Institut für Erd- und Umweltwissenschaften
Geophysik

Inversion of seismic source parameters for weak mining-induced and natural earthquakes

Kumulative Dissertation
zur Erlangung des akademischen Grades
”doctor rerum naturalium”
(Dr. rer. nat)
in der Wissenschaftsdisziplin ”Geophysik”

eingereicht an der
Mathematisch-Naturwissenschaftlichen Fakultät
der Universität Potsdam

von
Ali Tolga Şen

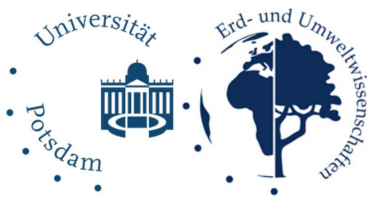

Potsdam im April 2014

Published online at the
Institutional Repository of the University of Potsdam:
URL http://opus.kobv.de/ubp/volltexte/2014/7191/
URN urn:nbn:de:kobv:517-opus-71914
http://nbn-resolving.de/urn:nbn:de:kobv:517-opus-71914

Abstract

The purpose of this thesis is to develop an automated inversion scheme to derive point and finite source parameters for weak earthquakes, here intended with the unusual meaning of earthquakes with magnitudes at the limit or below the bottom magnitude threshold of standard source inversion routines. The adopted inversion approaches entirely rely on existing inversion software, the methodological work mostly targeting the development and tuning of optimized inversion flows. The resulting inversion scheme is tested for very different datasets, and thus allows the discussion on the source inversion problem at different scales. In the first application, dealing with mining induced seismicity, the source parameters determination is addressed at a local scale, with source-sensor distance of less than 3 km. In this context, weak seismicity corresponds to event below magnitude M_W 2.0, which are rarely target of automated source inversion routines. The second application considers a regional dataset, namely the aftershock sequence of the 2010 Maule earthquake (Chile), using broadband stations at regional distances, below 300 km. In this case, the magnitude range of the target aftershocks range down to M_W 4.0. This dataset is here considered as a weak seismicity case, since the analysis of such moderate seismicity is generally investigated only by moment tensor inversion routines, with no attempt to resolve source duration or finite source parameters. In this work, automated multi-step inversion schemes are applied to both datasets with the aim of resolving point source parameters, both using double couple (DC) and full moment tensor (MT) models, source duration and finite source parameters. A major result of the analysis of weaker events is the increased size of resulting moment tensor catalogues, which interpretation may become not trivial. For this reason, a novel focal mechanism clustering approach is used to automatically classify focal mechanisms, allowing the investigation of the most relevant and repetitive rupture features. The inversion of the mining induced seismicity dataset reveals the repetitive occurrence of similar rupture processes, where the source geometry is controlled by the shape of the mined panel. Moreover,

moment tensor solutions indicate a significant contribution of tensile processes. Also the second application highlights some characteristic geometrical features of the fault planes, which show a general consistency with the orientation of the slab. The additional inversion for source duration allowed to verify the empirical correlation for moment normalized earthquakes in subduction zones among a decreasing rupture duration with increasing source depth, which was so far only observed for larger events.

Acknowledgements

It would not have been possible to write this doctoral thesis without the help and support of the kind people around me, to only some of whom it is possible to give particular mention here.

Above all, I would like to express my special appreciation, sincere gratitude and thanks to my principal supervisor Prof. Dr. Torsten Dahm and my advisor Dr. Simone Cesca, who have been tremendous mentors for me. I appreciate all their contributions of time, ideas, and funding to make my Ph.D. experience productive and stimulating.

During this long Ph.D study journey, I met with a lot of nice, polite, smart scientists and luckly with some of them we got good friends. I would like to thank my collegues Samira Magsoudi and Francesco Grigoli who had shared the same office with me for last 4 years. I would like to thank to Prof. Dr. Thomas Meier, Dr. Eleanora Rivalta, Dr. Dietrich Lange, Dr. Sebastian Wehling-Benatelli, Dr. Monika Bischoff, Dr. Lars Krieger, Dr. Sebastian Heimann, Lutz Ehlert, for their friendship and for their scientific supports.

Last, but by no means least, I would like to thank Serpil Şen and Aziz Şen who are not only my parents but also my best friends, my very good friends Dr. Francesco Maccaferri, Dr. Luigi Passarelli, Efi Psatha, Onur Ergin and especially to Gülce Koç who were always next to me in good and bad days.

Contents

List of Figures

Chapter 1

Introduction

1.1 Motivation

A major task in seismology is to analyze and understand the earthquake rupture processes. Important earthquake source parameters for any seismotectonic interpretation are the orientation of the rupture plane, the released seismic energy, the size of the rupture process or the presence of a preferential direction of the rupture. A second target of earthquake source studies is to determine whether the earthquake source is characterized by a shear failure along a surface (double-couple mechanism), or by other processes, for example, involving volumetric changes at the earthquake source. Among possible physical mechanisms differing from a shear fault representation, we have explosions, tensile cracks and collapse seismic sources. The study of non double couple components is relevant for certain natural events, such as those taking place in volcanic regions or in geothermal areas, as well as for induced or triggered earthquakes, which are stimulated by or consequence of human operations. Induced seismicity, in particular, is gaining a significant interest since different geomechanical operations, such as mining, waste water disposal, geo-resources exploitation and water reservoir impoundments have been shown to trigger or induced seismicity at a local scale [e.g. Cesca et al., 2013a], also affecting regions considered aseismic. Induced or human triggered earthquakes may affect the seismic hazard of a region. Source inversion studies for weak earthquakes are still challenging, but important towards a better understanding of involved rupture processes and towards the discrimination among natural and induced seismicity [Cesca et al., 2013b; Dahm et al., 2013]

Several seismological source inversion approaches have been proposed in the past to investigate the characteristics of the earthquake rupture process. They usually assume simplified earthquake source models, e.g. moment tensor point source models, which are selected to find an optimal fit between synthetic and observed ground motion seismograms. Moment tensor inversion techniques are nowadays routinely applied to large, tectonic earthquakes worldwide. Such applications, which are restricted to the frequency range between 0.01 Hz and 0.2 Hz, are reliable and stable, even for automated approaches. However, the moment tensor inversion of weak earthquakes has to be performed at higher frequencies and is more difficult and by far not standard. In this work, I adapted and tested an inversion scheme, which is established for the study of strong earthquakes at low frequencies, to weak and shallow earthquakes which generate sufficient signal noise ratio (SNR) only at high frequencies above 0.5 Hz. Some of the studied events have been induced by mining activities.

Through the implementation, adaptation, automation and application of this inversion algorithm, my final goal is to obtain source parameters for large dataset of weak mining induced and natural earthquakes.

1.2 Overview

One of the major research aspect of the seismology is try to understand the rupture process of the earthquake source. The simplest model to define the earthquake source, based on the point source approximation was already mentioned by Love [1927]. According to Aki & Richards [1980] an earthquake source can be considered as a point source, if both, the distance of the observer from the source and the wavelength, are much greater than the linear source dimension.

Most of the seismological source analyses are based on the assumption that the earthquake source mechanism describes a pure shear faulting process [Gilbert, 1884; Lawson & Reid, 1908; Reid, 1910]. This process can be described under a point source approximation using a double couple (DC) model. The adoption of this source model may pose a strong limitation towards the study of induced seismicity and certain types of natural events. In the last decades, a broad literature focused on the modeling of non-shear faulting earthquake mechanisms [e.g.

Feignier & Young, 1992; Hasegawa & Kanamori, 1987; Kanamori et al., 1993; McGarr, 1992a,b]. In this context, the point source double couple model has been often replaced by a more general moment tensor point source model, which was introduced by Gilbert [1971]. The moment tensor representation provides a more general model for the earthquake source, which can be used to describe both a pure shear fault, an isotropic source, a deformation source with no net volume change, or a combination of these cases under a point source assumption.

On the other hand, any point source model is deficient to describe the spatial and temporal properties of the seismic source, and is therefore unable to provide information on the small-scale details of the rupture process. For example, under a point source approximation, we can not explain changes in the apparent duration of the source process at different azimuths and stations, which is a common of observation of rupture directivity, indicating a preferential direction of the rupture process. To tackle these limitations, in the early 1960s, first (rectangular) finite source fault models were proposed by Ben-Menahem [1961, 1962] to describe the complex source mechanism problem in a more detailed way. Upon these early works, other finite source models have been proposed to describe the earthquake finite source. Among these, the most known and used are the uni-lateral and bi-lateral rectangular fault models by Haskell [1964] and the circular fault model by Brune [1970]. Several further earthquake source descriptions, such as slip map [Hartzell & Helmberger, 1982; Hartzell & Heaton, 1983; Olson & Apsel, 1982] approaches were more realistic, but often require a large number of source parameters. In these conditions, the source inversion problem, which is the process of estimating the earthquake source parameters based on the modeling and fit of observed ground motion seismograms, may have multiple solutions, all providing a similar fit to the data. The eikonal source model [Heimann, 2011] has been recently proposed as a compromise source model, which aimed to include some realistic source features with a reduced number of source parameters. The eikonal source model is described by only 13 parameters. The eikonal model is based on a variable rupture velocity based on a fixed scaling ratio with the variable shear wave velocity. The spatial extension and shape of the source model considers natural boundaries of a rupture plane, such as the free surface or brittle-ductile boundaries. For shallow earthquakes, for example, assuming the rupture plane is bounded within the crust, this eikonal model shape may vary among a circular fault, for small unbounded surfaces of small earthquakes, to quasi-rectangular faults, for large earthquakes with a rupture length much larger than the crustal thickness. The eikonal model can also consider rupture directivity, as the rupture

nucleation can be chosen at any location within the rupture area. The eikonal source can be described as the superposition of multiple point sources, homogeneously distributed along the rupture area and with the same rise time. The eikonal source model is shown in Figure 1.1.

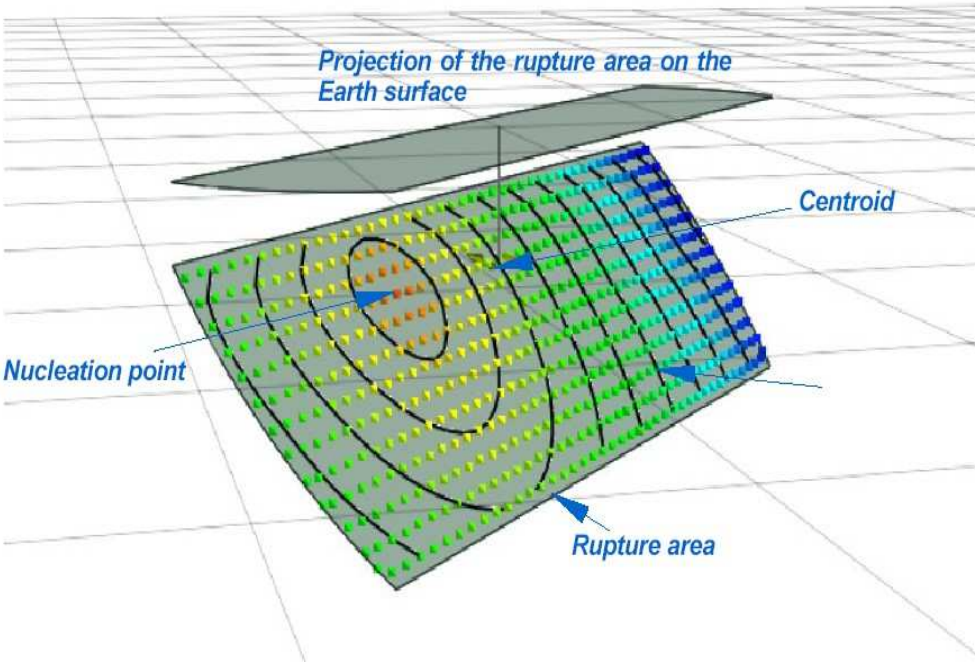

Figure 1.1: Graphical representation of the eikonal source model. The he superposition of multiple point sources which are homogeneously distributed along the rupture area [Heimann, 2011].

Since the focal region cannot be directly investigated, seismological approaches need to infer information on the rupture process from the surface expression of the earthquake occurrence. For weak or deep earthquake, which does not produce a significant surface deformation, seismograms recorded at the surface are the most important source of information. Recoded waveforms are affected both by the source processes and by the seismic wave propagation path from the earthquake source to the receiver, therefore they can be modeled only by accounting for both source and propagation path effects.Seismic source inversion can be described as the procedure of modeling of observed seismograms, in order to investigate the

source parameters and source mechanism of the earthquake. The typical source inversion approach relies on an available velocity model, which allows to model the wave propagation between source and receiver. It is then possible to compute synthetic seismograms for different source models. By comparing synthetic and observed seismograms, we can infer which is the most likely source model.

Nowadays, several national and international services (USGS NEIC, Global CMT, ERI, INGV, ETH, or NOA, among others) provide focal moment tensors for moderate and large earthquakes in quasi real time [e.g. Bernardi et al., 2004; Dreger, 2003; Melis & Konstantinou, 2006; Pondrelli et al., 2002; Rueda & Mezcua, 2005; Stich et al., 2003]. However, robust, fast and automated point source inversion techniques are limited to moderate and large earthquakes, at regional and teleseismic distances. Local moment tensor inversion applications to small magnitude events and microseismicity are still demanding. On the other hand, standard automated point source inversion routines relies on double couple or deviatoric moment tensors and have a limited potential towards the assessment of induced earthquakes sources. Inversion procedures assuming a full moment tensor source representation [Cesca et al., 2013b; Šílenỳ & Milev, 2008], able to reproduce a broad range of physical processes at the earthquake sources, are rarely implemented. Automated inversion approach for finite source models [Cesca et al., 2010; Heimann, 2011; Vallée & Bouchon, 2004], which is the determination of important source parameters such as the size of the rupture area or the main direction of the rupture propagation, are also not common, and semi-automated finite source inversions are typically discussed only for single large earthquakes or for small datasets.

Source mechanism determination is an extremely important task for induced seismicity studies in mining areas. Different studies specifically investigated source inversion in mining environments in the past [e.g. Feignier & Young, 1992; Julià et al., 2009; McGarr, 1992a,b; Šílenỳ & Milev, 2006; Trifu et al., 2000], including coal, copper, zinc and gold mines. The seismic source information can be used for defining rupture process in mining area and improve the hazard assessments. Following Hasegawa et al. [1989], mining induced events can follow in six basic mechanisms (figure 1.2): cavity collapse, pillar burst, tensional fault, and three types of fault slip.

The analysis of the focal mechanisms is important to evaluate the fault geometry and local stresses. Automated moment tensor inversion scheme may process large

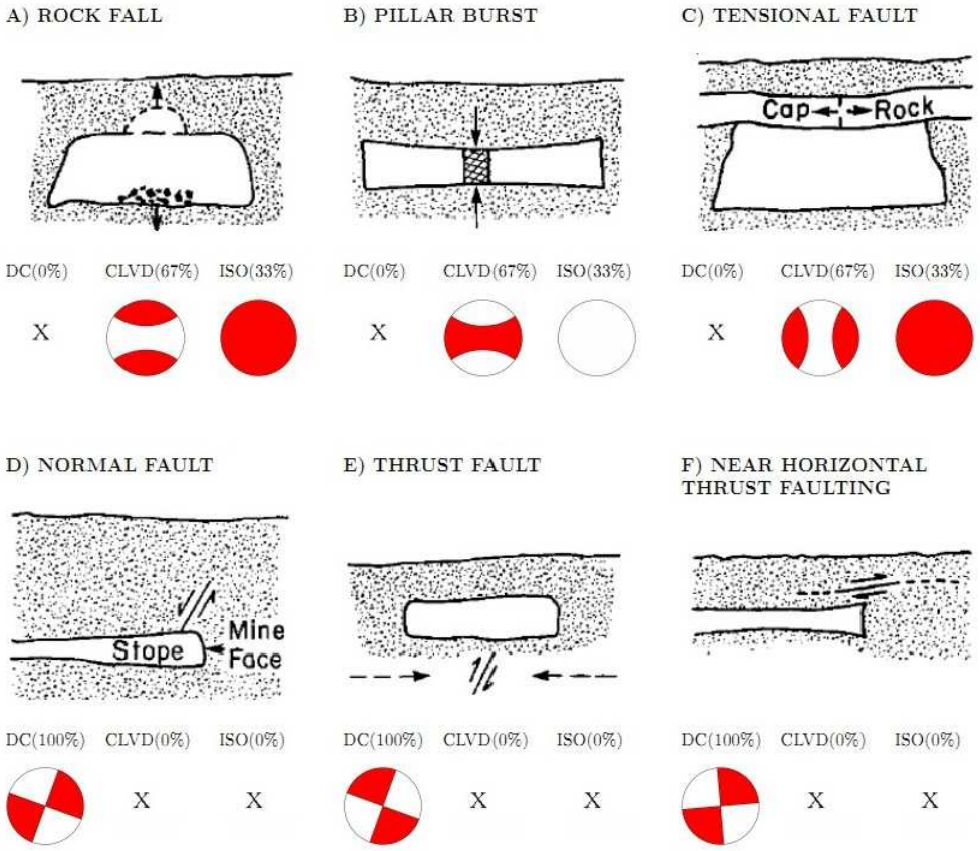

Figure 1.2: Schematic diagram of six possible ways in which mine-induced tremors can occur (A-F, upper row) and their focal mechanism representations (A-F, lower row).

earthquake datasets and provide catalogues including different source parameters. In this case, the analysis and interpretation of large moment tensor catalogues may become challenging, and it is difficult to extract the most important information, e.g. the most common type of focal mechanisms, from the catalogue. Therefore, specific methods should be developed to automatically recognize the most dominant source characteristics of the target seismicity and to identify families of events with similar mechanisms. For the purpose of focal mechanism classification, clustering methods can be applied. Clustering techniques have been used so far in seismology to recognize events patterns and to identify foreshocks and aftershocks based on their spatial location [Konstantaras et al., 2012; Lippiello et al., 2012; Ouillon & Sornette, 2011], to assess temporal evolution of the

seismic sources [Hainzl et al., 2000; Kagan & Knopoff, 1976; Kagan & Jackson, 1991] or to analyse the spatiotemporal distribution of seismicity [Hainzl et al., 2000; Sornette & Werner, 2005]. Finally, waveform similarity has also been used for clustering approaches [Cattaneo et al., 1999; Maurer & Deichmann, 1995; Wehling-Benatelli et al., 2013], in order to identify earthquakes producing similar seismic signals. In this study, we extend the focal mechanism clustering method, which was first proposed by Willemann [1993] through the adoption of a density based clustering algoritm (DBSCAN). The resulting clustering approach is very flexible, and it can be used for comparison of different seismic source representations, using different metrics.

In this work I discuss the adoption of a multistep inversion approach to derive point and finite source model parameters. This approach considers the problem of non double couple sources, and provide a multiple point source inversion result, either considering a pure DC source model and a full moment tensor representation. The inversion approach used in this work combines the fit of amplitude spectra and displacement waveforms. This approach helps to reduce the effects due to the misalignment of observed and synthetic waveforms and to the simplification of the adopted seismic velocity model. The inversion framework is based upon the Kiwi tools software [Cesca et al., 2010; Heimann, 2011]. The original multi-step inversion approach by Cesca et al. [2010] has been modified to perform source inversion with different source models: pure double couple (DC) point source, full moment tensor (MT) point source, point source with variable time duration and a finite source model. As finite source model, the eikonal model [Heimann, 2011] was chosen. The Kiwi tools were previously successfully used for source inversion of moderate and large magnitude events [e.g. Buforn et al., 2011; Cesca et al., 2010, 2011, 2013b; Custodio et al., 2012; Domingues et al., 2013; Heimann, 2011], but have never been applied to small magnitude tectonic and induced earthquakes below M 3.5 before this work. Similarly, they have been applied to a broad range of earthquakes at regional and teleseismic distances, but never at local distances, e.g. with stations at less than 10 km. In this work, the inversion algorithm is also used to infer kinematic source parameters, for example to understand rupture process and rupture directivity. Kinematic inversion with the Kiwi tools have been so far performed down to magnitude M_W 5 [e.g. Cesca et al., 2010, 2011; Custodio et al., 2012; Domingues et al., 2013; Heimann, 2011]. Here, they are tested for much smaller events, below M_W 2.0. A second, simplified, inversion scheme, only extends the first point source model by the inference of the rupture duration, a parameter which is important to investigate the scaling

law of rupture processes, for example to judge scaling relations between rupture duration, moment release and depth in certain tectonic environments.

This study focuses on two different datasets. The first one is composed by mining induced events, taking place during the mining of a panel close to Hamm, Ruhr region, Germany. Moment tensor inversion of low magnitude events, with M_W magnitudes in the range between 0 and 2, is carried out by the modeling of full waveform at local distances, below 3 km from the epicenters. Since more than 1000 earthquakes are investigated, this part of the work also deals with the problem of automation of the source inversion procedure. In this case, also the interpretation of a large moment tensor catalogue results demanding. To better analyse such large dataset, a new moment tensor clustering approach is here proposed: this method allows to automatically classify DC focal mechanisms and full moment tensors into earthquake clusters with similar source models. The second dataset includes, instead, tectonic earthquakes from Chile. The dataset is composed by a subset of the aftershock sequence of the 2010 M_W 8.8, Maule earthquake, Chile. Data were recollected by a dense network installed in the framework of an international experiment, following the occurrence of the Maule earthquake. In this case, the source inversion algorithm is used to investigate point source models, rupture duration and their correlation to the source depth and slab geometry.

This thesis has the following structure. A first theoretical chapter (Chapter 2) is devoted to introduce the reader to basic seismological concept, including moment tensors and finite models of the earthquake source, earthquake source parameters and the source inverse problem. This chapter includes a first general description of the inversion technique adopted in this thesis. Chapter 3 discusses the implementation of an automated full moment tensor and finite source inversion procedure and its application to a large dataset of coal mining induced earthquakes, occurring at the Ruhr region, Germany. Chapter 4 describes a new methodology for earthquake source clustering. Its application to the moment tensor results from the Ruhr mine dataset illustrates its potential applications towards automated source classification and mining monitoring. Chapter 5 demonstrates the application of previous techniques to the case of tectonic earthquakes. The application focuses to the aftershocks of the 2010 M_W 8.8 Maule earthquake, Chile. The analysis includes point source inversion, rupture duration estimation, and the investigation of scaling relation, e.g. rupture duration in function of source depth, for moderate seismicity. Finally, overall concluding remarks of this thesis are given in Chapter 6. This is a cumulative thesis. The results of the PhD work substantially

contributed to the preparation of three research papers, which are recollected in Chapter 3, 4 and 5. Two articles are currently published on Geophysical Journal International, while the third one is in review at Journal of Seismology. The papers discussed in Chapter 3 and 5 are entirely result of the PhD work, whereas the contribution to the clustering approach discussed in Chapter 4 is limited to the analysis of the Ruhr dataset with that technique.

Chapter 2

Inversion of Source Parameters for Induced and Natural Earthquake

2.1 Introduction

Earthquakes are associated to the release of seismic energy within the earth. Most earthquakes are consequence of tectonic stresses, where the stress release is typically accommodated by a shear failure along a fault, which produces a slip between the foot and hanging wall at the earthquake focal region. However, earthquake source process does not always take place as a pure shear faulting. For example, earthquakes occurring in volcanic, mining and geothermal areas may be consequence of other rupture processes, including collapses, rock-bursts, tensile cracks, explosions and deformation sources. The modeling and investigation of source parameters is an important tool to characterize and discriminate these rupture processes.

The sudden energy release at the earthquake source causes radiation of seismic waves. The observation of these waves at the earth surface (seismograms) is an important source of information, which can be used to understand the earthquake source process and to infer earthquake source parameters, like the earthquake source location, the released energy, the possible orientation of the fault plane, or the rupture duration. However, seismograms as recording seismic wave amplitude as a function of time at a given location do not only contain information about the source processes, but also depend on the seismic wave propagation between the seismic source and the receiver. A seismogram can be expressed as the convo-

lution of source, path and instrument response terms (Figure 2.1). If we remove the instrument effect from the observed seismogram, we obtain a description of the ground motion at the receiver location, which only depends on the earthquake source process and the wave propagation along the source-receiver path. If we can further model the wave propagation term, e.g. by estimating source propagation effects within a simplified earth structure model, we can obtain information on the earthquake source and focal mechanism. The last step of this process is known as source inversion process in seismology.

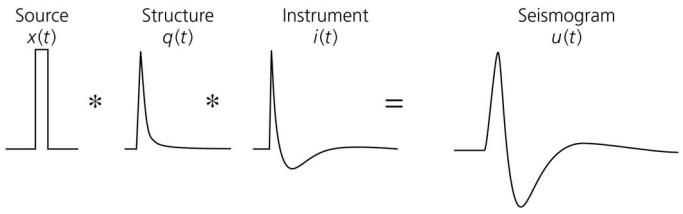

Figure 2.1: A seismogram can be expressed as convolution of source, structure and the instrument effect [after Stein & Wysession, 2009].

This chapter discusses the most common source models, and then introduces the models adopted in this thesis. Then, it considers the problem of modeling seismic wave propagations to construct synthetic seismograms for different source models, and briefly mentions how this step is performed in the present work. Finally, it discusses the inversion problem of retrieving earthquake source parameters by comparing synthetic and observed seismograms.

2.2 Earthquake Source Models

Several earthquake source models have been proposed in the past. The simplest approach to describe the earthquake source is to assume a spatial point source and a focal mechanisms corresponding to a pure shear fault. This model is not sufficient to describe certain source processes, such as an explosion source, nor to describe the spatial extension of the earthquake source and the temporal evolution of the rupture process. A moment tensor representation is more general and can

be used to describe different processes, still under a point source approximation. On the other hand, several finite source models have been proposed to describe the spatial and temporal evolution of the rupture.

2.2.1 Point Source Models

The theory of point source plays a fundamental role in earthquake seismology and even the most simple double couple representation is still widely used nowadays to describe the source processes of many earthquakes [Jost & Herrmann, 1989]. In early 1950's, first earthquake source models were described by single couple forces. It was soon recognized that such a source model was failing to explain S wave radiation [Honda, 1962]. The Double Couple (DC) point source model was developed in the early 1960's [Burridge & Knopoff, 1964; Maruyama, 1963]. The energy radiation pattern at the earthquake source was modeled as a DC, assuming a slip with a single direction of motion along a single fault plane. According to this geometric description, this earthquake source model is defined by three angles (strike, dip, rake), which are needed to provide the plane orientation and the slip direction, and a scalar (scalar moment), which indicates the energy released. A sketch of this model is given in Figure 2.2.

The strike angle ϕ defines the azimuth (with respect to North) of the trace of the fault on a horizontal plane, such as the Earth's surface. The dip angle δ characterizes the steepness of the fault. The rake or slip angle λ is used to describe the direction of the motion within the fault plane. An illustrative graphical representation of the focal mechanisms is by means of the focal sphere (Figure 2.3). The fault and auxiliary planes intersect the focal sphere and divide it in four quadrants. Colored quadrants correspond to compressional P waves and include the tension axis (T), which reflects the minimum compressive stress direction, whereas white quadrants correspond to tensional P waves and contain the pressure axis (P), which reflects the maximum compressive stress direction.

The seismic waves radiated from an earthquake can be used to estimate both the magnitude and the orientation of the focal mechanism. However, the elastic seismic wave radiation from a DC source is symmetric. Given this radiation pattern,

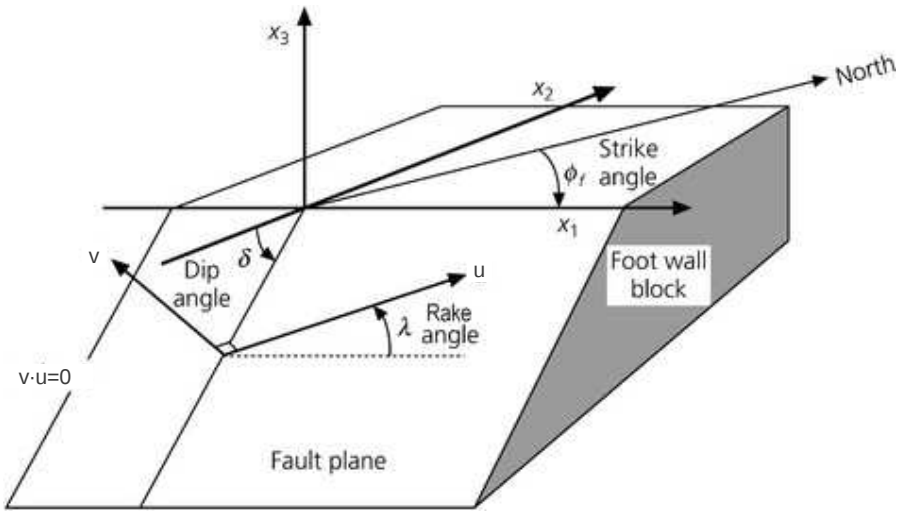

Figure 2.2: A sketch of the fault geometry and source parameters. u and v represent the slip vector and the fault normal, respectively, whereas ϕ, δ and λ represent the strike, dip and rake angles, respectively [after Stein & Wysession, 2009].

it is not possible to identify the fault plane among the two nodal planes, if a point source model is used.

A more general representation of the earthquake point source is using a moment tensor [Gilbert, 1971]. This representation describes the earthquake source by means of equivalent forces and moments applied at the source (Figure 2.4), and is mathematically described by a second order matrix. We define the moment tensor M as:

$$M = \begin{bmatrix} M_{xx} & M_{xy} & M_{xz} \\ M_{yx} & M_{yy} & M_{yz} \\ M_{zx} & M_{zy} & M_{zz} \end{bmatrix} \tag{2.1}$$

$\mathbf{M_{kj}}$ represents a pair of opposing forces pointing in the k direction, separated in the j direction. For angular momentum conservation, the condition $\mathbf{M_{kj}}$ = $\mathbf{M_{jk}}$ should be satisfied, so that the moment tensor is symmetric and have only six independent elements. Using the notation of Figure 2.4, double couple displacement fields are represented by the sum of two couples with same absolute strength, such as M_{xy}+M_{yx}, M_{xx}-M_{yy}, M_{yy}-M_{zz}, M_{yz}+M_{zy}, etc. [Bock,

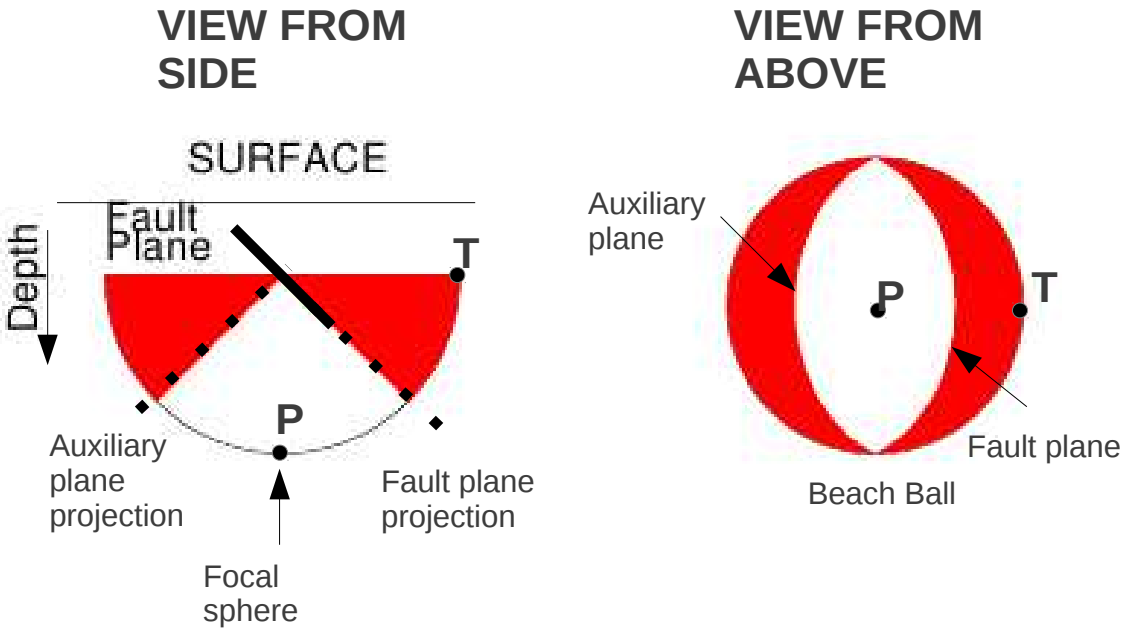

Figure 2.3: The focal sphere, or beach-ball, representation is the projection of the lower half of an imaginary, spherical shell (focal sphere) surrounding the earthquake source along an horizontal plane.

2012]. An explosion source can be modeled by the sum of three vector dipoles $tr(M) = M_{xx}+M_{yy}+M_{zz}$ with same strength. A compensated linear vector dipole (CLVD), which is representing a deformation at the source with no net volume change, is represented by a vector dipole of strength 2 and two vector dipoles of unit strength but opposite sign in the two orthogonal directions.

The DC model is a special case of moment tensor. The moment tensor components in an isotropic medium for a double couple of equivalent forces are given by:

$$M_{kj} = M_0(u_k v_j + u_j v_k) \tag{2.2}$$

where $\mathbf{u}$ is the slip unit vector along the fault surface and $\mathbf{v}$ is the unit vector normal to the fault plane [Aki & Richards, 1980]. The term $\mathbf{u_k v_j + u_j v_k}$ in equation (2.2) forms a tensor, describing a double couple.

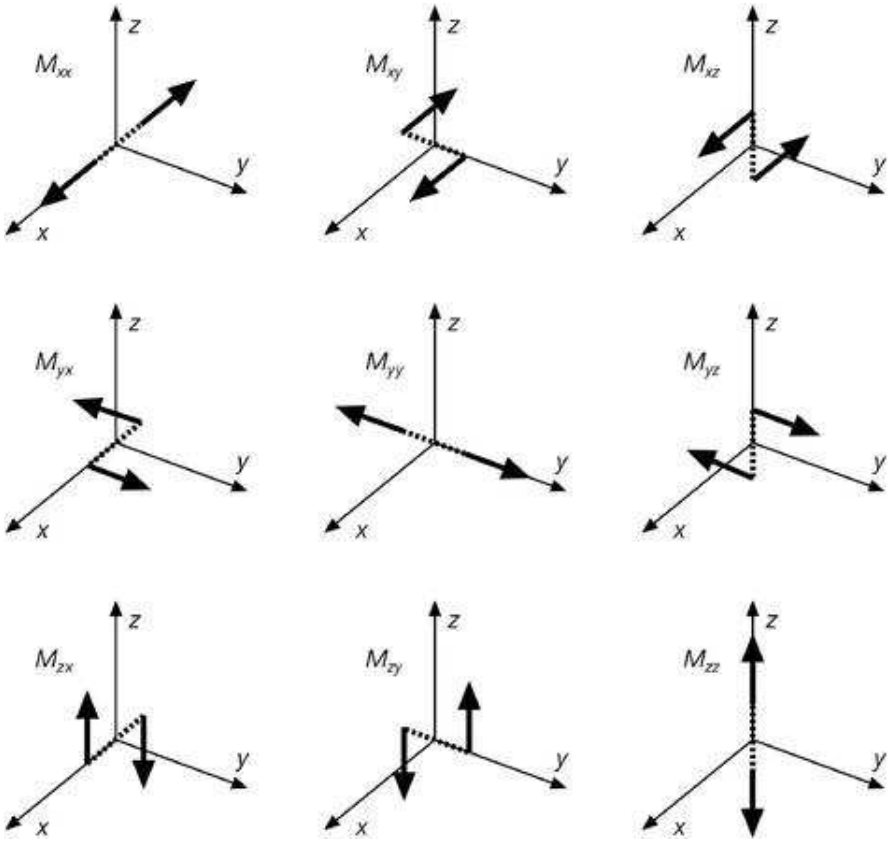

Figure 2.4: The 9 force couples representing the moment tensor. For example M_{xy} is a force couple in the xy-plane acting in the x-axis direction, [after Aki & Richards, 1980].

The characteristic properties of a moment tensor representing a double couple are that: (1) one eigenvalue of the moment tensor vanishes, and (2) the sum of the eigenvalues vanishes. Physically, this is a representation of a shear dislocation source with no volume change.

The scalar seismic moment can be defined on the base of the rigidity μ, the area of the fault plane A and the average slip $\bar{u}$ as:

$$M_0 = \mu A \bar{u} \tag{2.3}$$

Now, following Jost & Herrmann [1989], we can obtain the Cartesian components of symmetric moment tensor (Figure 2.4), in terms of strike, dip and slip angles:

$$\begin{aligned}
M_{xx} &= -M_0(\sin\delta\cos\lambda\sin 2\phi + \sin 2\delta\sin\lambda\sin^2\phi) \\
M_{yy} &= M_0(\sin\delta\cos\lambda\sin 2\phi - \sin 2\delta\sin\lambda\cos^2\phi) \\
M_{zz} &= M_0(\sin 2\delta\sin\lambda) \\
M_{xy} &= M_0(\sin\delta\cos\lambda\cos 2\phi + \frac{1}{2}(\sin 2\delta\sin\lambda\sin 2\phi)) \\
M_{xz} &= -M_0(\cos\delta\cos\lambda\cos\phi + \cos 2\delta\sin\lambda\sin\phi) \\
M_{yz} &= -M_0(\cos\delta\cos\lambda\sin\phi - \cos 2\delta\sin\lambda\sin\phi)
\end{aligned} \tag{2.4}$$

2.2.2 Moment Tensor Decomposition

Until now we introduce the DC source, and then generalized to a full moment tensor source. We can now consider a moment tensor configuration and then try to describe it through its decomposition into different terms, using a generalized moment tensor decomposition method.

$\mathbf{M}$, the principle axis tensor can be decomposed into two terms, $\mathbf{M^{ISO}}$ and $\mathbf{M^{DEV}}$ (Figure 2.5), in the following way:

$$\mathbf{M} = \mathbf{M^{ISO}} + \mathbf{M^{DEV}} \tag{2.5}$$

$$\mathbf{M} = \frac{\mathbf{1}}{\mathbf{3}}\begin{bmatrix} tr(M) & 0 & 0 \\ 0 & tr(M) & 0 \\ 0 & 0 & tr(M) \end{bmatrix} + \begin{bmatrix} m_1 & 0 & 0 \\ 0 & m_2 & 0 \\ 0 & 0 & m_3 \end{bmatrix} \tag{2.6}$$

It is important to point out that while the decomposition of $\mathbf{M}$ into $\mathbf{M^{ISO}}$ and $\mathbf{M^{DEV}}$ is unique, the further decomposition of $\mathbf{M^{DEV}}$ is not. $\mathbf{M^{ISO}}$ describes the

volumetric changes at the source. $\mathbf{M^{DEV}}$ can be decomposed in different ways [for an overwiew, see: Jost & Herrmann, 1989]. The most common decomposition (Figure 2.5), which is also used in this study, is into a pure double couple (DC) and a CLVD (compensated linear vector dipole). $\mathbf{M^{CLVD}}$ represents the deformation at the source with no net volume change.

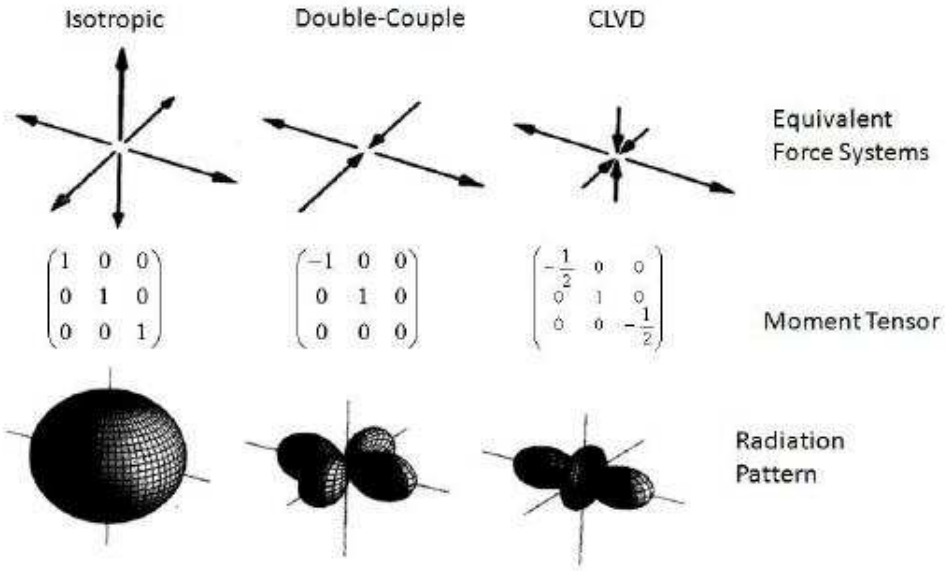

Figure 2.5: Force couples, moment tensors (in principal coordinate system), and radiation patterns for the three source types used in moment tensor decomposition [after Julian et al., 1998].

If the absolute values of eigenvalues are sorted so that $m_3 \geq m_2 \geq m_1$, the crack factor ϵ can be used to judge the deviation from a pure shear crack model. This is defined as:

$$\epsilon = \frac{m_1}{m_3} \tag{2.7}$$

where m_1 and m_3 are the smallest and the largest eigenvalues of the deviatoric part $\mathbf{M^{DEV}}$, respectively. ϵ varies between -0.5 and 0.5. For a pure DC source, ϵ=0, because m_1=0. For a pure CLVD, ϵ=$\pm$0.5. The parameter is positive for tensile sources and negative for compressive sources. The DC percentage can be

expressed as:

$$DC\% = (1 - 2\epsilon)100 \tag{2.8}$$

We can now write the deviatoric part of $\mathbf{M}$ as:

$$M^{DEV} = m_3(1 - 2\epsilon)(v_3 - v_2) + m_3\epsilon(v_3 - v_2 - v_1) \tag{2.9}$$

where the left side of the summation is representing the pure shear crack (DC) part of the moment tensor and the right side its deformation action (CLVD).

Full moment tensor solutions, especially for seismicity in mining areas, can be used to discuss the non-DC components of the earthquake source, e.g. to evaluate the presence of tensile or isotropic components. This is specially important for mining induced applications, where the finding of relevant non-DC components can be used to detect collapse, rockburst or explosive processes. Hudson et al. [1989] proposed a diagram for a discriminative representation of the source mechanisms in terms of isotropic, DC and CLVD components, which is independent from the type of DC mechanism. In the source type diagram, the moment tensor decomposition is represented by two parameters, $\mathbf{T}$ and $\mathbf{k}$, which are displayed along the horizontal axis and vertical axis respectively. The T parameter reflects the ratio between the CLVD and DC components within the deviatoric moment tensor. The $\mathbf{k}$ parameter reflects the ratio between isotropic and deviatoric term [Hudson et al., 1989]. This type of plot (Figure 2.6) is often referred as source-type diagram: in this diagram DC mechanisms map to the center, purely explosive and implosive events are at the top and at bottom of the diagram, and finally, pure CLVD are at the edges of the horizontal axis.

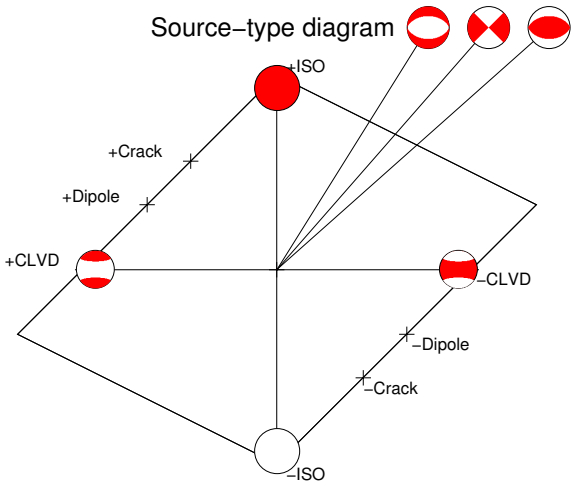

Figure 2.6: Equal-area source type plot, showing source types in terms of T, constant volume (shear) component in the source (horizontal), and k, proportion of the volume change (vertical).

2.2.3 Source Time Function

The Source time function (STF) is defined as the time history of the seismic moment release from the earthquake source. The analysis of the STF can provide several information about the rupture process of the earthquake. For example, it has been often used to identify multiple events, occurring within short time [e.g. Chung & Kanamori, 1976].

The components of the moment tensor are time dependent. To simplify, the source rupture history can be assumed as homogeneous, so that each moment tensor component has the same time history. In this case, the time history s(t) can be factorized and separated from the moment tensor components:

$$M_{kj}(t) = s(t)\hat{M}_{kj} \tag{2.10}$$

It is common to assume s(t) as a ramp function of duration $\mathbf{d}$ [Dahm & Krueger, 2014], and it has been showing that $\mathbf{d}$ is typically correlated with the earthquake size and magnitude [Tanioka & Ruff, 1997].

2.2.4 Finite Source Models

We saw that a first limitation of a point source representation is that there is an intrinsic ambiguity between fault and auxiliary plane. In order to identify the fault plane, additional information about the seismic source is needed. There are different ways to assess the fault plane orientation. One possibility is to infer it on the base of the spatial distribution of the earthquake aftershocks [e.g. Jones, 1988], which should align along one of the nodal planes. A second possibility is to determine a rupture directivity effect [Cesca et al., 2011; Warren & Shearer, 2006], which indicates a preferential direction of the rupture and can be used to discriminate between fault and auxiliary plane. Finite source inversion provides a third method to identify the true rupture plane [Heimann, 2011]. Other methods have been proposed to assess the rupture plane orientation, including hypocenter-centroid relative location [Zahradnik et al., 2008], or using Empirical Green Functions [e.g. Mori & Hartzell, 1990].

Finite source models represent the slip history on the fault. In last decades, especially for large earthquakes, different finite source model have been proposed. Ben-Menahem [1961, 1962] described extended sources in terms of distributions of single and double couples. The rupture front propagates with a certain velocity over a rectangular surface. Haskell [1964] proposed rectangular dislocation models, both including unilateral and bilateral ruptures, and Savage [1966] proposed an elliptical fault model. Brune [1970] proposed a circular fault model where shear stresses suddenly applied [Udias, 1999].

This study adopts the eikonal finite source model, proposed by Heimann [2011]. The eikonal source model can be described as the superposition of multiple point sources, homogeneously distributed along the rupture area and with the same rise time. The earthquake source is defined by 13 parameters: 8 of them describes the model under a point source approximation (origin time, latitude, longitude, depth, scalar moment, strike, dip and rake), while the remaining 5 (radius, nucleation point coordinates(x,y), rupture velocity and rise time) are related to the finite rupture.

The temporal evolution of the rupture process, using the eikonal source model can be described as follows. The finite source is discretized into a number of point sources, each one emitting energy during a limited time, here referred as rise time. Each point source is only activated, when the rupture front reaches

it. The velocity of the rupture front is controlled by the relative rupture velocity parameter and by the depth-dependent shear wave velocity profile. The entire duration of the rupture process $\mathbf{d}$, equivalent to the duration of the source time function for a point source, will be given by:

$$\mathbf{d} = \mathbf{t_R} + \mathbf{t_r} \tag{2.11}$$

where t_R is the rupture time, here defined as the time required for the rupture front to propagate along the whole rupture area and t_r is the rise time, here defined as the duration of the energy emission of each point source.

The directivity effect can be described as the effect of the earthquake source on the amplitude, frequency and duration of the seismic waves propagating in different directions. The duration of the recorded signals will be different in each station due to rupture direction and station position. For example, an unilateral rupture along a horizontal linear source will produce theoretical P wave pulses of shorter duration for stations located towards the rupture propagation, and larger duration for stations in the opposite direction to the rupture (figure 2.7). The apparent source duration is the estimate of the source time function assuming a point source representation on the base of the observation at a single station. It can be estimated, for example, as the duration of the recorded P-wave pulse at that receiver. The analysis of apparent source time durations at different stations can be used to assess the rupture directivity [Cesca et al., 2011].

2.3 Synthetic Seismograms

It was shown that observed seismograms can be viewed as the convolution of source, path and instrument response. After removing the instrument effect from the observed seismogram, the true displacement trace d at a location x and time t can be expressed as [Aki & Richards, 1980]:

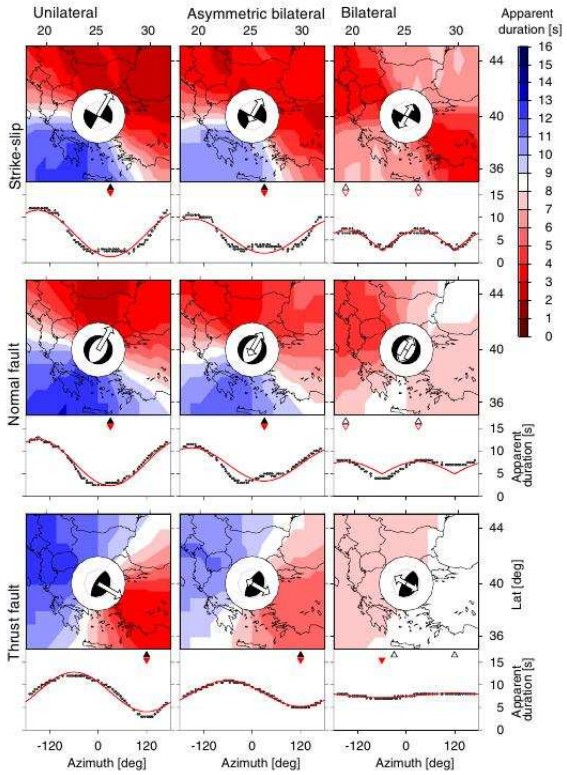

Figure 2.7: Synthetic inversion results for 9 different source mechanisms, considering a circular eikonal source model. Color scale represent increasing apparent duration from red to blue around source respect to rupture model and rupture direction [after Cesca et al., 2011].

$$d_n(x,t) = M_{kj} * G_{nk,j} = \hat{M}_{kj}[s(t) * G_{nk,j}] \tag{2.12}$$

where d_n are observed seismograms for the n component, M_{kj} are constants representing the components of the second order seismic moment tensor M, s(t) is the source time function (e.g. a Heavyside function describing an instantaneous slip), $G_{nk,j}$ are the spatial derivative of Green's functions (GFs) and * denotes convolution. GFs are functions of source and receiver locations, describing the response at the receiver location in consequence of the application of simple excitations at the seismic source location, and take into account wave propagation effects.

The three components of the displacement can be represented on the base of 27 independent functions, the spatial derivatives of the Green's tensor (3^{rd} order tensor). These can be expressed as:

$$\frac{\partial}{\partial \xi_j} G_{nk}(x,t') = \frac{\partial G_{nk}}{\partial x_i}\frac{\partial x_i}{\partial \xi_j} + \frac{\partial G_{nk}}{\partial t}\frac{\partial t'}{\partial \xi_j} = G^{(n)}_{nkj} + \dot{G}^{(f)}_{nkj} \tag{2.13}$$

where the first and second terms correspond to near and far field and are denoted by (n) and (f) superscripts. The displacement equations for the near and far field are:

$$u^{(n)}_n(x,t) \approx \hat{M}_{kj} s(t) * G^{(n)}_{nkj}(x,t) \tag{2.14}$$

$$u^{(f)}_n(x,t) \approx \hat{M}_{kj} s(t) * \dot{G}^{(f)}_{nkj}(x,t) = \hat{M}_{kj} \dot{s}(t) * G^{(f)}_{nkj}(x,t) \tag{2.15}$$

If a layered 1D earth model is assumed, as it will be in all applications discussed in this thesis, the number of elementary seismograms will reduce to 10 from 27 where 8 of them are representing the far field terms and 2 of them are representing the near field terms. Even if there is no well defined distance for classification for near field and far field distances, the most useful criteria to define the near field zone is by comparison of the source dimension with the source to site distance. Seismograms in the near field are characterized by the fling step effect which is the effect of the source function in the near field distances [Somerville et al., 1997]. When the source time function is an impulse, the far field P and S waveforms are impulsive but the near-field waveform is a ramp starting at the P arrival time and ending at the S arrival time [Archuleta & Hartzell, 1981]. An example is given in figure 2.8.

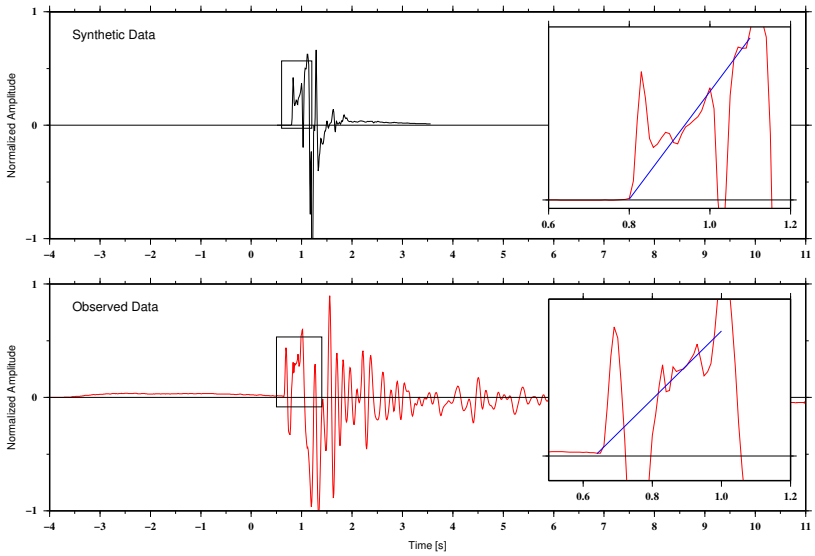

Figure 2.8: Near field affect on synthetic (above) and observed (below) ground displacement seismograms.

Assuming a flat layered earth model, the radial (u_r), transversal (u_t) and vertical (u_z) displacements at a station at a given location and depth can be expressed as linear combination of only 10 functions (g, typically also referred as Green's functions or elementary seismograms). Their contributions is weighted using coefficients, which depend on the source geometry (in terms of moment tensor components) and station azimuth (ϕ). Details on the definition of the elementary seismograms, as implemented within the Kiwi tools, can be found in Heimann [2011].

In a flat layered media, with P wave, S wave, density and attenuation properties only varying as a function of depth, the elementary seismograms are only dependent on the source depth and the epicentral distance to the considered receiver. To speed up the computation of synthetic seismograms for different focal mechanism and source-station geometry, a concept of GF database can be introduced. According to the target seismicity, elementary seismograms can be computed for a range of source depth and epicenter-receiver distances, choosing a proper velocity model and seismogram sampling. These are stored in a fast-access Green's function database, which will allow the fast computation of synthetic seismograms at the time of the inversion [Heimann, 2011]. Several methods and algorithms may be implemented to compute elementary seismograms. In this study, they have

been computed using the QSEIS software [Wang, 1999], which is based on the reflectivity method. Synthetic seismograms generation was here discussed only for point source models. Modeling the synthetic seismograms for a finite source can be achieved by discretizing the finite source into a number of point sources, and then superposing the delayed contributions (synthetic seismograms) of these point sources.

2.4 Source Inversion

In the past, many different source inversion approaches were proposed. They model the earthquake source mechanism process by comparing synthetic and observed seismograms or spectra. The comparison may be performed either in terms of first motion polarities [e.g. Reasenberg & Oppenheimer, 1985], P and S wave amplitudes [e.g. Nakamura, 2002] , spectral amplitude combined with P wave polarities [e.g. Lund & Bodjvarsson, 2002], S/P-wave amplitude ratios [e.g. Hardebeck & Shearer, 2003; Julian & Foulger, 1996; Kisslinger, 1980], full waveforms in the time domain [Dreger & Helmberger, 1993; Kanamori, 1972; Kikuchi & Kanamori, 1982; Langston, 1976; Madariaga & Papadimitriou, 1985] and amplitude spectra in the frequency domain [Brune, 1970; Cesca et al., 2006; Cotton & Campillo, 1995; Dahm & Krüger, 1999]. The waveform inversion approach, either in the time or in the frequency domain, is assumed to be more robust, and can be used to infer full moment tensor source models, whereas polarity approach are typically limited to DC source models.

There are several software packages which can handle the source inversion problem, such as ISOLA [Sokos & Zahradnik, 2008], Time-domain MT inversion code (TDMT-INVC) [Dreger, 2003], and Rapidinv [Cesca et al., 2010], which is based on the Kiwi tools [Heimann, 2011]. The Kiwi tools are an open source software package which allows fast calculation of synthetic seismograms for extended earthquake sources and can be used as a framework for point source moment tensor inversion and finite source inversion procedures [Cesca et al., 2010; Heimann, 2011].

Previously, the Kiwi tools were adopted for a broad range of source inversion studies [e.g. Cesca et al., 2010, 2011; Custodio et al., 2012; Domingues et al.,

2013; Heimann, 2011], dealing with DC point source, full moment tensor and finite source inversion with different datasets. However, they were never tested before for the analysis of mining induced seismicity. Point source inversion with the Kiwi tools was never performed before below magnitude M_W 3.5, nor finite source below magnitude M_W 4.4. One aim of this study is to test and extend their application to weaker events.

2.4.1 Source Inversion in Time and Frequency Domain

The moment tensor inversion can be performed on the base of equations (2.12), which can be expressed in the form of a linear system:

$$\mathbf{d} = \mathbf{G}\mathbf{m} \tag{2.16}$$

where $\mathbf{d}$ is the recorded data (displacements), $\mathbf{m}$ is the model vector (6 moment tensor components) and $\mathbf{G}$ are the Green's functions. This system of equations can be solved by the least squares (LS) technique, either in time or in the frequency domain. However, in the frequency domain, equation (2.16) can be written as:

$$d(\omega) = G_{nk}(\omega)m_k(\omega) = [\Re G_{nk} + \Im G_{nk}]m_k \tag{2.17}$$

where $\Re$ and $\Im$ denote the real and imaginary parts of the spectrum. The absolute value of the spectral seismogram amplitudes are then:

$$|d(t)| = \sqrt{([\Re G_{nk}(\omega)m_k(\omega)]^2 + [\Im G_{nk}(\omega)m_k(\omega)]^2} = f(G, m) \tag{2.18}$$

The amplitude spectrum is then a non linear function f (amplitudes of basic seismic dipole sources or couples) of the moment tensor components. The resulting

amplitude spectra inversion problem is non linear. The inversion can be linearized and iteratively solved, e.g. by a gradient method using a number of starting models.

An alternative method to solve the proposed inversion problems is by grid search in a multi dimensional model space. The approach can be used to test a number of source model and evaluate the discrepancy between predicted synthetics and observations. The model which best fit the observation can be considered as the preferred one.

2.4.2 Inversion Procedure

The inversion scheme used in this work is based on the adoption of two reference source models: a full moment tensor point source model and the eikonal finite source model [Heimann, 2011]. The DC point source model can be described by any of these models: it can be considered as a special case of MT source, with no isotropic non CLVD terms, as well as a particular eikonal source, with a point source size.

This work follows a multi step inversion approach (Figure 2.9), as earlier proposed by Cesca et al. [2010]. The basic idea is to perform the inversion in different steps, so that only certain source parameters are inverted at a time. This approach avoids the simultaneous inversion of many parameters, which could result non robust and time consuming. Typically, it first focuses on the source parameters describing the simplest DC point source model (strike, dip, rake, scalar moment), investigates then the full MT source model, in some cases considers the temporal evolution of a point source model (centroid location), and finally investigates the additional parameters of the finite eikonal source model.

The method combines the fit of amplitude spectra and displacement traces in order to derive all desired source parameters in the most stable way. The adoption of a mixed scheme, where the inversion is both performed in the time and in the frequency domain is justified by the known advantages and limitations of these two approaches (figure 2.9). The amplitude spectra inversion method is less sensitive to a precise trace alignment and to phase shifting owing to mismodeling of the crustal structure, allowing more stable solutions also at slightly higher frequen-

cies. However, the focal mechanism polarity cannot be resolved by the amplitude spectra inversion. For this reason, we apply a two step point source inversion process, combining the potential of both approaches.

The quality of derived source models is judged on the base of the fit among observed seismograms or amplitude spectra and synthetic ones. As misfit definition, both L^1-norm or L^2-norms can be used.

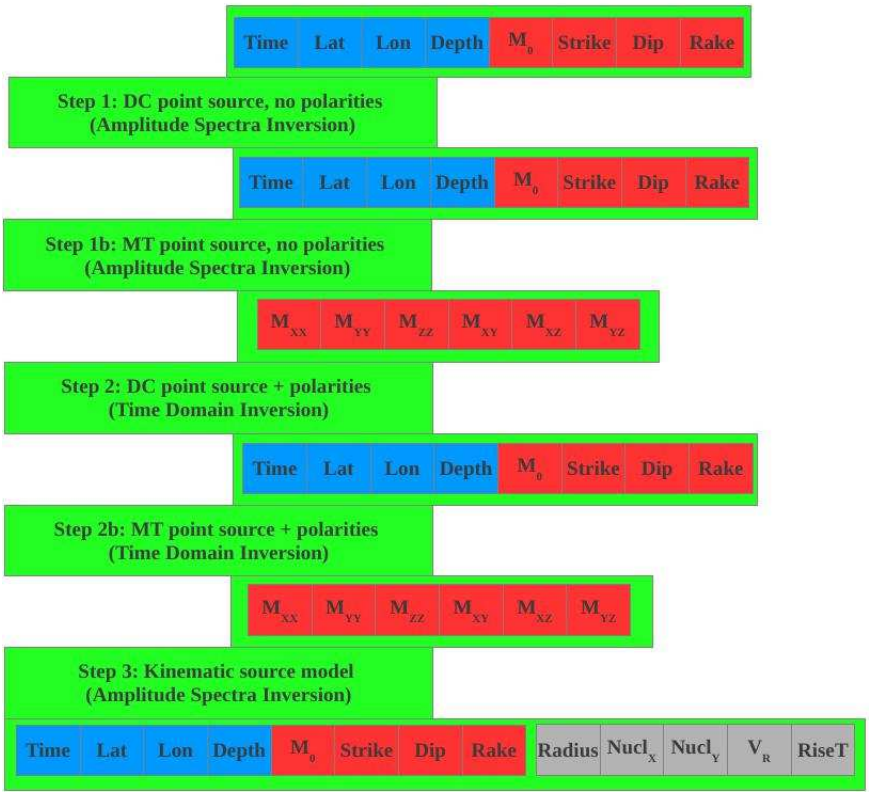

Figure 2.9: Inversion flow scheme. Blue colored boxes represent the parameters which are known at the specific inversion steps and red colored boxes represent the parameters which are going to be inverted only for point source model assumption. Grey colored boxes represent the parameters which are going to be inverted for finite source models.

The general inversion flow is here described in its main steps. Before starting

the inversion, some information on the target earthquake is assumed to be known, including origin time, epicentral location and rough depth and magnitude estimations.

In the first inversion step, different starting point DC source models are considered. They vary in focal mechanism and depth, but rely on the original location coordinates. Waveforms can be filtered and tapered, depending on the target seismicity (e.g. either bodywaves or full waveform can be modeled, and the frequency range can be optimally selected upon the frequency content of the target earthquakes). The inversion is performed comparing amplitude spectra; as discussed, this approach is preferred to time domain inversion, because it is less sensitive to a precise trace alignment or to phase shifting owing to simplified structural modeling [Cesca et al., 2006; Dahm et al., 1999; Romanowicz, 1982]. The modeling of non-rotated displacement traces (North, East, vertical components) allow to keep spare horizontal traces, whenever single traces are noisy or unavailable [Cesca et al., 2010].

Once a best DC source model is found, the space of full MT solutions is investigated. As starting configurations, both the best DC model and a range of non-DC models of equivalent scalar moment are considered. The best retrieved full MT is then decomposed into DC, CLVD and ISO components. This procedure relies on the MoPaD tool [Krieger & Heimann, 2012].

Since the polarity of the focal mechanism has been resolved by the amplitude spectra inversion, a comparison in the time domain is performed in the second step. Both the DC and full MT model solutions are considered. Once the polarity ambiguity is solved, perturbed centroid locations and times are investigated. For each of the tested location and time, unshifted displacement waveforms are compared, and the best location and time are found. At the end of this stage, all point source parameters are derived.

After obtaining point source parameters, the rise time can be inverted using a point source approximation, in order to obtain an estimate of the source duration. In this work, the rise time is iteratively inverted for each station separately, providing different estimates of the apparent duration, as seen at each station. This information could be used to infer rupture directivity effects, as proposed by Cesca et al. [2011]. Here, it is mostly used [Şen et al., 2014] to evaluate the average duration (see the applications in chapter 5).

The last inversion step aims to provide finite source parameters, such as fault plane orientation, radius, nucleation point coordinates, rise time and rupture velocity. The analysis relies on the best DC point source model, as the geometry of the two tested fault planes is constrained upon that focal mechanism. Application to synthetics and to real cases from previous studies have shown that this inversion step is mostly sensitive to the duration of the rupture. This introduces a trade-off between rise time and rupture time, within two extreme cases [Cesca et al., 2010; Heimann, 2011]: if the rise time is chosen long (in the range of point source duration), the rupture time will be extremely small, and vice versa. This also affects the size estimation, which scales with the rupture time. In this study, a fixed ratio of 1/3 between rise time and rupture time is chosen (Cesca et al. 2010), which is consistent with scaling relations of earthquake rupture dynamic [e.g. Stein & Wysession, 2009]. To reduce the number of free parameters the rupture velocity is often constrained, to be slower than the shear wave velocity (Valle and Bouchon, 2004). The last inversion step is typically performed by fitting amplitude spectra, now including higher frequencies, above the earthquake corner frequency; the L^1- norm have been here often preferred, because less sensitive to outliers [Cesca et al., 2010; Heimann, 2011]. To avoid excessive computation, the inversion is performed by a grid walk over a limited number of source models.

Chapter 3

Automated Full Moment Tensor Inversion of Coal Mining-induced Seismicity

Authors:
Ali Tolga Sen[1], Simone Cesca[1,2], Monika Bischoff[3], Thomas Meier[4], Torsten Dahm[1,2]
Journal:
Geophysical Journal International
Status: Published
doi: 10.1093/gji/ggt300

Authors affiliation:
1) Institute of Earth and Environmental Sciences,
University of Potsdam, Potsdam, Germany
2) GFZ (German Research Centre for Geosciences) Potsdam,
Section 2.1, Physics of earthquakes and volcanoes,
Potsdam, Germany
3) BGR, LBEG/NED,
Hannover, Germany
4) Institute of Geosciences, Christian-Albert-University,
Kiel, Germany

3.1 Summary

Seismicity induced by coal mining in the Ruhr region, Germany, has been monitored continuously over the last 25 yr. In 2006, a dense temporary network (HAMNET) was deployed to locally monitor seismicity induced by longwall mining close to the town of Hamm. Between 2006 July and 2007 July, more than 7000 events with magnitudes M_L from -1.7 to 2.0 were detected. The spatiotemporal distribution of seismicity shows high correlation with the mining activity. In order to monitor rupture processes, we set up an automated source inversion routine and successfully perform double couple and full moment tensor (MT) inversions for more than 1000 events with magnitudes above M_L -0.5. The source inversion is based on a full waveform approach, both in the frequency and in the time domain, providing information about the centroid location, focal mechanism, scalar moment and full MT. Inversion results indicate a strong dominance of normal faulting focal mechanisms, with a steeper plane and a subhorizontal one. Fault planes are oriented parallel to the mining stopes. We classify the focal mechanisms based on their orientation and observe different frequency-magnitude distributions for families of events with different focal mechanisms; the overall frequency-magnitude distribution is not fitting the GutenbergRichter relation. Full MTs indicate that non-negligible opening tensile components accompanied normal faulting source mechanisms. Finally, extended source models are investigated for largest events. Results suggest that the rupture processes mostly occurred along the subvertical planes.

3.2 Introduction

In mining environment, it is extremely important to monitor the spatial and temporal evolution of rupture processes. The determination of focal mechanisms, scalar moment, centroid location and extended source parameters can provide valuable information to detect weakened regions and evaluate risks of further dangerous ruptures or changes in structural properties, such as hydraulic permeability. With respect to tectonic earthquakes, which are typically well described by shear failures, mining-induced events can show different kind of rupturing types. Hasegawa et al. [1989] proposed different possible failure types for mining-induced seismicity, including normal and thrust faulting, pillar burst, roof collapses and outburst.

Mining blasts can also be performed during the mine exploitation. A moment tensor (MT) representation offers a general model to describe a point seismic source and can be used to model all mentioned rupture processes within such approximation. While seismic sources of natural seismicity are often modelled by means of constrained MT, forcing the isotropic [ISO; and in some cases the compensated linear vector dipole (CLVD)] term to be null, seismic sources in mining environments should be modelled by a full MT. Most of the discussed processes, in fact, present significant, or even dominant, non-double couple (DC) components, including ISO components. Several MT inversion approaches have been developed in the last decades and successfully applied to a variety of seismic sources and spatial scales. Different studies specifically investigated source inversion in mining environments in the past [e.g. Feignier & Young, 1992; Fletcher & McGarr, 2005; Julià et al., 2009; Lizurek & Wiejacz, 2011; McGarr, 1992a,b; Šílenỳ & Milev, 2006; Trifu et al., 2000; Vavryčuk, 2001; Vavryčuk & Kühn, 2012], including coal, copper, zinc and gold mines as well as underground laboratories. Full MT source inversions were either performed modelling first onset polarities, combining polarities, amplitudes and spectra of different body waves [Feignier & Young, 1992; Lizurek & Wiejacz, 2011; Trifu et al., 2000; Vavryčuk, 2001] and fitting body waves or full waveforms in the time domain [Fletcher & McGarr, 2005; McGarr, 1992a,b; Šílenỳ & Milev, 2006; Trifu et al., 2010; Vavryčuk & Kühn, 2012]. Data were either provided by surface, borehole and in-mine sensors, including accelerometers, geophones and broadband seismometers.

MT applications have been typically applied to learn about sources in order to reduced number of events in the mining environment. McGarr (1992a) studied seismic tremors in a South African gold mine and inverted ground motion data of 10 events ($1.9 \leq M \leq 3.3$) to investigate MT components and source characteristics of these events. Most events showed significant implosive components and normal shearing. Feignier & Young [1992] used accelerometer data to determine the focal mechanisms of 33 seismic events down to moment magnitude -3.2, 12 events showed tensile cracks, 6 mostly implosive sources and the remaining 15 events showed mainly shear components. Dahm [2001]; Dahm et al. [1999]; Manthei et al. [2001] studied MT and rupture of acoustic emissions in salt mines at about 15 kHz, and found predominant DC mechanisms and rupture lengths of about 20 mm. Šílenỳ & Milev [2008] inverted amplitudes of body waves for five events (M_W 2.5-2.7) in a gold mine; resulting focal mechanisms showed significant non-DC components, and in most cases this non-DC component values are related with pressure of single couple, which fit with the physical model of pillar

bursts. Julià et al. [2009] studied 76 earthquakes (M_W range 0.5-2.6) and inverted P, SV and SH spectral amplitudes to obtain MT components; their results showed that principal stresses were generally negative, a result attributed to gravitational effects on mined-out areas. Limitation to more extensive applications were due to the quality of the data and signal-to-noise ratio, which reduce the inversion performance for small events, as well as because of the wave propagation modelling in strongly heterogeneous mining environments. These difficulties also limited the performance of automated MT inversion routines; attempts for automated source inversion have been discussed for synthetic data in Trifu et al. [2000], and further tested on a salt mine data set [Trifu et al., 2010].

Different features, which are characteristic of mining environments, may pose a strong limitation to any seismological approach to model and invert seismic waveforms. First of all, given the presence of strong heterogeneities (voids, galleries, and different mineralogical bodies), observed high-frequency waveforms may only be reproduced by accounting for wave propagation in 3-D (when not 4-D, given the time evolution of the environment) velocity models. [Vavryčuk & Kühn, 2012] performed a MT inversion adopting a 3-D velocity model and discussed the limitation of simplified models in reproducing first onset polarities, amplitudes and waveforms. Simplified (e.g. homogeneous or 1-D) velocity models can be adopted when fitting lowpass filtered seismograms, removing the higher frequencies which are affected by small-scale heterogeneities; this approach may be limited to larger events, because of poor signal-to-noise ratios at low frequencies. A second problem, is that mining regions are typically (seismically) noisy environments, and recordings may show a poor signal-to-noise ratio, especially for weaker events. Seismic noise often presents a significant temporal variation as a consequence of mining activities, which can affect the inversion performance. Rydelek & Sacks [1989] showed that the number of events detected is larger during day time, because of mining activities, but the number of detected small events is higher during night time, because of the absence of cultural noise and better performance of the inversion approach. Finally, because of the large number of induced events in mining environments, manual processing is not viable to evaluate the rupture processes of detected seismicity, and automated inversion procedures must be set up. We choose here to perform the source inversion in the frequency domain, fitting full waveform amplitude spectra, instead of the more standard time domain inversion approach. Such approach proved to be more robust in presence of model simplification or structural mismodelling [Cesca et al., 2006; Dahm et al., 2000; Šílenỳ & Milev, 2008] and allows the use of slightly

higher frequencies with respect to the time domain approach. The algorithms we use have been developed based on the Kiwi tools [Heimann, 2011], and follow an inversion scheme similar to those successfully adopted by Cesca et al. [2010, 2011] for the analysis of seismic sources at regional distances. In our approach, both the DC, full MT and kinematic source parameters can be retrieved.

The aim of this paper is to implement a robust automated source inversion algorithms and investigate earthquake rupture processes following coal mining, both by determining DC and full MT point source models. Since most earthquakes are caused by shear faulting, DC source models can be first discussed. However, since induced mine tremors can include tensile and ISO components, a full MT inversion is also performed. Finite source inversion is more challenging because of the very small magnitudes (down to M -0.5) and the requirement to fit high-frequency radiation with a simplified velocity model. Because of this reason, we limit the application of extended source inversion to about 130 biggest events. Finite source inversion can provide information on the rupture plane and other extended source parameters, such as the size of the rupture. Since different inversion steps may be affected by inaccurate modelling of waveform propagation, we test the inversion using different velocity models and stations configurations, and perform the inversion at different frequency ranges. We finally propose an automated inversion scheme, and successfully apply it to more than 1000 events.

3.3 Mining Activity and Seismic Data

Coal mining in the Ruhr region, North Rhine-Westphalia, Germany, has been performed for centuries since early 13th century. The coal deposit spreads between the Lippe and Ruhr river. Geologically, the region is characterized by the presence of different coal-bearing layers from the Upper Carboniferous period. The Carboniferous strata comprise sandstone and claystone layers with distributed coal seams. This structure has an overall thickness of approximately 6000 m. The coal seams reach the surface in a strip along the Ruhr river and dip downward from the river to the North. The thickness of the coal layers ranges up to few meters. It is thinner for deeper layers, it increases up to 3-4% workable seam between the Witten and Bochum strata (approximately between 2000 and 4000 m depth) and then drop again in the younger, upper stratas of the Upper Carboniferious [Cold-

ewey & Semrau, 1994; Drozdzewski, 1993] According to Coldewey & Semrau [1994], the total thickness of the carbon layers is approximately 70 m. However, the authors only considered the first 3000 m depth structure.

Induced seismicity in the Ruhr region has been monitored by the Ruhr University Bochum since 1983 [Bischoff et al., 2010a]. In this paper, we focus on the investigation of induced seismicity following longwall coal mining in the Hamm Heringen region, which is located at the eastern edge of the Ruhr region (Figure. 3.1). The process of longwall consists in the repeated mining and removal of single slice of ore. The mining activity processed at depths between 700 and 1500 m below the free surface. The size of the slices removed by the longwall mining had dimensions up to 300 m in height and 1000 m in length. The thickness of the coal seams was about 2 m [Bischoff et al., 2010b]. The stope advanced with an average velocity of about 100 m $month^{-1}$. The mining region is considered tectonically inactive and all seismicity is induced or triggered by mining operations. The region close to the town of Hamm was continuously monitored by the HAMNET network, a local network running from 2006 June to 2007 July. Along the time of the network deployment, longwall mining was mostly performed between 2006 August and 2007 April. The network consists of 15 surface sensors: nine short-period (Mark L- 4C-3D, 1 Hz) and six broadband stations (five Güralp CMG, 60 s; one Trillium 40, 40s). The network covers a region of about 2 km x 3.5 km (Figure. 3.1). Thanks to this local network, 7651 events could be detected and located during the monitoring interval (Bischoff et al. 2010a). However, about 5 per cent of these events have been related to mining activities at the neighboring longwall in Bergkamen, and are therefore not discussed here. The remaining data set includes 7337 local events at the mining area (51.64-51.67 Lat N, 7.72-7.76 Lon E) in Hamm Heringen [Bischoff et al., 2010a]. Epicentres are spread across a surface of 4 by 3 km, and about 90$\%$ are located close to the longwall area. Hypocentral estimations (manual picking, based on P arrival time inversion) indicate source depths between 500 and 1500 m. The average source depth is at about 1000 m, which is approximately 100 m above the average mining level. Earthquake magnitudes range between M_L -1.7 and 2.0. The large number of events and the good quality of seismic waveforms provide an optimal data set to test the potential of automated MT and kinematic inversion routines for weak shallow induced events at a very local scale (below 2 km).

In this work, we initially consider all (more than 3000) events with magnitudes

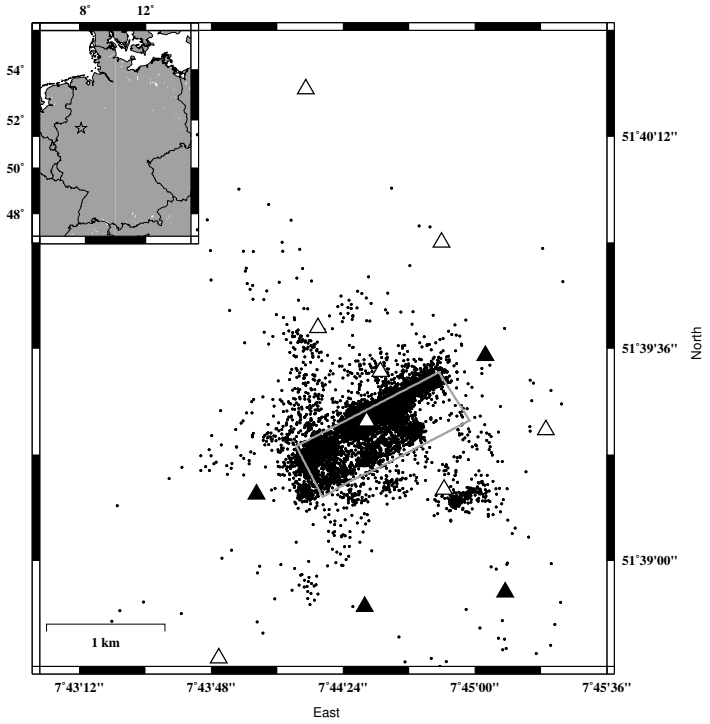

Figure 3.1: Geographical insight (left) and study region (right). White triangles denote short period stations and black triangles broadband stations. A gray rectangle indicates the geometry of the mined panel.

above or equal M_L -0.5. However, results will only be discussed for a subset of 1169 events, for which we obtain the most robust results (Figure 3.2). The selection of best results has been based on a minimum number of observations and on the displacement spectra and time history misfits. The epicentral and depth distribution of the events used in this paper is shown in figure 3.2(a), where colour circles denote the spatiotemporal evolution of the seismicity: This shows a clear relation with the mining process, which proceeded from WSW toward ENE. The number of events increased during the mining activity and reduced again after the mining stopped. The frequency-magnitude distribution (FMD, Fig. 3.2b) does not follow the expected linear relation. Bimodal distributions have been often observed in mining environments [Holub, 1999; Kijko et al., 1988]. Possible explanations from the deviation to the Gutenberg-Richter relation might be a change in the sensitivity of the monitoring network or the superposition of separated processes with different size distributions (Mendecki 2012). According to Gibowicz

et al. [1994]; Kijko et al. [1988]; Mendecki [2012], two different hypothesis have been proposed to explain these separated processes: events can be classified in groups of different origin, either because of their occurrence in different structural bodies, or because of their relation with mining-induced or residual tectonic stresses. Both the rock heterogeneity and the stress distribution can affect the distribution and size of events, which is controlled by the size and distance between brittle or stressed patches, where sources can nucleate and stop. The superposition of different groups of events, each of them with a different magnitude-frequency distributions, leads to the observed bimodal distribution. In particular, it has been suggested that a concavity of the distribution, as observed for our data set, could be generated by high activity of low magnitude events induced by mining excavation, and larger events caused by failure along pre-existing geological faults [Mendecki, 2012].

3.4 Methodology

For the implementation of an automated source inversion algorithm for the mining environment we adopt the Kiwi tools (Heimann 2011). This software has been successfully applied to study seismic sources of moderate and large earthquakes at local and regional distances [Buforn et al., 2011; Cesca et al., 2010, 2013b; Custodio et al., 2012], and tested for automated routines [Domingues et al., 2013]. However, they have never been routinely applied so far to small events in near-field distances with magnitude below Mw 3.5. The Kiwi tools allow synthetic seismograms generation and source inversions, both for DC, full MT and different kinematic models, and require pre-calculated Greens functions (GFs), which are stored in structured databases. We test here two possible velocity models: a homogeneous model (V_p=3.880 km/s and V_s= 2.042 km/s) and a layered one. This last model (figure 3.2) was defined according to Pelzing [1978], and is based on sonic logs from five boreholes, seismic reflection and geological profiles from the region. GFs have been generated using a reflectivity method [QSEIS code Wang, 1999].

The inversion is performed at different steps, which are illustrated in figure 3.4 for

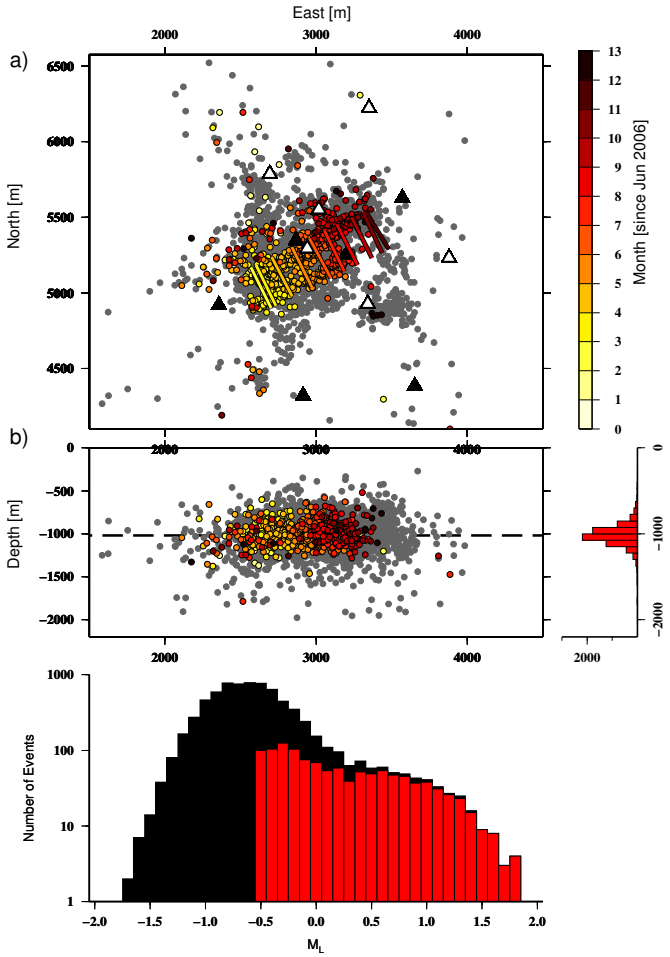

Figure 3.2: a) Spatial distribution of all located events (grey circles), spatiotemporal distribution of events studied in this work ($M_L \geq$ -0.5, colour from yellow to red according to the timescale) and temporal shift of the longwall mining stope (coloured bars). (b) The non-cumulative FMD (bottom) is plotted for all recorded events (black histograms); red histograms indicate events successfully inverted in this work.

a synthetic data set. In this example, data were generated with the layered model, while the inversion was performed assuming the homogeneous model. Note that, although 45 spectra and traces from 15 stations are fitted, only a small selection is shown for simplicity. The first point source inversion relies on the information available through the seismic catalogue compiled by the Ruhr University Bochum, which provide the hypocentral location and a first magnitude estimation. This information is used to set up a set of more than 10 000 starting configurations of the

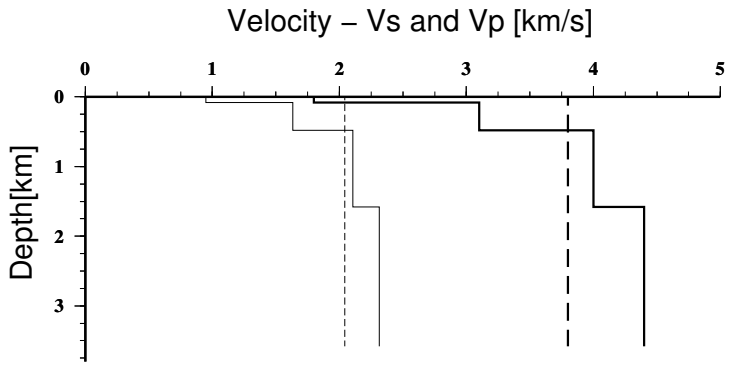

Figure 3.3: Layered (continuous lines) and homogeneous (dashed lines) velocity model used for the generation of Greens function (thick lines indicate vertical profiles for Vs and Vp , respectively).

point source parameters (strike, dip, rake, moment and depth; e.g. we assumed 15 possible starting depths, in the range 200 m with respect to the hypocentre location). In the first inversion step, we assume a DC point source model and perform the inversion in the frequency domain by fitting amplitude spectra of the whole trace. Since the inversion is non linear, we repeat the inversion iteratively for all considered starting configurations. A Levenberg-Marquardt approach is used to minimize the L^2 norm misfit from each starting source model. As a result of this first inversion step, the fault plane angles (strike, dip, rake; four configurations due to intrinsic fault-auxiliary plane and focal mechanism polarity ambiguities), the centroid depth, the scalar moment and thus the magnitude. The fit of amplitude spectra is here preferred for the inversion, because it does not require a precise alignment of observed and synthetic waveforms, and because it is less dependent on the chosen velocity model. We use non-rotated displacement traces (North, East, vertical components), in order to keep spare horizontal traces, whenever a single trace is damaged or unavailable. Data and synthetics are tapered in the time domain (we use 8 s long time windows and apply a taper which smooths 1 s at both window sides) and a bandpass filter is applied in the frequency domain. After testing different frequency ranges (see discussion in the following text), three preferred bandpasses were chosen: 0.5-2, 1-3 and 1-4 Hz. Inversions were repeated for all these three bandpasses. Results of the amplitude spectra inversions are ambiguous, because compression and dilatation quadrants cannot be distinguished. The best DC model, as well as other possible non-DC models (e.g. a pure ISO source as well as dipole and tensile cracks with different orientations), are chosen as starting models for the following amplitude spectra inversion step,

where a full MT point source model is assumed. Tapering, bandpass filtering and inversion approaches remain unchanged, so that the new misfit estimation can be directly compared with those of the DC model. The retrieved full MT is decomposed into DC, CLVD and ISO components using the MoPaD tool (Krieger and Heimann 2012). In the next inversion step, we determine the focal mechanism polarity, by computing synthetic displacement traces for both polarities with the observed waveforms. A grid search for possible centroid locations and centroid times, around the starting values (epicentre) is also performed. At the end of this stage, all point source parameters are derived (strike, dip, rake - two possible configurations, depth, moment and centroid coordinates). As a last step, a kinematic source inversion may be carried out. We generally adopt a circular source model; the performance of alternative line source models is mentioned in the discussion section. Other, more complex fault model have been proposed for mines [Mendecki & Lötter, 2011]. We choose here to use simplified finite source models, which are described by fewer parameters, to avoid any over parametrization of the inversion problem. For the finite source inversion we adopt the centroid location, focal mechanism and scalar moment according to the point source inversion results, and test a range of possible extended source models: two possible fault plane orientations are defined according to the best DC point source, eight rupture sizes range between 10 m (here equivalent to a point source, given the spatial sampling of the Greens function database) and 350 m radius, and five possible rupture propagations (outward, and four unilateral ruptures in different directions). The inversion is performed again by fitting amplitude spectra (here the L^1 norm is chosen) and repeated for two frequency ranges (1-10 and 1-20 Hz).

3.5 Methodology Evaluation Tests

This section is devoted to the description and discussion of a set of tests, both with synthetic and real data, with the purpose of evaluating the reliability and stability of the inversion results. A first set of synthetic tests aimed to evaluate to what extent the adoption of simplified and/or improper velocity models could affect the inversion results.

Synthetic data were generated using realistic source parameters, wave propaga-

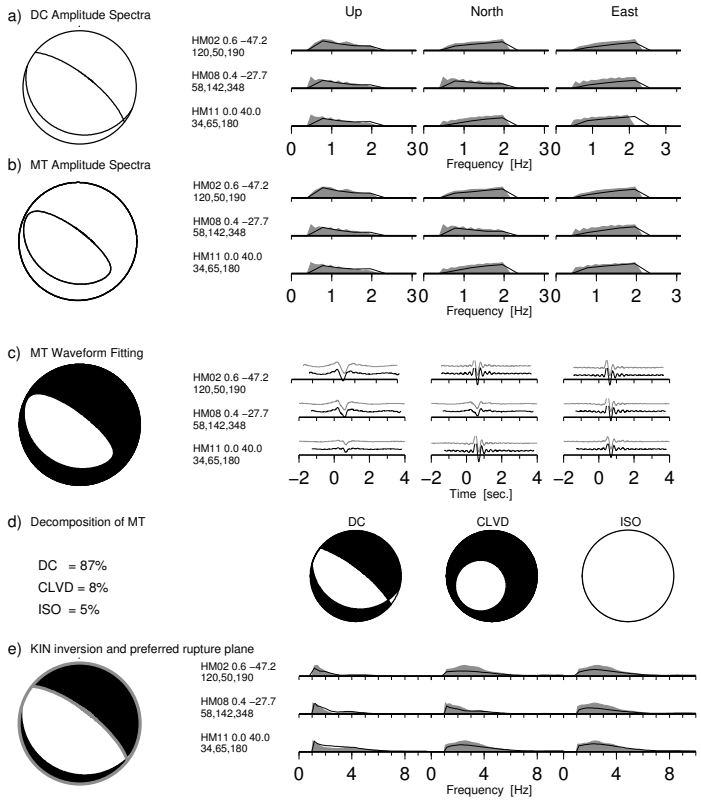

Figure 3.4: Example of the output of inversion process (synthetic event with M_W 1.1). (a) DC focal mechanism and fit of amplitude spectra (gray observed spectra, black synthetic spectra; selected stations only) after inversion step 1a. (b) Full MT focal mechanism and fit of amplitude spectra (grey observed spectra, black synthetic spectra) after inversion step 1b. (c) Full MT focal mechanism and fit of displacement waveforms (grey observed waveforms, black synthetic waveforms). (d) Percentage and focal sphere for the DC, CLVD and ISO components of the decomposed full MT. (e) DC focal mechanism and orientation of the preferred rupture plane (thick black line) and fit of amplitude spectra (grey observed spectra, black synthetic spectra) after inversion step 3 (kinematic inversion). All shown displacement traces and amplitude spectra are normalized.

tion and source-receiver geometry. Synthetic seismograms have been computed for a source located at 51.65266° Lon E and 7.74858° Lat N with depth 1.0 km, approximately at the centre of the observed-induced seismicity. We consider nine source mechanisms: three pure DC point source focal mechanisms (striking with 70°, 160°, 310°, dip 70°, rake 90°), three full MT point source mechanisms (including 50% positive ISO component; DC components are the same as for the

three pure DC synthetic events) and three extended source mechanisms (again same pure DC focal mechanisms, circular, subvertical rupture areas, with radius 50 m, rise time 0.05 s and rupture propagating unilaterally upward with a velocity of 1.4 km/s , corresponding to 70% of Vs at the source depth). The orientation of focal mechanisms is consistent with the normal faulting derived by analysis of first motion polarities for selected events [Bischoff et al., 2010b] and with the results of our inversion, which will be discussed in the following section. All events have a magnitude M_W 1.6 (note that here the magnitude has no significant importance, and only affects waveforms amplitudes). Synthetic displacements are then computed with a sampling of 0.01 s at all HAMNET stations locations, both using the homogeneous and the layered velocity model. No noise has been originally included, since our aim here is to discuss the effects of waveform propagation mismodelling. The inversion is then performed for DC, full MT and kinematic models for all 18 data sets (nine source models and two velocity models), assuming both possible velocity models. Finally, we can discuss 36 inversion results, which are summarized in figure 3.5 (where DC, MT and kinematic inversion labels denote pure DC, full MT and finite source models used to generate the data).

All inversion results point out the reliability of the derived focal mechanism solutions: strike, dip and rake are well-retrieved even when non-DC components are present, when the source ruptured a finite region, and when a wrong velocity model is used to reproduce the data. The adoption of a wrong model only affects the misfit values, but not the determination of the correct point source model. Similar results are found for the inversion performed with full MT data: with all models we can correctly retrieve non-DC components. The adoption of a full MT source does not lead to the retrieval of anomalous finite source parameter: all kinematic inversion performed with DC and MT source model indicate the smallest tested rupture radius (10 m), consistent with the point source models used to generate synthetic waveforms. Finally, inversions with data generated assuming finite source model indicated that: (a) DC source models are always well derived, even when using a wrong velocity model, (b) spurious non-DC components may be retrieved during point source inversion, up to 5% CLVD, 14% ISO and 17% non-DC when using the correct velocity model, and up to 9% CLVD, 24% ISO and 27% non-DC when using a wrong velocity model. The expected dominant DC components are always correctly derived. Rupture plane orientations, size and directivity are correctly retrieved when assuming the proper model, but can fail with a wrong one. Unilateral ruptures in other directions can be erroneously

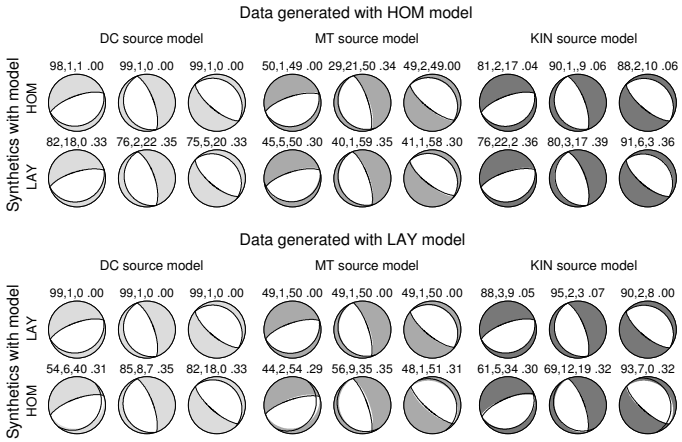

Figure 3.5: Synthetic tests for 3 different focal mechanisms (gray focal spheres) where the data generated for homogeneous (top) and layered (bottom) models; data are generated for pure DC sources (left), MT sources including 50% positive ISO component (middle), and unilateral upward subvertical 50 m radius finite source models (right). Inversions are performed using the correct and wrong velocity models. Inversion results include the best DC model (thin black line focal mechanism), the decomposed MT (first three values above each focal mechanism indicate DC, CLVD and ISO component percentage). The last value given above the focal mechanism indicate the L^2 norm misfit.

found and the rupture plane remain often poorly resolved, indicating that reliable finite source models require a realistic velocity model. Note, however, that we chose here a challenging setup, inverting for a vertical directivity using surface stations only. Unilateral ruptures along horizontal directions are better resolved with our station configuration. Finally, the inversion results point out that, likely because of the network geometry, we can better resolve finite rupture parameters for specific orientations of the rupture plane, with the best performance (better fit, low spurious non-DC terms, and correct results of the finite source inversion) for the source model with 70° strike. This suggests that the inversion performance may significantly change, depending on the focal mechanisms of different events. Repeating this synthetic events with noise contaminated synthetic seismograms (white noise, 10% amplitude of the maximal amplitude) lead to increased non-DC anomalies, which can be as large as 20% using the correct velocity model and 35% when using the wrong one. The dominant DC components are always well resolved, as well as the orientation of the fault planes.

The second test was carried out using real data. Its main goal is to judge the sta-

bility of inversion results, which we discuss by following a jack-knife approach: we repeated each inversion test 15 times, each time removing one different stations, and discuss the distributions of retrieved source parameters, in comparison to best results, when the inversion is performed using all stations. A second goal is to discuss the reliability of the two chosen models, by discussing spectral fits of real data when computing synthetics for both velocity models. We choose a small data set: six events with variable magnitudes between M_L 0.5 and 1.8, for which reference solutions derived by using P-wave polarities and P-S amplitude ratios [Bischoff et al., 2010b] are available. The inversion is performed in the frequency range 1-4 Hz. Results are shown in figure 3.6. Even if retrieved focal mechanisms are often similar, independently on the chosen velocity model, synthetic spectra computed with a layered velocity model always provide a better fit. Therefore, for the following application to real data, we will only use the layered model. In most cases, DC inversion results are consistent with the reference polarity-based solutions. One exception is event 6, for which both our solutions consistently predict $5°$-$10°$ striking mechanisms (for the steeper plane), different from the reference solution (strike $15°$). A consistent focal mechanism for event 3 is only found for the layered model (using the homogeneous model we found an anomalous mechanism, but also obtain a very poor fit, indicator of the bad quality of the inversion result). The jack-knife test proof that results are very stable for most events, with the exception of event 3; the location of this event at the SW edge of the panel and the asymmetric stations distribution may be responsible for the observed instabilities, when removing some stations from the full stations configuration. Full MT solutions generally show non-DC components. As expected, we find consistent signs of the CLVD and ISO components (solutions in the upper-left or lower-right quadrants). Non-DC component are comparable among inversion results with different velocity models. The jack-knife results are stable in terms of the amount of the non-DC terms, but in some cases their sign is not consistently retrieved, when removing some stations. In addition to these tests, we repeated the inversion of these six events using just broadband and short period stations separately. While amplitude spectra inversion has a similar performance and lead to comparable focal mechanism, time domain inversion indicate that waveform polarities are poorly resolved when using short period stations, where the waveform match become worse as misfit increase. The inversion using broadband stations only always provide solutions which correctly predicts the observed first onsets polarities. Because of these results the focal mechanism polarity (inversion step 2) will be based on the data from broadband stations only. The jack-knife test was also used to evaluate the uncertainties of single MT components, since it is

well known that some components are poorly resolved in certain inversion conditions (for example, M_{xz} and M_{yz}, when inverting low-frequency full waveform signals of shallow earthquakes). In our case, we found that on-trace components are worsely resolved, than off-trace components.

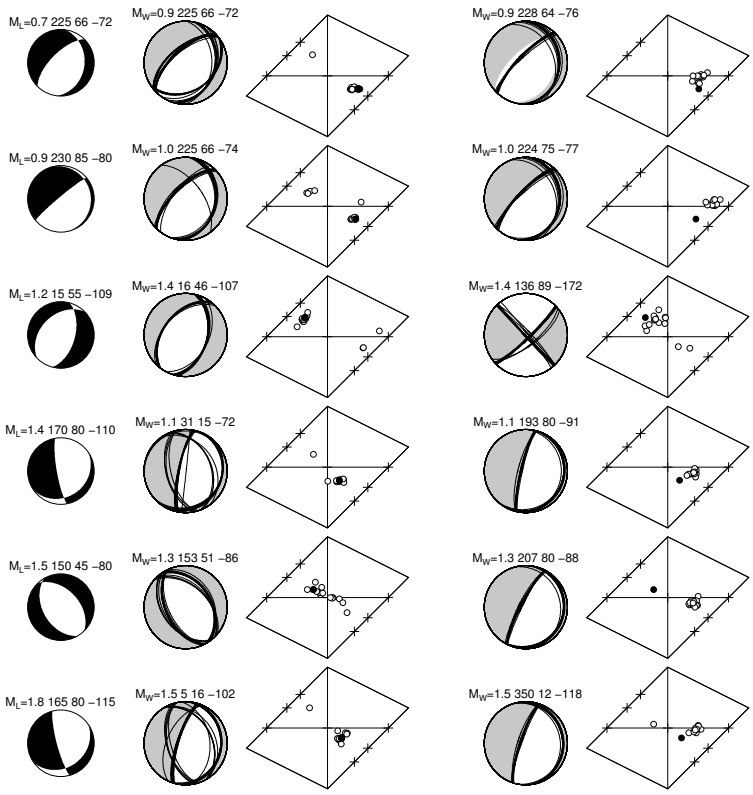

Figure 3.6: Focal mechanisms solutions based on first P onset polarities for six selected events (left, black focal spheres; magnitude, strike, dip and rake are reported above each focal mechanism) are compared with the results of our MT inversion (gray focal spheres; magnitude, strike, dip and rake are reported above each focal mechanism) using a layered (middle) and a homogeneous (right) velocity model. Thin black lines indicate all solutions obtained after the jackknife test. Full MT solutions are discussed using source type diagrams on the side of each solution (black circles denote best solutions, white circles results of the jackknife test)

3.6 Results

We apply the proposed inversion scheme to 3371 events, all events from the catalogue with magnitude above M_L -0.5). Figure 3.7 shows an example amplitude spectra and waveform fits for a selected event (27.11.2006, M_L = 0.7). Results are only discussed for the best 1169 cases, which we consider the most reliable solutions. The selection of best solution was based on the inversion misfits (amplitude spectra misfits below 0.50, waveform misfits below 0.90; note that misfit in the time domain are strongly affected by noise and traces misalignment) and data quality (at least 12 traces available). Since more than 92$\%$ of the focal mechanism has a plane steeper than 45° and a second one shallower than 45°, we can discuss the distribution of fault plane angles (figure 3.8) for the planes with steeper dip angle only. Figure 3.8 shows that most events have similar focal mechanisms, which can be classified in few classes upon their strike angle. Rake angles (Fig. 3.8a) show that most events occur as normal faulting (90$\%$ of the events between -110° and -70° , following Cronin 2004); the distribution is not symmetric and a relevant number of oblique events are found. The plot of the dip angle distribution (figure 3.8b), indicate that for most events the steeper plane is dipping between 50° and 65°. Finally, strike angles highlight different clusters of events, with strike angles of about 70°, 160°, 250° and 310°. This finding can be easier discussed in figure 3.9, where the number of events is plotted along strike-dip, strike-rake and dip-rake diagrams, where families of events with similar focal mechanisms can be better identified. The strike angles of the clusters are fitting with the orientation of the mining walls and stope, which are here indicated by dashed lines. Figure 3.9, bottom, illustrate the temporal evolution of the spatial (Figure 3.9b) and magnitude (Figure 3.9c) distributions within each cluster. Specific patterns characterize different clusters, in terms of the temporal, spatial and magnitude distributions of seismic events. For example, clusters 1 and 4 are more localized in space and time: they almost occur at the beginning and end of the study period, and at the SW and NE edge of the panel, respectively. On the contrary, events of cluster 2 take place during the whole time frame and epicentres are spread in a larger region. Looking at the magnitude distribution (Figure 3.9c), we can see that largest events, with MW larger than 1 occur mostly within clusters 3 and 4.

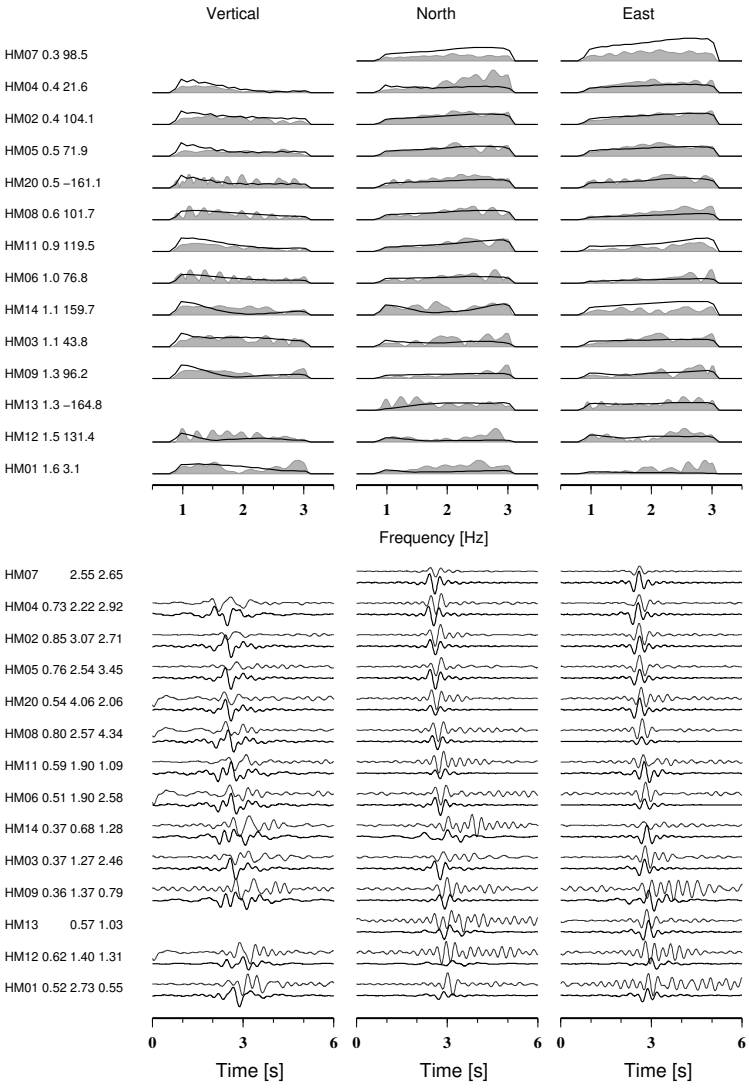

Figure 3.7: Spectra and waveform fit of a real event (2006 November 27 M_L=0.7). Top: comparison of amplitude spectra of observed data (gray) and synthetics (black). Bottom: comparison of displacement seismograms of observed data (grey) and synthetics (black). Station names, distance (km) and azimuth (deg) are given on the upper left-hand side, station names and maximal amplitudes of plotted traces (in 10^{-6} m) on the bottom left-hand side. All shown displacement traces and amplitude spectra are normalized

Full MT inversion has been performed for the same data set (1169 events) to discuss full MT results, we perform its decomposition and plot DC, CLVD and ISO components on a source-type diagram [Hudson et al., 1989]. Figure 3.10 summarizes these results, showing the distribution of full MT mechanisms according to ISO, DC and CLVD percentage and source type plots (figure 3.10). For most events the DC component dominates the deviatoric term (DC is larger than CLVD). The distribution of CLVDs resemble the patterns observed also for natural events For example, see Cesca et al. [2013a], who discussed the distribution of spurious CLVD terms resulting from the limitation of the modelling approach (e.g. because of noisy data or poor knowledge of the velocity model). This would at first suggest CLVD components are spurious terms, only retrieved because of an approximated description of the velocity model, or an unfavourable network geometry. However, the distributions of DC and ISO components provide a different image: most of the events show relevant ISO components, which can account for up to 50% of the energy release. Note that for tectonic earthquakes, the ISO component is often significantly larger than values obtained in synthetic tests. The centre of the source type plot is underpopulated, indicating few pure DC events, whereas most events are characterized by a combination of shear and tensile cracks. In most cases (more than 60%), we observe opening cracks (combination of positive ISO and positive CLVD) rather than closing ones (negative ISO, negative CLVD, about 30%). This clear predominance seems quite reliable, despite the polarity resolution problem highlighted by the jack-knife test. Only in few cases (less than 10%), we have ambiguous ISO and CLVD signs.

From the spectral analysis performed for a random subset of events, with magnitudes ranging between M_W 1.0 and 1.8, corner frequencies were estimated approximatively between 3 and 15 Hz. Corner frequencies derived from S phase spectra for different magnitudes are slightly higher than those derived using P waves. Low corner frequencies (for the given magnitude range) and a low ratio between P and S waves corner frequencies suggest that the failures occur with a slow rupture velocity [Kwiatek et al., 2011], which could help the resolution of finite rupture parameters. Based on this findings, in the following kinematic inversion, we have chosen a rupture velocity of about 1.4 km/s , which is 0.7 times the S-wave velocity at the source depth, as estimated from the local layered velocity model (figure 3.3). Kinematic source model inversion was then carried out for 158 events, all events with $M_L \geq 1.0$ and with a reliable point source solution. When limiting the inversion to the lowest frequencies, below the corner frequency, extended source models cannot be investigated, and both point and kinematic source

model fit equally well the observed amplitude spectra. For the range of considered magnitudes and the spectral analysis, the inversion with frequencies up to 10 and 20 Hz should have the potential to resolve finite source parameters, at least for largest events. However, in most cases (84% for 1-10 Hz, 57% for 1-20 Hz) the best finite source solutions have the smallest tested size, which make them equivalent to a point source (the discretized extended source model is composed by a single point source). For the remaining cases, when a larger size is found (in general a radius of 25 m), subvertical fault planes are preferred to subhorizontal ones. This result is found consistently for both frequency ranges: the subvertical planes are preferred in 64 per cent of the cases, for a bandpass 1-10 Hz, and in 81% of the cases, when including frequencies up to 20 Hz. No clear directivity pattern is resolved. Finally, it should be noted that the estimation of the rupture sizes is strongly biased by the adoption of a given rupture velocity: in general, after testing the adoption of different rupture velocities, we observed a trade-off between rupture velocity and rupture radius, which makes difficult to discriminate between larger and faster source models, and smaller and slower ones.

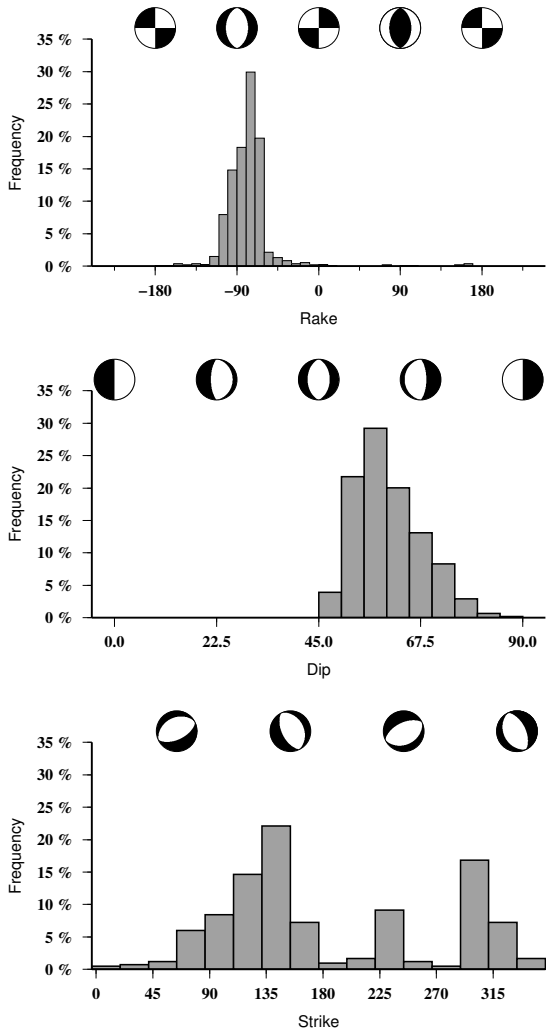

Figure 3.8: Distribution of DC solutions for fault plane angles for the steepest plane: rake (a), dip (b) and strike (c) distributions.

3.7 Discussion

The overall performance of the proposed point source inversion scheme indicates that our approach can be successfully used to automatically analyse large data sets in mining environments, and demonstrate the potential application of the Kiwi tools for local data sets and micro seismicity data. Different from most source inversion techniques typically adopted in mining monitoring, our method relies on the fit of the full waveform, rather than only on the body- wave polarities. The performance of the first inversion step in the frequency domain (amplitude spectra) allows us to ignore problems associated to waveform alignment and reduces the effects due to wave propagation mismodelling and the adoption of simplified layered models. The method performance may be limited in presence of strongly heterogeneous media, where the adoption of 1-D models may be improper. Other cases where we expect a worse performance for mining environments includes the simultaneous occurrence of different events or the case of specific processes, such as rockfalls, where the energy is released over a longer time and with a complex source time function. The method has the potential to be extended to consider wave propagation in 3-D media, upon a reconfiguration of the Green function database. Another possible expansion, which should benefit the inversion stability, is the inclusion of surface and in-mine sensors, which would improve the coverage of the focal region.

The amount of inversion results make unfeasible a manual analysis of all event solutions, and some outliers in the MT catalogues cannot be excluded. Therefore, we chose here to discuss the best results and the average patterns of source parameters, when most events lead to similar results. This allowed us to draw general conclusions concerning the seismicity patterns. In this way, we could highlight that most events repeatedly occur with similar mechanisms, correlated with the mining geometry, and could define on this base few clusters of events. A similar approach was used to point out the presence of a significant non-DC components, indicating mostly positive tensile cracks in addition to shear crack. The reliability of these terms is supported by the fact that ISO and CLVD components generally have a consistent signs, and confirmed by the performance of synthetic data sets inversions. Finally, synthetic tests confirmed that spurious non-DC are also not artifact obtained in consequence of a point source approximation to finite source ruptures with specific rupture patterns (e.g. a repeated directivity or rupture plane orientation).

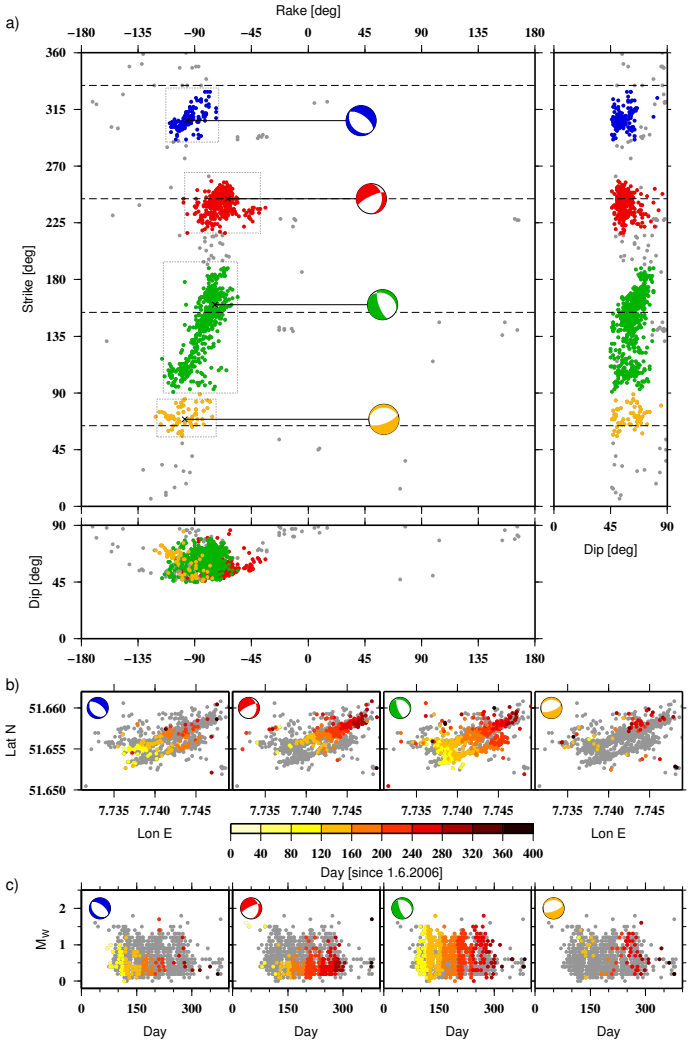

Figure 3.9: (a) The number of events along strike-rake, dip-rake and strike-dip plots highlights four clusters (dotted squares) of events with similar DC focal mechanisms (coloured focal spheres). Clusters show similar normal faulting, but different strike orientations, which are consistent with the orientation of mining walls (dashed lines). (b) Spatiotemporal distribution of the four clusters and (c) Temporal evolution of the magnitude distribution of the four clusters.

Finite source inversion on the available data set was a very challenging task, even when limited to the largest events. The fact that most preferred solutions are consistent with point sources or indicating small size ruptures (radii below 50 m) highlights the limitations of our resolution. These results indicate that synthetic seismograms, generated with 1-D models, are not able to reproduce observed high frequencies and the 1-D velocity model is not realistic enough to test frequency above 10 Hz. The adopted rupture velocity plays also a role in the estimation of rupture size, since fast larger ruptures and slow small ruptures produce similar waveforms and such source models may not be distinguished. Slow rupture processes are supported by the detection of seismic energy at low frequency and the estimations of spectra corner frequencies. Even though single finite source inversion may not be considered reliable, the overall analysis of finite source models point out some common patterns, such as the preference for subvertical faults, rather than the subhorizontal ones. Given the local stratigraphy, with presence of different seams and layers, Bischoff et al. [2010a] proposed that the brittle failure associated to induced events only occur within thin layers. We compare therefore two finite source inversions, using the features of the eikonal source model: in the first case, we use the unbounded circular-shaped model, and in the second case, we bound it above and below the centroid depth, within a depth thickness of 20 m, to reproduce the failure of thin subhorizontal layers. The geometry of the seismogenic layer leads to a range of source geometries within two extreme cases: a line source model, when the rupture plane is almost vertical, and a circular model, when the rupture plane is horizontal. Main results are illustrated in figure 3.11, when the results of eikonal and bounded eikonal source misfits are compared to the point source ones (for bandpasses 1-10 and 1-20 Hz). Although finite source models can better fit the spectra, the improvement is often minor and do not significantly perform better than point source models. The comparison of eikonal and bounded eikonal sources indicate a slight preference for unbounded (circular) source models, but again the differences among fits are minor.

According to Hedley & Wetmiller [1985], comminuted fracturing and faulting processes, also referred to as strain energy burst, is a common process affecting intact rocks in mines. Fracturing takes place as a normal fault, along subvertical planes in proximity of mine faces, and above the mining level. Comminuted faults are considered among the most common types of faulting in mines [Hasegawa et al., 1989]. Our results, both in terms of source locations, focal mechanisms and preferred rupture plane geometry, suggest that this fracturing processes are also

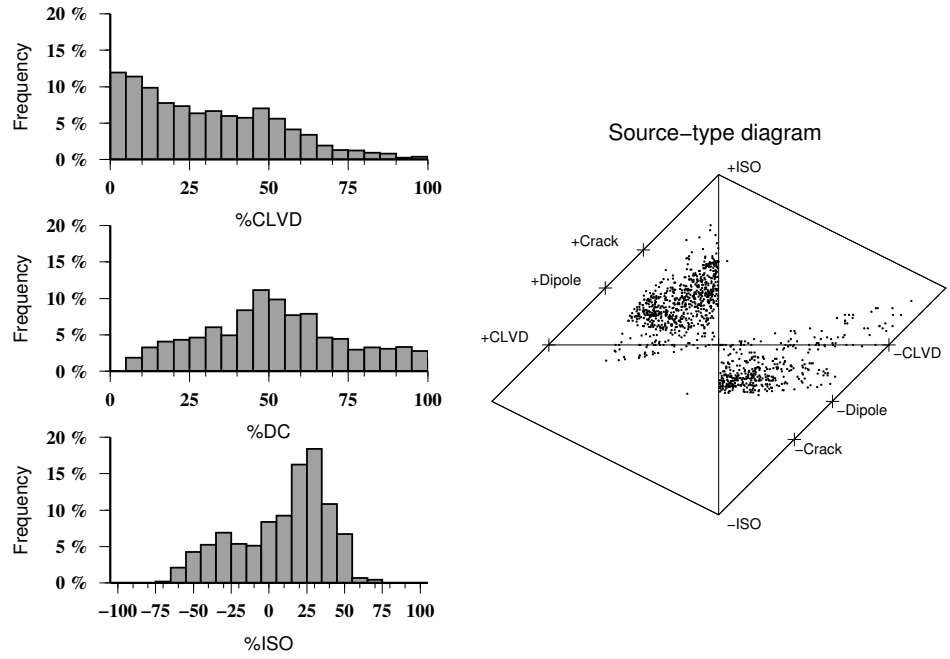

Figure 3.10: Left: distribution of decomposed terms (DC, CLVD, ISO) after full MT inversion. Right: source type plots are shown for each single event (black circles).

dominant in our study area.

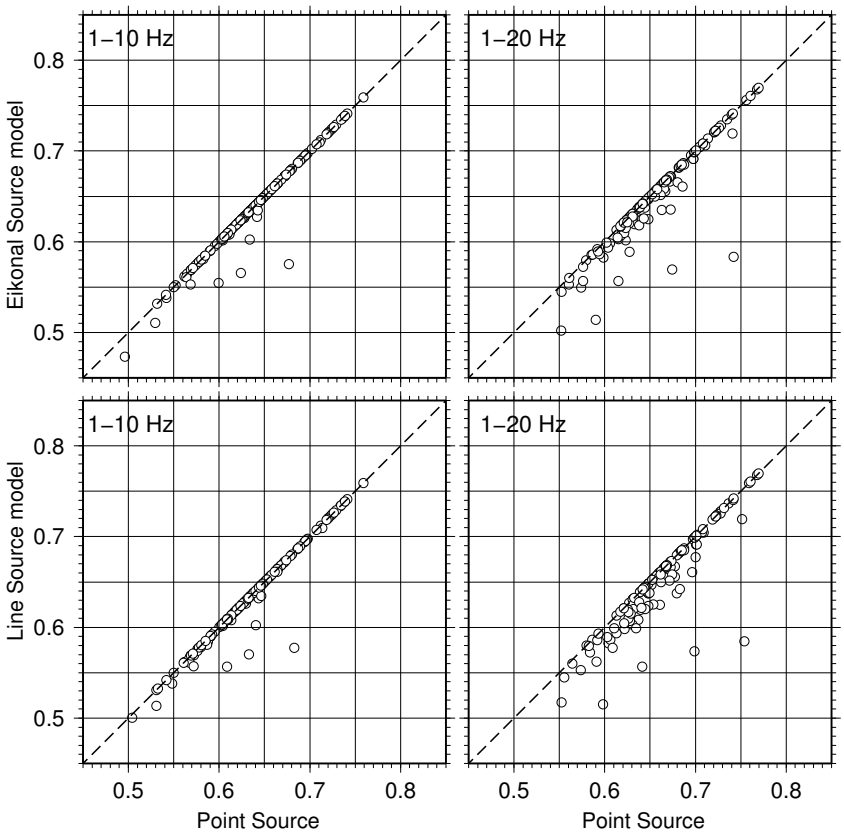

Figure 3.11: Top: misfit comparison among unbounded (circular) and bounded (line) eikonal finite source models inverted in the 1-10 Hz (left) and 1-20 Hz (right) frequency range. Bottom: misfit comparison among the bounded eikonal source model and the point source model in the 1-10 Hz (left) and 1-20 Hz (right) frequency range. Each point corresponds to an event. Dashed lines highlight equal misfits.

Source model solutions can be classified into different clusters with similar source models, e.g. according to the orientation of the DC planes, the sign of the tensile crack component, or the determination of preferred kinematic solutions along the subhorizontal or subvertical plane. The availability of large focal mechanism data sets can be then used to investigate whether any of these source features can be related to the observed anomalous FMD and thus used to discuss its origin. FMDs are here discussed on the basis of MW magnitude estimations, the outcome of our inversion, rather than on the original ML values. Figure 3.12 shows the cumulative and non- cumulative distribution from the entire data set (top) for which we obtain reliable solutions, as well as FMDs based on subsets (bottom), according to two classification approaches: in the first case subsets are based on the focal mechanism clusters derived in the analysis of DC point sources (see figure 3.9), in the second case based on the sign of the tensile component. Results from the first approach highlight different FMDs for different DC models. Clusters 1 (blue) and 2 (red) show a similar behaviour, following a Gutenberg Richter distribution, with a completeness magnitude of about M_W 0.3. They include no events with magnitude above M_W 1.5. Events from clusters 3 and 4 (green and yellow circles) show an anomalous pattern, similar for both families of events, with a significant number of large events above M_W 1. The distributions do not fit the expected Gutenberg-Richter relation, unless considering an unrealistic high magnitude of completeness and low b-values, In general the superposition of two main families of events, clusters 1 and 2, and clusters 3 and 4, with different FMDs are responsible for the observed overall bimodal distribution of this coal mining-induced seismicity data set.

Source model solutions can be classified into different clusters with similar source models, e.g. according to the orientation of the DC planes, the sign of the tensile crack component, or the determination of preferred kinematic solutions along the subhorizontal or subvertical plane. The availability of large focal mechanism data sets can be then used to investigate whether any of these source features can be related to the observed anomalous FMD and thus used to discuss its origin. FMDs are here discussed on the basis of M_W magnitude estimations, the outcome of our inversion, rather than on the original M_L values. Figure 3.12 shows the cumulative and non- cumulative distribution from the entire data set (top) for which we obtain reliable solutions, as well as FMDs based on subsets (bottom), according to two classification approaches: in the first case subsets are based on the focal mechanism clusters derived in the analysis of DC point sources (see figure 3.9), in the second case based on the sign of the tensile component. Results from the

first approach highlight different FMDs for different DC models. Clusters 1 (blue) and 2 (red) show a similar behaviour, following a Gutenberg-Richter distribution, with a completeness magnitude of about M_W 0.3. They include no events with magnitude above M_W 1.5. Events from clusters 3 and 4 (green and yellow circles) show an anomalous pattern, similar for both families of events, with a significant number of large events above M_W 1. The distributions do not fit the expected Gutenberg-Richter relation, unless considering an unrealistic high magnitude of completeness and low b-values, In general the superposition of two main families of events, clusters 1 and 2, and clusters 3 and 4, with different FMDs are responsible for the observed overall bimodal distribution of this coal mining-induced seismicity data set.

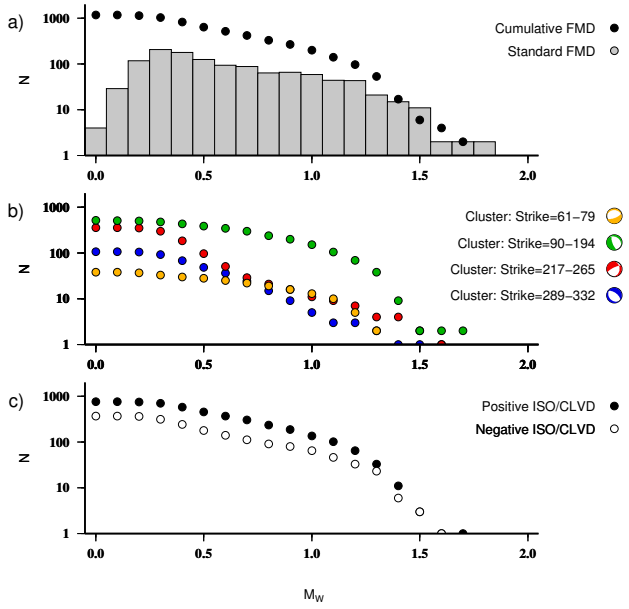

Figure 3.12: Overview of the FMD for different source classifications. (a) Cumulative (black dots) and standard (gray histograms) FMDs for the studied 1169 events. Bottom: cumulative FMDs after clustering the events respect to: (b) strike angle (colour dots according to the coloured focal mechanism, see also figure 3.6), (c) sign of the tensile/ ISO component (black dots for positive tensile/ ISO components, white dots for negative ones).

Our results are not sufficient to discriminate whether the overall FMD is only a consequence of structural heterogeneities or only a response to different acting stresses. The first hypothesis cannot be fully investigated, since large uncertainties on source locations limit the interpretation of the correlation between subsets locations and different structural bodies. The alternative hypothesis for the observed FMDs, based on the combined effects of tectonic and induced stresses, could fit to our findings, since focal mechanisms of different orientations have different likelihood to take place depending on the acting stresses. However, local stresses are poorly known, and therefore this hypothesis cannot be further assessed. The proposed approach for the focal mechanism classification and the following analysis of FMD for classes of subevents with a similar mechanism could be used in other environments (e.g. swarms, volcanoes), where deviation from the Gutenberg-Richter law is observed.

3.8 Conclusions

We propose an automated full waveform inversion approach, coupling amplitude spectra and displacement waveform inversion, to derive point and extended source models at very local distances, feasible for micro seismicity and mining-induced seismicity analysis. After testing different stations configurations, velocity models and inversion parameters (e.g. frequency band), full waveform MT inversion was successfully applied to more than 1000 mining-induced events following longwall mining in a coal mine in Germany. Data recorded at a local scale ($\leq$2 km) by a combination of broadband and short period stations, were used to derive source parameters for low magnitude events down to M_L -0.5. The automated inversion process was applied to 3371 events and provided good spectral fit and reliable DC and full MT solutions for 1169 of them. Major conclusions can be summarized as follows:

DC solutions are in good agreement with reference solutions, based on first polarities and S wave polarization, when available (about 100 events). A layered velocity model better reproduces observations than a simplified homogeneous model. Best results are obtained when fitting amplitude spectra and displacement traces in the range between 0.5 and 4 Hz. Focal mechanisms show similar style of faulting: a very large majority shows normal faulting, with one steep fault plane.

Strike angles are parallel to the advancing mining stope or to the mining walls. Full MT inversion results shows that most of the events deviate from a pure DC model and include an opening crack component. Kinematic inversion results suggest that slow ruptures occur in most cases along the steeper fault. However, finite source parameters are poorly resolved. Events have been classified in different clusters according to their source parameters: the observed bimodal FMD is better explained by clustering the events according to their fault plane orientations.

3.9 Acknowledgements

We are thankful to the Ruhr University Bochum and to all researchers involved in the installation and handling of the local network, for monitoring and providing access to data used in this study. This work has been funded by the project MINE. The project MINE is part of the R&D-Programme GEOTECHNOLOGIEN, The MINE project is funded by the German Ministry of Education and Research (BMBF), Grant of project BMBF03G0737.

Chapter 4

Seismicity Monitoring By Cluster Analysis of Moment Tensors

Authors:
Simone Cesca[1,2], Ali Tolga Sen[2], Torsten Dahm[1,2]
Journal:
Geophysical Journal International
Status: Published
doi: 10.1093/gji/gji492

Authors affiliation:
1) GFZ (German Research Centre for Geosciences) Potsdam,
Section 2.1, Physics of earthquakes and volcanoes,
Potsdam, Germany
2) Institute of Earth and Environmental Sciences,
University of Potsdam, Potsdam, Germany

4.1 Abstract

We suggest a new clustering approach to classify focal mechanisms from large moment tensor catalogues, with the purpose of automatically identify families of earthquakes with similar source geometry, recognise the orientation of most active faults, and detect temporal variations of the rupture processes. The approach differs in comparison to waveform similarity methods since clusters are detected even if they occur in large spatial distances. This approach is particularly helpful to analyse large moment tensor catalogues, as in microseismicity applications, where a manual analysis and classification is not feasible. A flexible algorithm is here proposed: it can handle different metrics, norms, and focal mechanism representations. In particular, the method can handle full moment tensor or constrained source model catalogues, for which different metrics are suggested. The method can account for variable uncertainties of different moment tensor components. We verify the method with synthetic catalogues. An application to real data from mining induced seismicity illustrates possible applications of the method and demonstrate the cluster detection and event classification performance with different moment tensor catalogues. Results proof that main earthquake source types occur on spatially separated faults, and that temporal changes in the number and characterization of focal mechanism clusters are detected. We suggest that moment tensor clustering can help assessing time dependent hazard in mines.

4.2 Introduction

Moment tensors are the most common and general representation of seismic sources, under the assumption of a point source approximation. A moment tensor is mathematically represented by a second-rank symmetric tensor, which is fully described by its 6 independent components [e.g. Aki & Richards, 1980]. Additional source constraints are often assumed, which reduces the number of independent variables. Source volume changes for natural earthquake source are generally considered negligible, and the isotropic source term neglected; isotropic source components are typically considered only for certain applications, e.g. in volcanic [e.g. Cesca & Dahm, 2008; Cesca et al., 2007, 2008; Chouet et al., 2003; Davi et al., 2010; Kaneshima et al., 1996; Legrand et al., 2000; Lokmer et al., 2007; Panza et al., 1993; Sarao et al., 2001], geothermal [Boyd et al., 2011; Kravanja

et al., 2000; Panza et al., 1993; Panza & Sarao, 2000; Ross et al., 1999] or mining [Cesca et al., 2013b; Feignier & Young, 1992; Fletcher & McGarr, 2005; Foulger & Julian, 1993; Julià et al., 2009; Kühn & Vavryčuk, 2013; McGarr, 1992a,b; Şen et al., 2013; Trifu et al., 2000; Vavryčuk & Kühn, 2012] environments, where changes in volume at the source may take place in consequence of multi-phase processes, explosions and collapses. Volumetric source changes have been also considered for deep focus earthquake [Buforn et al., 2011; Frohlich, 1995; Kuge & Kawakatsu, 1990, 1992, 1993]. The isotropic component is uniquely derived from the moment tensor, through its decomposition into isotropic and deviatoric terms [e.g. Jost & Herrmann, 1989], and the deviatoric part further decomposed. The most widely adopted (Julian et al. 1998) is by far the superposition of a double couple (DC) source and a compensated linear vector dipole (CLVD) according to Knopoff & Randall [1970]. A further assumption of negligible CLVD brings to the description of the source by a pure double couple, a model often used to represent the radiation pattern of a shear failure at the earthquake focus. A DC point source is generally described by means of the scalar moment and the fault plane angles (strike, dip, rake), rather than by constrained moment tensor components.

In the last decades several codes have been proposed to invert the earthquake moment tensor. Early applications to large earthquakes at teleseismic distances leading e.g. to the Global CMT calatog [Dziewonski et al., 1981; Ekström et al., 2012] have been later extended or adapted for the analysis of regional seismicity [e.g. Bernardi et al., 2004; Giardini et al., 1993; Pondrelli et al., 2002; Ritsema & Lay, 1993; Stich et al., 2003] and weak seismicity at local distances [e.g. Şen et al., 2013]. As a result, moment tensor catalogues are routinely generated for the whole earth and for specific regions. Moment tensor inversion, with different source constraints, is carried out by minimizing residuals between observations and synthetics, with the observation being either first onset polarities, bodywaves amplitudes, amplitude ratios, full waveforms or amplitude spectra. Possibly, the most common approach is to invert low frequency full waveform in the time domain to retrieve a deviatoric moment tensor. Polarity based approach, as well as studies to analyse the geometry of fault systems, are often carried out using a DC source representation. Finally, for specific applications (e.g. in volcanic, geothermal and mining environments), full moment tensors are inverted.

If the analysis of focal mechanisms for single events or a limited number of earthquakes can be easily evaluated to discuss the fault geometry or to invert for local stresses, the automated analysis of large moment tensor catalogues require the

setup of specific tools. These should be able to automatically recognise the most dominant source characteristics of the target seismicity, identify families of events with similar focal mechanisms, and share the earthquake catalogue according to the chosen classification. We propose here to use clustering techniques to this purpose. Data clustering is the task of assigning a set of objects into clusters, which are group of objects similar among them. Event clusters are not predefined, but automatically detected through the cluster analysis. A broad range of clustering techniques have been proposed in the past, and applied to a very broad range of scientific fields; a wide literature describes different techniques and corresponding algorithms. In this paper we limit the discussion to the use of a density-based clustering algorithm, namely DBSCAN, and combine it with the definition of different metrics, which can be used to define the distance among source models, according to different moment tensor representations. Clustering approaches have been used in seismology so far mostly to recognise events patterns and identify foreshocks and aftershocks based on the spatial location (Konstantaras et al. 2012; Ouillon and Sornette 2012; Lippiello et al. 2012), temporal evolution [Hainzl et al., 2000; Kagan & Knopoff, 1976; Kagan & Jackson, 1991] or on the analysis of spatiotemporal distribution of seismicity [Hainzl et al., 2000; Sornette & Werner, 2005]. Waveforms similarity has also been used for clustering approaches [Cattaneo et al., 1999; Maurer & Deichmann, 1995; Wehling-Benatelli et al., 2013]; however, since similar waveforms are observed when both the source radiation patterns (i.e. the focal mechanism) and the source locations are similar, the approach and expected classification results are different to those here discussed. Finally, focal mechanism clustering have been proposed by Willemann [1993], which tested hierarchical clustering techniques to classify focal mechanisms using a moment tensor representation. Following the developments of moment tensor inversion techniques and new clustering techniques in the last decades, we extend the former approach by Willemann [1993] through the adoption of DBSCAN clustering, the comparison of different metrics for different source representations, and the discussion of moment tensor inversion uncertainties within the clustering framework. Moreover, we discuss the application of moment tensor clustering to monitor the temporal evolution of seismicity, in order to detect the appearance of anomalous rupture processes improving seismic hazard assessment. This is extremely important e.g. in mining, geothermal, gas/oil and water reservoirs exploitation environments, where different geoengineering operations can strongly modify the characteristics of fracturing processes.

4.3 Methodology, Clustering Method

Clustering techniques are devoted to the automated classification of object into classes, or clusters, characterized by similar objects. Any clustering technique requires the definition of a metric, to be used to evaluate the similarity (or dissimilarity) among the objects within the studied dataset. Several techniques have been proposed in the last decades. They may lead to different clustering results depending on adopted algorithms and parametrizations. We adopt here a density-based clustering approach, DBSCAN [Ester et al., 1996]. DBSCAN, as a density-based clustering technique, is based on the observation that data clusters are characterized by a high density of points (in this case, moment tensors), much higher than outside of the cluster, and that outliers are sparsely distributed, in regions of much lower density than for any cluster. Such an approach will identify a cluster as a densely populated region, with no constraints on its shape. The inclusion of a point in a cluster with DBSCAN is based on the concept of density reachability, which is here briefly recalled [for more details, see Ester et al., 1996]. It is likely that the cluster will be more densely populated in its inner part and less populated at the edge. From this consideration, DBSCAN defines core points those ones located in a dense region: formally, a core point has a sufficient number of points (N_{min}) in its neighbourhood (which is defined on the base of a threshold distance, ϵ). Points located in the neighbourhood of the core point are defined as directly-reachable from the core point. If such target points are still located in a dense region, they are also identified as core points of the cluster. Otherwise, when they are in a more sparse region, they are defined as border point and will result at the edge of the cluster. The neighbourhood of a border point is much less populated than the one of a core point, nevertheless the border point still pertains to a cluster, because it is directly-reachable from a core point. Following the DBSCAN formalism, all points of a cluster are then said density-reachable, and the cluster densely-connected. Core point can be identified by checking the populations in their neighbourhood. Each of them can create a cluster, together with the points in their neighbourhood. Connected clusters will be merged into single clusters. Points with sparsely populated neighbourhood and which are not densely-reachable by any core point will be identified as noise. The performance of DBSCAN is entirely controlled by two parameters: the threshold value ϵ, which defines the maximal distance at which a target event is considered directly reachable from a core point, and Nmin, which is a measure of the density of a given region, defined as the minimum number of the points which have to be situated within the distance range. N_{min} is also a constraint for the minimal size of a

cluster. DBSCAN has several qualities, which make it appealing for the aim of clustering focal mechanisms and moment tensor solutions. First of all, the algorithm has the concept of noise, so that not all events have to be part of a cluster. This feature is important to treat outliers, which are likely present in a moment tensor catalogue, but may not be easily identified for large catalogues. A second, relevant features is its stability against the sorting of the input catalogues, whereas other methods may provide different clustering results depending on the way the original catalogue is sorted. This feature make the clustering result unique, at least with respect to the catalogue sorting. Finally, DBSCAN does not require a predefined number of clusters, a feature which is anyhow common to many other algorithms. As a drawback, DBSCAN may be unable to separate close clusters, unless through a precise tuning of its parameters, and Nmin. Moreover, the choice of these parameters is somehow subjective and can affect the number, size and heterogeneity of identified clusters. The problem is further discussed in the following section on synthetic tests. Previous attempts to cluster moment tensor solutions [Willemann, 1993] only made use of hierarchical clustering techniques; density-based techniques such DBSCAN have never been used before to this purpose. The DBSCAN technique has been implemented within our software, making use of a suitable python library within scikit-learn [Pedregosa et al., 2011]

4.4 Methodology, Distance Between Moment Tensors

Different distances among moment tensors have been proposed in previous studies [Kagan, 1991, 1992; Tape & Tape, 2012; Willemann, 1993] and will be here discussed and further extended. The Kagan angle approach [Kagan, 1991, 1992] aims to describe the difference among pure DC source models. It has the beauty to be intuitive, as it is based on the transformation of a DC focal mechanism into a second one through rotations. Using the quaternion convention, a single rotation is sufficient and the rotation angle (later referred as Kagan angle) can be used as a measure of this distance. In order to have a distance d ranging [0,1], the rotation angle is here divided by 120^0, which is the maximal possible Kagan angle among two DC focal mechanisms (note that in the following plots, a similarity coefficient is defined as 1-d, so that the value 1 is assigned in case of maximal similarity):

$$d = \xi_0/(2\pi/3) \tag{4.1}$$

where ξ_0 is the Kagan angle (see Kagan [1992] for details on its computation).

The other considered metrics are more general and based on a moment tensor representation. They are thus useful to compare full and deviatoric moment tensor mechanisms, but can also be used for pure DC cases. Willemann [1993] proposed to use coherence, where similarity is assessed on the base of the cosine angle among vectors composed by moment tensor components. A cosine-based approach was also proposed in Tape & Tape [2012], where the formalism is more suited to build a distance definition which ranges between 0 and 1. Upon Eq. 67 in Tape & Tape [2012], we can define the distance among two moment tensors M and N (with elements mij and nij respectively) as:

$$d = \frac{1}{2}[1 - \frac{M \cdot N}{\|M\|\|N\|}] = \frac{1}{2}[1 - \frac{\sum m_{ij} n_{ij}}{(\sum m_{ij}^2)^{1/2} (\sum n_{ij}^2)^{1/2}}] \tag{4.2}$$

with summation over both indices. The distance is computed using the standard inner product in $\mathbb{R}^9$. Considering that moment tensor are characterized by 6 independent moment tensor components, which are the typical output of moment tensor inversions, the following modification of the previous distance could be considered:

$$d = \frac{1}{2}[1 - \frac{\sum m_i n_i}{(\sum m_i^2)^{1/2} (\sum n_i^2)^{1/2}}] \tag{4.3}$$

where m_i and n_i are the independent components of moment tensors and the inner product is performed in $\mathbb{R}^6$. Other possible metrics, treating the independent moment tensor components as vectors could make use of normalized L_1 and L_2 norms.

Figure 4.1 illustrates the distance increase with respect to a reference DC model (normal faulting, strike $0°$, dip $45°$, rake $-90°$). The first cases (figure 4.1a-d) refer to DC perturbations, by increasingly change the strike, dip, rake or the three

angles at a time. The Kagan angle shows some nice features: it has a linear relation with the rotation angle and the same rotation of strike, dip or rake angles lead to the same distance. The adoption of the Kagan angle for focal mechanism comparison was criticised by Willemann [1993], upon the fact that focal mechanisms with opposite polarities are not considered the most dissimilar (the Kagan angle among them is $90°$, whereas the maximal Kagan angle value is $120°$). However, the maximal Kagan angle is found for focal mechanisms pairs, which can be considered even more dissimilar in terms of rupture geometries: for example, certain pairs of normal and thrust mechanisms with perpendicular strikes.

The remaining tested distances (see figure 4.1) do not accomplish the previous properties of the Kagan angle distance. The only exception is the cosine distance in $\mathbb{R}^9$, which shows a linear behaviour with the rotation angle, but still differ for common variations of strik, dip and rake angles. However, these distances remain useful, at least, for the case of full and deviatoric moment tensors, where the Kagan angle cannot be used. Figure 4.1e-f illustrates this case, showing how the L^1, L^2 and cosine distance perform, when the original focal mechanism is perturbed through the inclusion of increasing CLVD (Figure 4.1e) and isotropic (Figure 4.1f) components. Note that maximal perturbed cases correspond to pure CLVD and ISO sources. Cosine distance in $\mathbb{R}^9$ and $\mathbb{R}^6$ have the same performance, because off-trace components are invariant for the selected range of moment tensors.

It is worth to note that all these distance makes no use of uncertainties of the moment tensors solutions. Moment tensors are typically the results of specific inversion routines, based on the fit of a part of the seismic data (e.g. polarities, amplitudes, waveforms), and relying on variable datasets and limited knowledge of wave propagation. They are significantly affected by several factors, including the source depth, the network geometry, the signal quality, the simplified adopted velocity models, and the inversion framework. As a consequence, moment tensor solutions may have relevant uncertainties: however, these are typically not comparable for all moment tensor components. For example, Henry et al. [2002] showed that M_{xz} and M_{yz} components are poorly resolved for shallow earthquakes using low frequency full waveforms, because their Green's functions vanish at the free surface. Bukchin et al. [2010] showed how this can lead to ambiguous focal mechanisms solutions. Du & Warpinski [2011] discussed the effects of moment tensor uncertainty effects on fault plane solutions for microseismicity studies. In other

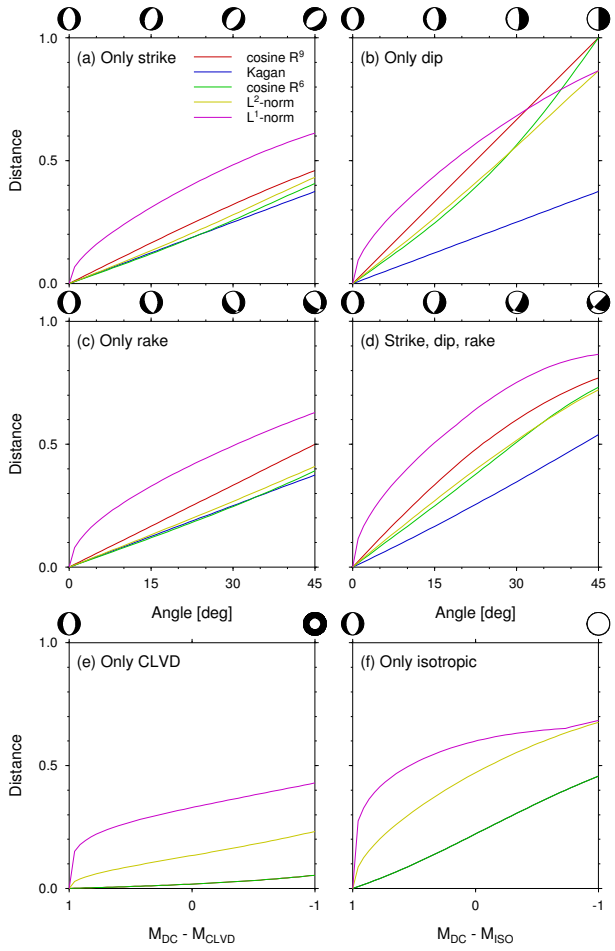

Figure 4.1: Performance of difference distance definitions. Distances are computed for five metrics (colours according to the legend in the top left-hand plot), among a reference pure DC focal mechanism (strike $0°$, dip $45°$ and rake $-90°$) and perturbed mechanisms. DC focal mechanisms perturbations (top) are obtained by rotating progressively (see focal spheres) the reference mechanisms up to $45°$ of strike (a), dip (b), rake (c) and all three (d) angles. Perturbed mechanisms including non-DC components are shown in the bottom plots for four metrics (the Kagan angle is not applied as it cannot handle). Mechanism perturbation is performed by adding increasing CLVD (e) and ISO (f) components, in a way that moment tensor remain normalized; most perturb cases correspond to pure CLVD and ISO mechanisms.

cases, because of the source-network geometry and the inversion approach, the distribution of uncertainties may be different. The problem is here illustrated for the coal mining induced seismicity dataset, which will be analysed in the following of this work. Moment tensor components uncertainties have been here

assessed using synthetic tests. We considered events with different locations (epicenters at the edges of the mined area where the seismicity is concentrated, see Grigoli et al. [2013]) and typical focal mechanisms (normal faulting parallel to mine walls and stope, see en et al. 2013). For each reference mechanism and location, we estimated the misfit increments, when perturbing separately each single MT component of the original focal mechanisms by 20%; misfits were computed among amplitude spectra using an L2 norm, reproducing the exact inversion conditions as for the derivation of the MT catalogue. A small misfit among the true and perturbed mechanism indicates a worse condition to discriminate among both source model, thus pointing to a larger uncertainty on the tested MT component. Results are illustrated in Figure 4.2: although results slightly change when considering variable locations and reference mechanisms, these variations are minor, compared to those among MT components. In particular, horizontal dipoles M_{xx} and M_{yy} are the least resolved components, whereas M_{xz} and M_{yz} are the best constrained. Similar results were also found on the base of the distribution of MT results from a jack-knife analysis, considering a very limited dataset composed of 6 selected events [Şen et al., 2013].

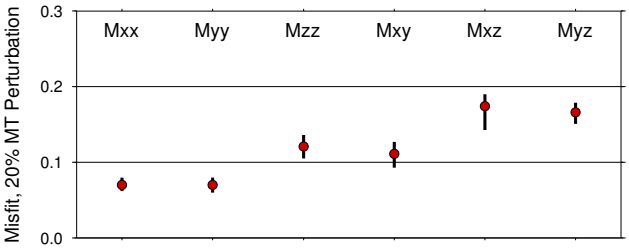

Figure 4.2: Mean values (red circles) and range of values (black bars) of misfits obtained when comparing original amplitude spectra and synthetics for perturbed moment tensors, following the inversion approach used by Şen et al. [2013]. The figure illustrates the overall result of repeated tests, considering different locations and focal mechanisms. Smaller misfits, corresponding to larger MT component uncertainties, can be used as weights for the weighted MT clustering approach.

On the base of these considerations, moment tensor components uncertainties should be accounted in the definition of the distance. Adopting the cosine-distance, we propose to use the following equation:

$$d = \frac{1}{2}[1 - \frac{\sum w_i^2 m_i n_i}{(\sum w_i^2 m_i^2)^{1/2}(\sum w_i^2 n_i^2)^{1/2}}] \tag{4.4}$$

where each w_i is a weighting factors for a moment tensor component i. Weighting factors can be defined e.g. as reciprocals of uncertainties. Note that distances defined according to [Tape & Tape, 2012; Willemann, 1993], as in Eq. 4.2, as well as Eq. 4.3, are specific cases of Eq. 4.4, upon certain weights selection. A similar weighting approach can also be applied to L^1 and L^2 norm distances. It is important to remind that the proposed weighting scheme, assigning fixed weights to single MT components, should only be used if the distribution of uncertainties is similar for the whole considered dataset. It is possible, in fact, that MT component uncertainties vary among events with different locations, depths, focal mechanisms or magnitudes. The weighting scheme should in any case be tested when considering seismogenic region which are large in comparison to the network, or if strong network changes took place during the catalogue time (a temporal evolution of the network could affect MT uncertainties in different time spans). An alternative approach, when the moment tensor catalogue is dominated by moment non-DC terms, e.g. in presence of tensile cracks with dominant tensional (or compressive) CLVD, a different approach could be considered, with a distance mostly based on the similarity among tension (or pressure) axis orientations, and down-weighting the poorly resolved orientation of the remaining axis.

Cluster mean parameters can be obtained for each cluster. They should be computed on the base of the distance definition adopted for the clustering. The mean parameters should ensure the minimization of the sum of the distances to cluster members. For the Kagan angle definition, the mean triple (strike, dip, rake; in the following with the notation ϕ, δ, λ) can be obtained by scanning the whole space of possible triples (ϕ, δ, λ), to find the triplet for which is minimized the summed Kagan distance over the n members of the cluster:

$$(\bar{\phi}, \bar{\delta}, \bar{\lambda}) = \{(\phi, \delta, \lambda) : \sum_{i=1,n} \xi_0((\phi, \delta, \lambda)(\phi_i, \delta_i, \lambda_i))\} \tag{4.5}$$

where the scan of the triples can be optimized upon the distribution of strike, dip and rake of cluster members. For cosine-based definitions, included weighted ones, averaging of moment tensor components provides the searched mean values.

4.5 Synthetic Tests

Prior to the application to real data, we discuss the performance of the proposed clustering technique on a synthetic moment tensor dataset. The synthetic catalogue is composed of 500 events, with the following dominant mechanisms: (1) 20% are close to pure DC mechanism with normal faulting of common orientation (focal mechanism A: strike $80°$, dip $45°$, rake $-90°$), (2) 20% are generated with focal mechanism A superposed to a negative tensile component (50% of the energy release, the principal axis oriented vertically), (3) 20% are dominated by a second, different pure DC focal mechanism associated to normal faulting of different orientation (focal mechanism B: strike $130°$, dip $45°$, rake $-90°$), (4) 20% have focal mechanism B superposed to a negative tensile component (50% of the energy release, the principal axis oriented vertically), (5) the remaining 20% is composed by dominant shear crack events of random faulting style. For each event, full moment tensor components are derived, normalized to a scalar moment of 1 Nm. Each moment tensor component is then randomly perturbed up to ± 0.1 Nm (off-trace components) or up to ± 0.2 Nm (trace components). In this way a full moment tensor catalogue is generated. A second, pure DC catalogue is obtained from the previous one, only considering the DC term, after a moment tensor decomposition (ISO+CLVD+DC, see Jost & Herrmann [1989]; Krieger & Heimann [2012]).

We start considering the DC catalogue and apply the clustering using the Kagan angle metrics (Eq. 4.1). Results are shown in Figure 4.3a, through similarity matrices, sorted chronologically (left) and upon clustering (right). The plot illustrates the correct resolution of 2 clusters, accounting each for 40% of the catalogue, and a noise cluster, accounting for the remaining 20% of the earthquake source models. The two main clusters are composed by events of type (1) and (2), and (3) and (4), respectively, because the non-DC terms cannot be resolved in this approach. The analysis of the full MT catalogue (Figure 4.3b-c), is performed both using a cosine distance in $\mathbb{R}^9$ (Figure 4.3b), according to Eq. 4.2, and using a weighted distance (Figure 4.3c), according to Eq. 4.4. Both approaches lead to the correct resolution of the 4 original clusters; the 20% of random DC mechanisms of group (5) are properly identified as noise. As expected, the two clusters of combined

DC+tensile crack events show some similarity to their relative pure DC clusters. For the chosen synthetic tests setup, weighted and unweighted moment tensor clustering estimate comparable similarity values (average distance of 0.15 among different pure DC clusters, 0.06 among different non DC clusters, and 0.08 among a DC cluster and its corresponding non-DC cluster, with similar orientation of the DC component). On these synthetic dataset, the DBSCAN algorithm can successfully distinguish the original clusters for all discussed metrics. For both synthetic tests, the DBSCAN algorithm was tuned using N_{min} = 10 and ϵ = 0.90.

4.6 Clustering of Mining Induced Seismicity

To illustrate possible applications of moment tensor clustering, we consider a mining induced microseismic dataset. Although the method has similar potential applications for the analysis of natural seismicity, the induced seismicity dataset is here chosen because of the strong temporal and spatial variation of seismicity, the occurrence of different, repeatable focal mechanisms, the possible presence of non-DC, tensile and isotropic sources, and the occurrence of specific failures in correspondence to geoengineering operations. This makes it an optimal case to discuss the overall identification and characterization of source clusters, as well as the adoption of the focal mechanism clustering technique for monitoring purposes. The study region is located close to the town of Hamm, in the Ruhr region, Germany. In the Ruhr region, coal mining has been performed for centuries, and mining induced seismicity seismically monitored since 1983 [Bischoff et al., 2010b]. We focus here on induced seismicity taking place between June 2006 and July 2007, in consequence of the longwall mining of a rectangular-shaped panel in the region Hamm-Heringen. During almost 14 months, more than 7000 events were located, 3000 of them with magnitude above M_L -0.5. Moment tensor solutions are available for 1169 events, following the work of Şen et al. [2013], based on the inversion of full waveform amplitude spectra and displacement traces at surface stations located at local distances (below 2 km). The multi-step inversion approach adopted by Şen et al. [2013] made available two moment tensor catalogues: one for pure DC and one with full MT solutions. Note that these catalogues are the result of two different amplitude spectra inversion setups; the DC catalogue is composed by the best fitting focal mechanism solutions, assuming a pure DC constraint, and it is not simply listing the DC components of the full

MT solutions. Hypocenters are spread around the average depth of 1000 m, with ruptures mostly taking place just above the mining level. According to a first, qualitative classification of focal mechanisms, almost all events are characterized by normal faulting, with a fault plane steeper than 45° and one shallower than 45°. Strike angles have a more complex distribution, but a correlation with the orientations of sides and stopes of the rectangular mined region have been suggested [Şen et al., 2013]. Moment tensor solutions often indicate relevant non-DC components, which are interpreted as a combination of tensile crack (opening cracks occurring more often than closing cracks) and shear faulting.

We first consider the pure DC catalogue and used the Kagan angle approach to perform the source clustering. Upon checking different values for N_{min} and ϵ, DBSCAN is finally performed using N_{min}=10 and ϵ=0.90 (the effect of a variation of these parameters is commented in the discussion section). Results are illustrated in Figure 4 and show that five main clusters are identified. Their average focal mechanisms are shown in Figure 4c. Note that the adopted representation, showing only strike, dip and rake angles for one (steeper) fault plane, is only possible because of the favourable circumstance that many (more than 92%) events have a steeper (more than 45°) and a shallower (less than 45°) dipping, which make the mechanism unambiguously describe by fault plane angles of one plane. Clusters are here sorted upon their size. Cluster 2 (303 events) and 5 (16 events) are relatively similar among them and their normal faulting focal mechanisms striking in direction NE-SW and N-S, with one plane commonly striking parallel to the panel wall (about N 60° E); the smaller Cluster 5 has a larger oblique component. Cluster 1 (360 events), 3 (119 events) and 4 (78 events) also have similar features, striking sub-parallel to the panel sides, which are oriented WSW-ENE; the steeper plane of clusters 1 and 4 dip toward SW, and toward NE for cluster 3. Finally, 301 events are considered as noise.

A second application to the full MT catalogue was performed using a weighted cosine distance, according to Eq. 4.4. Weights for the 6 moment tensor components were chosen as it follows, based on the estimated perturbation misfits (see figure 4.2): w_{xx}=0.41, w_{yy}=0.41, w_{zz}=0.71, w_{xy}=0.65, w_{xz}=1.00, w_{yz}=1.00. DBSCAN run with analogous parametrization as for the DC clustering. Results are illustrated in Figure 4.5. Six clusters are found. Cluster 1 and 2 are the largest, with 357 and 141 events respectively; Clusters 3 and 4 are similar to Cluster 2, while Clusters 5 and 6 are similar to Cluster 1. 538 focal mechanisms are not assigned

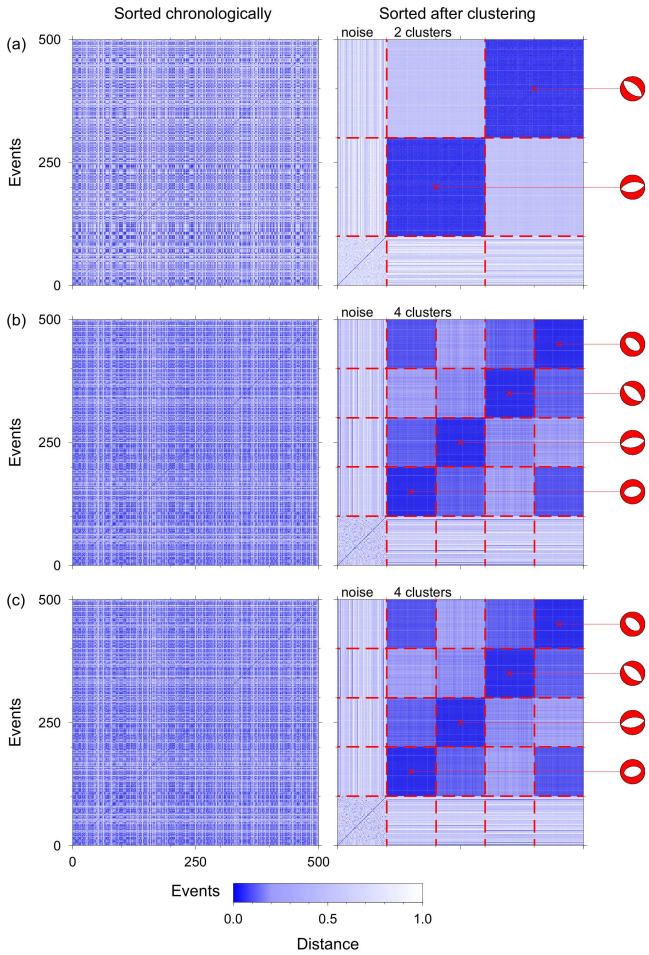

Figure 4.3: Synthetic test results for pure DC (a), and full MT (b, c) clustering are shown in terms of similarity matrices, according to the colour scale below. A Kagan angle distance is used for the DC approach, and both unweighted cosine distance according to eq. (4.2) (b) and weighted cosine distance as in eq. (4.4) (c) for the MT approach. Similarity matrices are plotted before clustering, sorting events chronologically (left-hand panels), and after clustering, sorting them upon their cluster (right-hand panels). Average focal mechanisms are shown on the right-hand side for each cluster, except for noise.

to any cluster and considered as noise. Figure 5c shows the source type diagram representation [Hudson et al., 1989]. It illustrates how the two main identified clusters are characterized by full moment tensor composed by a superposition of DC and tensile components. However, Cluster 1 is characterized by a positive tensile crack component, while Cluster 2 by a negative one. Both clusters include

events with variable orientation of the DC component. Only smallests clusters (e.g. Clusters 5 and 6), which are more compact, contains events with similar decomposition and similar DC mechanism. It is important to point out that MT clustering does not necessarily highlights the different moment tensor decomposition. This result is found here because of the unpopulated region at the centre of the Hudson plot, which separates regions (clusters) with denser populations of moment tensors.

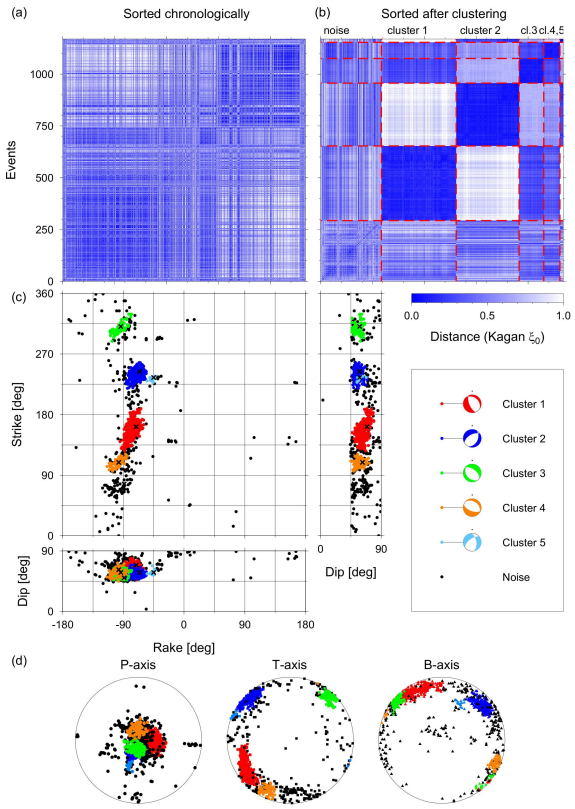

Figure 4.4: Results of DC clustering of a coal mining induced data set, Ruhr, Germany. Similarity matrices are shown before (a) and after (b) clustering. Red dashed lines indicate noise events and identified clusters. Strike, dip and rake parameters are plotted (c) along strike-dip, rake-dip and strike-rake diagrams, according to the colour legend on the bottom right. Mean focal mechanisms are plotted with the same colour scale. Plots (d) illustrate the distributions of pressure (P), tension (T) and null (B) axis for different clusters (Lambert azimuthal equal-area projection is used).

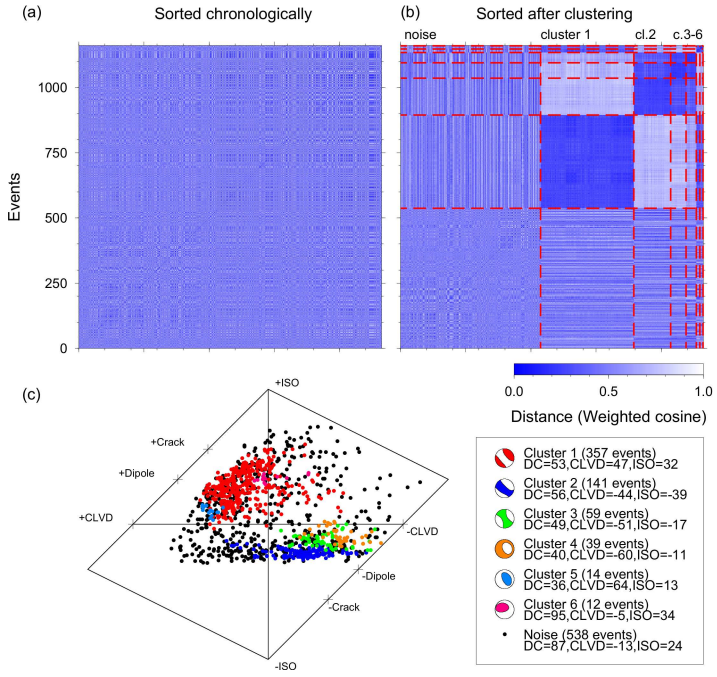

Figure 4.5: Results of MT clustering of a coal mining induced data set, Ruhr, Germany. Similarity matrices are shown before (a) and after (b) clustering. Red dashed lines indicate noise events and identified clusters. Source models are plotted using a source-type diagram (c), according to the colour legend. Mean values for the MT decomposition and mean focal mechanisms are given for each cluster, except for the noise one.

4.7 Temporal Monitoring of Rupture Process

The previous section illustrated the identification of clusters and their characterization, through the evaluation of average focal mechanisms for each cluster. Induced seismicity dataset, such as the mining dataset here considered, may be characterized by a strong spatio temporal variation, as a consequence of discontinuous geo mechanical activities and their translation in space at different time and phases of the exploitation. The spatio temporal migration of seismicity, which is well observed for the studied dataset, is not relevant here. However, this can well be accompanied by changes in the brittle failures. A temporal analysis of the number and characteristics of focal mechanism clusters is thus important for monitoring

purposes, in order to early detect anomalous rupture mechanisms. Limiting to mining environments, the appearance of new DC mechanisms may indicate the activation of pre-existing faults, and strong non-DC terms may indicate anomalous tensile components. Since the magnitude frequency distribution of DC and tensile events typically differs [e.g. Becker et al., 2010], the clustering technique can thus provide a valuable contribution towards temporal evolution of hazard assessment in the mine. The temporal evolution of different clusters, in terms of number of events, is illustrated in Figure 6. Induced seismicity mostly takes place between day 30 (reference day 0 is July 14th, 2006) and day 270. While at the beginning of the exploitation clusters 1, 3 and 4 are dominant, in the second phase, after day 150, most seismic events pertain to cluster 2. Cluster 5 is only activated at a later stage, between days 200 and 260.

We discuss here a possible approach of source clustering for monitoring purposes, with respect to the analysis of the DC catalogue for the Hamm region, simulating the temporal evolution of the catalogue. Since the moment tensor inversion is performed within 3 minutes and clustering of a catalogue of about 1000 events within 1 minute on a single processor, the clustering application can work in near-real time. In terms of the warning time required to detect the appearance of a new cluster, these computation times may be negligible for many applications. More often, the warning time will be controlled by the seismicity rate and the Nmin parameter. In fact, a new cluster will only be detected when a sufficient number of event with a new focal mechanism type have been identified. Before this time, they are identified as noise, and might only be detected looking at the noise rate; this option is not investigated in this work. The monitoring starts here after a learning period of 30 days, which is needed to have a sufficient number of earthquakes focal mechanism solutions. The clustering analysis is routinely repetead (in the example in Figure 4.7, every 10 days) considering either the whole seismic catalogue until the current date, which we refer as cumulative seismicity approach, or only the events of a previous period (here 30 days), which we refer as time window approach. The number and characteristics of the clusters are iteratively updated. A change in the cluster mean values or the appearance/disappereance of a new cluster can be used as a warning signal and trigger more detailed source analysis and an update of the hazard assessment. The cumulative seismicity approach (Figure 4.7d, green line) is suited to monitor the overall seismicity: the number of events increases with time while the clustering approach becomes more stable. The time window approach (Figure 4.3d, red line) may be less stable during periods of weaker activity, but it can also detect the disappearence or weakening of

previously active clusters. Results are illustrated in figure 4.7, where a snapshot (at day 270) of the monitoring framework is shown. The different panels on the top of the figure illustrates the spatiotemporal distribution of the hypocenters, their spatial correlation with the mined region, and the spatial distribution of different clusters. These plot are produced using the overall catalogue until the current monitoring day (day 270).

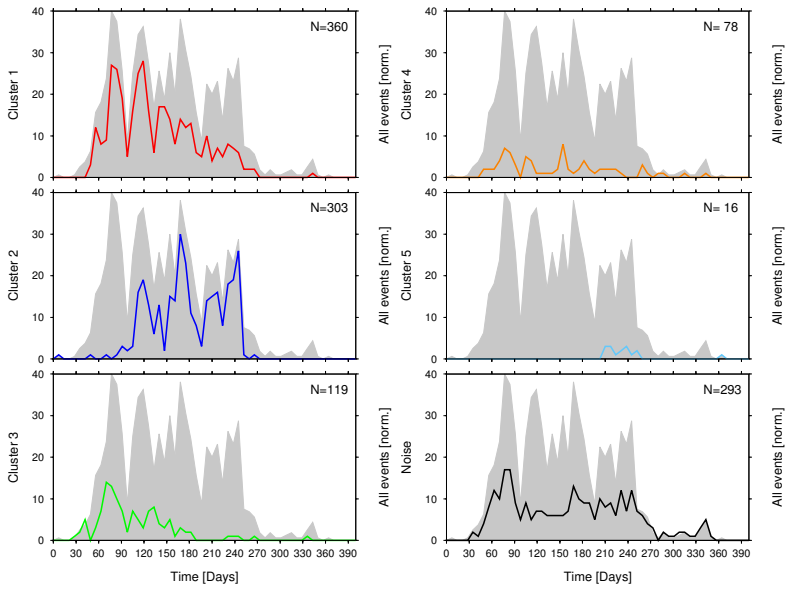

Figure 4.6: Temporal variation of the number of events from each cluster (colour curves according to the colour convention adopted in Fig. 4.4) and unclustered events (noise, black curve), with respect of the number of events with an available focal mechanism solution. Plots are shown for 400 d, starting on 2006 July 14, including the whole data set.

4.8 Discussion

Moment tensor clustering showed to be a powerful tool for the automatic classification of catalogues of earthquake source parameters, the identification and characterization of source models families in different environments and regions, and the evaluation of temporal changes of the source models. The application

to an induced seismicity catalogue at Hamm (Ruhr region, Germany) is suited to demonstrate the technique performance, as seismicity results strongly correlated to human activities, not only with respect to the spatial migration of epicenters with the mining advancement, but also for the characterization of the rupture processes, which is strongly linked to the mine geometry. The clustering technique, both applied to DC and full MT models is able to recognise the most important rupture patterns. The DC clustering approach identified the typical geometry of DC focal mechanisms, which resulted characterized by normal faulting mechanisms oriented parallel to the mining stope and panel sides. The MT clustering was unable to resolve the orientation of the DC terms, but could well detect the presence and sign of the non-DC component, which are in the current case associated to tensile components; this result is important towards the mining monitoring and hazard assessment. The choice of a specific metric (e.g. only considering full MT or DC component) will affect clustering results. Any future study should choose the most proper metric to answer the target scientific questions. For example, an analysis of fault plane orientations may be best discuss with the aid of a pure DC clustering approach, whereas the distribution of non-DC terms (e.g. in volcanic or mining environments) can only be judged using a full MT approach.

The method has a range of possible application for the analysis of broad seismicity catalogues in tectonic, volcanic or induced seismicity environments. Among its possible applications, we can foresee the investigation of repeated rupture processes in large datasets and microseismicity applications, the reconstruction of fault system geometries, the assessment of non-DC terms, and the identification of transient earthquake source and rupture anomalies. Depending on the goal of the source clustering, a preferred metric can be chosen. We have here proposed a variety of metrics, though other could be considered to answer specific seismological questions. For example, distances based only on the orientation of one fault plane angle, may be suited for the discussion of the orientation of specific faults or slab segments. Another important example may be given by distances definition on the base of the similarity of pressure and/or tension axis, which may be provide useful informations towards stress inversion studies.

Towards the adoption of the proposed technique for future studies, either dealing with natural or induced seismicity datasets, it is extremely important to remind that clustering results may be affected by the subjective choice of the clustering parameters. Limiting to the DBSCAN algorithm discussed in this work, a vari-

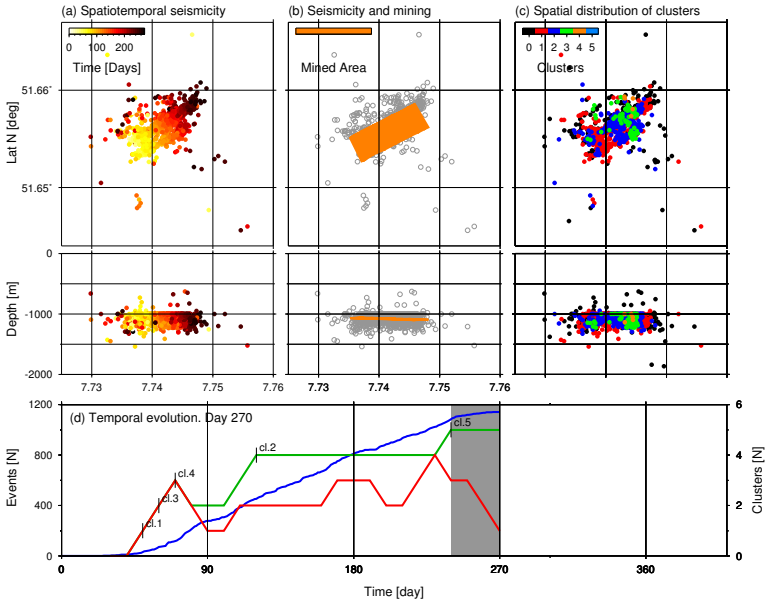

Figure 4.7: Snapshot (day 270 since 2006 July 14) of the seismicity monitoring framework, simulating the continuous monitoring applied to the Ruhr DC catalogue. Top plots illustrates the spatiotemporal evolution of seismicity as map and cross-section projection (top left, according to the given colour scale), the comparison of seismicity location and mined region (top centre, the mined region is denoted with an orange polygon), and the spatial distribution of different clusters (cluster colour scale according to convention used in Figures 4.4 and 4.6). The bottom panel illustrate the evolution of the number of detected clusters (thick red and green lines) and the cumulative number of event (thick blue line), as a function of time. The clustering is repeated every 10 d, after a first learning period of 30 d. The red curve is obtained considering only the seismicity recorded in the preceding 30 d (grey area), the green curve using all events until the running day. Thin black lines and cluster labels denote the appearance of clusters for the cumulative seismicity approach (green line).

able choice of Nmin and parameters can strongly modify the number, size and average properties of the clusters. Figure 8 attempts to summarize main effects of different parameter choices. In general, decreasing the parameter leads to the identification of more self similar clusters and will tend to produce a larger number of small clusters. The number of cluster generally increases by reducing Nmin. The choice of clustering parameter should also account for the expected number of unclustered events. Increasing the size of the noise cluster is equivalent to a loss of information from the original catalogue, as the clustering result only can be used to assess the rupture process of a part of the studied seismicity. The number of unclustered events is typically correlated with the clustering parame-

ters and can be reduced by increasing or by decreasing Nmin. Few anomalies can anyway be observed in Figure 8, with the presence of darker belt-like regions of increased cluster numbers (Figure 8a) and local scattering of the number of noise events (Figure 4.8b). These effects are illustrated in Figure 8c: we repeated the clustering using a fixed ϵ (0.90) and 4 values of N_{min} (10, 15, 20, 25). In general, as expected, increasing N_{min} leads to smaller clusters, as only denser regions of the cluster are left. However, in the specific case one cluster (the red one) has an heterogeneous density with two denser regions, separated by a more sparse band. In such case, when increasing Nmin from 15 to 20 the original red cluster is divided into two subclusters (red and cyan in the plot corresponding to N_{min} 20), temporally increasing from 4 to 5 the number of detected clusters. A further increment of Nmin, e.g. to 25, results in the typical decrease in the clusters number, with the disappearence of the less populated clusters. The combination of such effects and the variable required cluster density are similarly responsible for some sudden variations among the number of noise events of neighbouring ϵ - N_{min} configurations.

A major potential of the clustering technique concerns its adoption within monitoring tools. The iterative clustering at different time can be used to detect the appearance, disappearance and evolution of clusters. In fact, if strong anomalous failure processes may be identified by the clustering approach, through the identification of a new cluster with anomalous average properties, it can also happen that the temporal stress perturbation only changes the average rupture mechanisms. For example, rupture may always take place along the same fault geometry (e.g. with strike and dip unchanged), and the effects of the temporal evolution of local stresses may only lead to a variation of the slip direction, along a more favourable configuration. Such effect may be seen through the appearance of a new cluster, if the rake change is considerable, but can also be detected for less dramatic changes by checking the time evolution of the average properties of the cluster. Cluster appearance (and disappearance) may also occur as a consequence of the clustering approach. A common case may be when one cluster becomes at a given time density-reachable from the second one, leading to a single, broader cluster. This can occur if the two clusters are close (similar) enough, when a sufficient number of outliers are present between them. A timely detection of anomalous ruptures is linked to the choice of clustering parameters. The occurrence of new fracturing processes can only be identified through the detection of a new cluster, which only takes place upon the inclusion of a sufficient number of event with the new source model in the catalogue. A quicker detection of new clusters can be achieved by

reducing the parameter Nmin. However, this choice can also lead to false alarm, depending on the catalogue quality and the number of expected outlier solutions.

Finally, the possibility of combining clustering techniques based on different source parameters, such as focal mechanisms, location, size, stress drop or seismicity rate, may be used to further investigate significant changes in the observed seismicity. However, such extension will need the definition of specific metrics, where different physical units have to be handled in a common distance definition.

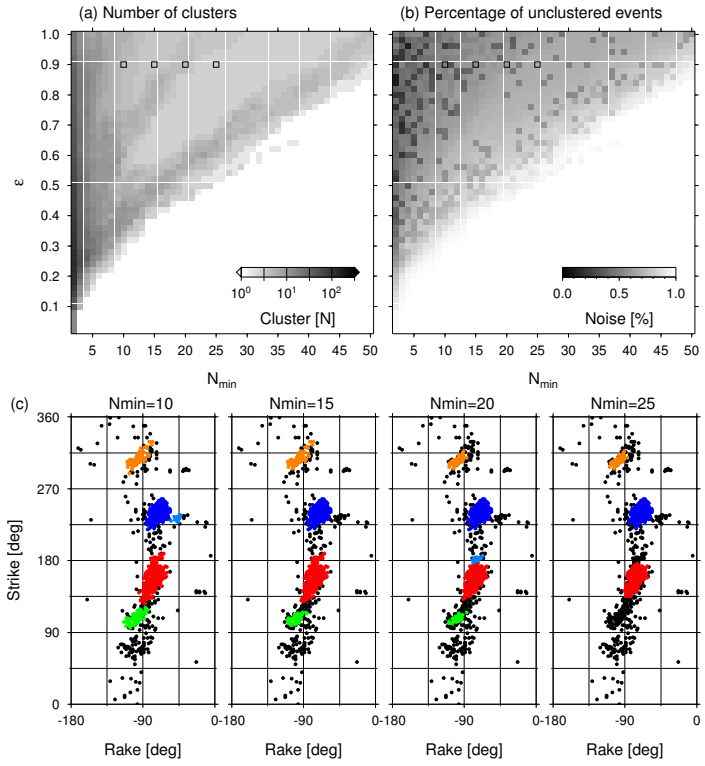

Figure 4.8: Performance of the DBSCAN algorithm with the pure DC catalogue from the Ruhr region (distance based on Kagan angle) when varying parameters Nmin and epsilon. These plots illustrate how these parameters can change the number (and thus the average size) of clusters (top left-hand panel) and the number of non-classified (noise) focal mechanisms (top right-hand panel). Clustering results (bottom panels) are illustrated for the pure DC Ruhr data set using the Kagan angle distance, with ϵ 0.90 and four N_{min} values (the four used configurations are denoted by squares in the top left-hand plot). The analysis of the pure DC Ruhr data set has been performed with N_{min} = 10 and ϵ = 0.90.

4.9 Conclusions

A methodological approach and algorithm for moment tensor clustering and automated classification of earthquake point source models have been here presented and illustrated through application to synthetic and real dataset. We could demonstrate the potential of the method for the automated detection and characterization of focal mechanisms clusters, which can be used to analyse large moment tensor catalogue. The availability of different metrics make possible to apply our method to different type of source representation.

We suggest the adoption of Kagan angle distance for pure DC catalogues, and weighted cosine distance for deviatoric and full moment tensor catalogues. Weights should be chosen on the base of moment tensor uncertainties, which are specific for different setups, and related to the adopted moment tensor inversion techniques, source-network geometries and velocity models. Other specific distance definition can be adopted, depending on the clustering application. On the other side, clustering parameters (N_{min} and ϵ) should be chosen carefully, and synthetic and real tests should be used to assess their effects on the clustering performance, which can be affected in terms of the number, size and self similarity of identified clusters. In particular the Nmin value should be chosen with respect of the dataset size (e.g. increasing with the size of the dataset) and the desired resolution among close clusters: these can only be discriminated if the inter-cluster regions are judged by the algorithm as sparsely populated. The ϵ parameter should be chosen according to the desired degree of similarity within each cluster (small ϵ will lead to homogeneous clusters composed of very similar focal mechanisms) and upon the adopted metrics.

The application to an induced seismicity catalogue, following the exploitation of a coal mine panel in the Ruhr region, Germany, lead to the identification of main seismic source families. Based on the DC catalogue, we identified 5 families of events, with normal faulting of different orientations. Striking correspond to the orientation of the panel sides and stope. Full moment tensor clustering identified two main event families, based on the presence of positive and negative tensile components. The analysis of the temporal distribution of clusters indicate that during the first part of the longwall mining, ruptures are dominated by NNW-SSE

strike faulting, parallel to the mining stope. During the second part of the exploitation, mostly from day 150, most induced earthquakes were instead characterized by a WSW-ENE striking, parallel to the panel sides.

The method is potentially of interest for monitoring of natural and induced seismicity, in active tectonic, volcanic, geothermal and mining environments. The adoption of the clustering tool for monitoring purposes can be used to identify the appearance or disappearance of rupture clusters, and significant variation of fracturing processes or local stress, thus providing important information for the temporal reassessment of seismic hazard.

4.10 Acknowledgements

The authors wish to thank Prof. Dr. Jan $\check{S}$ilen$\check{y}$ and an anonymous reviewer for comments and suggestions, and Prof. Dr. Frank Krger for valuable discussions. The used mining seismicity moment tensor catalogue [Şen et al., 2013] was generated thanks to the monitoring and processing work carried out by the Ruhr University Bochum, for which we particularly acknowledge Prof. Dr. Thomas Meier and Ms. Monika Bischoff. Figures and DC focal mechanisms have been plotted with GMT (Wessel and Smith 1998). Moment tensor decomposition and plotting is carried out using the Mopad tool [Krieger & Heimann, 2012], which is routinely used by the software MTD. This work has been funded by the German BMBF Geotechnologien project MINE (Grant of project BMBF03G0737).

Chapter 5

Systematic Changes Of Earthquake Rupture With Depth: A Case Study From The 2010 Mw 8.8 Maule, Chile, Earthquake Aftershocks sequence

Authors:
Ali Tolga Sen[1], Sebastian Heimann[2], Simone Cesca[1,2], Dietrich Lange[3] Torsten Dahm[1,2]
Journal:
Geophysical Journal International
Status: Submitted (25 April 2014)

Authors affiliation:
1) Institute of Earth and Environmental Sciences,
University of Potsdam, Potsdam, Germany
2) GFZ (German Research Centre for Geosciences) Potsdam,
Section 2.1, Physics of earthquakes and volcanoes,
Potsdam, Germany
3) GEOMAR, Helmholtz-Zentrum für Ozeanforschung Kiel
Kiel, Germany

5.1 Abstract

On February 27, 2010, the M_W=8.8 Maule earthquake struck offshore Chile, initiating a long sequence of aftershocks, which lasted for months. In this work, we invert for focal mechanisms, depth and source durations of 72 aftershocks of the Maule earthquake, with magnitudes between M_W 4.0 and 6.8. In order to account for the different number of available seismic records during the aftershock series we use stations at regional and teleseismic distance to invert for different temporal intervals of the aftershock sequence. During the first days after the Maule 2010 mainshock, only few broadband stations at regional distances were available, and we mostly rely then on teleseismic recordings. Later, a dense network of 130 broadband stations was installed on-shore allowing source investigations on the base of seismic data at regional distances. Focal mechanisms highlight the correlation of thrust focal mechanisms with the 3D slab model geometry in the area, and the occurrence of normal fault earthquakes on a crustal fault system, in the northernmost part of the study area. The analysis of depth and magnitude dependence of the normalized source duration, following an approach proposed for strong and global earthquakes in subduction zones, indicate that the correlation among these source parameters is confirmed and extends also to smaller magnitude events.

5.2 Introduction

Convergent plate boundaries, where oceanic plates subduct in the mantle along shallow dipping megathrust faults, are the regions where the earth's largest earthquakes occur. The majority of such events show thrust faulting characteristics on the interplate megathrust and the depth of the seismicity is mostly distributed down to 50 km [Bilek et al., 2004]. The 2010 Maule 2010, Chile earthquake is the sixth largest earthquake instrumentally recorded in the history [e.g. Agurto et al., 2012]. The Global Centroid Moment Tensor (gCMT) solution has a scalar moment for the mainshock of M_0 = 1.8x10^{22} Nm (M_W=8.8) and the centroid location is given with $35.95°$S, 73.15W, 23 km depth. The focal mechanism (strike $12°$, dip $18°$, and rake $112°$) corresponds to a NNW-SSE striking thrust fault, with low-angle dipping plane consistent with the slab orientation. Coseismic slip inversions show a bilateral rupture propagation and a rupture length of $\sim$550 km along

the Chilean Forarc. Two major slip patches were resolved [Moreno et al., 2012] and the peak slip was 15-20 m. Hicks et al. [2012] suggested that a subducted topographic anomaly on the incoming plate, now located at the subduction interface between the Nazca and South American plates, controlled the nucleation of the Maule 2010 event. Four main tectonic features shape the seismic characteristics of the upper plate along the Maule region, which are the north-south trending Thrust Rigde (between $35°$S - $37°$) [Geersen et al., 2011], the Santa Maria fault (between $\sim 36°$S - $37°$S) [Melnick et al., 2012], the Lanalhue fault [Glodny et al., 2008], which is a major NW-SE trending crustal fault system (between $\sim 38°$ - $39°$S), and the extensional Pichulemu aftershock cluster [e.g Farías et al., 2010] at the northern part of the Maule 2010 rupture zone.

In response to the M_W 8.8 Maule earthquake on 27 February 2010 and given the lack of dense regional network, Chilean and international partners (IRIS, SSN, IPGP, GFZ, University of Liverpool) installed a dense seismological network (International Maule Aftershock Deployment, IMAD), which covered the whole length of the rupture zone between $32.5°$S and $38.5°$S. Figure 5.1 shows the changing number of stations in time. This dense network spreads around an area of about 600 x 300 km, larger than the rupture area of the main shock (Figure 5.2). More than 160 seismic stations were deployed, 130 of them equipped with broadband sensors, whereas the remaining ones are short period stations. Over 2.300.000 potential P and S wave onsets within a time frame of 2 months were detected, starting from March 15, two weeks after the occurrence of the main shock. Hypocentre locations of 18629 aftershocks show that aftershock seismicity mostly occurs between 40 and 140 km distance from the trench, and in a depth range between 10 and 70 km [Rietbrock et al., 2012]. The IMAD network was completely operational mid of March 2010. Prior to this date, the location information is based on the Chilean catalogue provided by the Servicio Sismologico Nacional de Chile (SSN) and the National Earthquake Information Center (NEIC), which has a magnitude of completeness of ~ 4.

In the time frame from the M_W 8.8 Maule earthquake to now, aftershock catalogues have been used for several seismological studies. Rietbrock et al. [2012] built a catalogue of over 30000 events, from the first 2 months of the IMAD records, by using an automated picking and processing methods. Lange et al. [2012] located over 20000 aftershocks in the Maule region. Out of these, for 13441 events P phases from at least 12 stations are available. The highest lo-

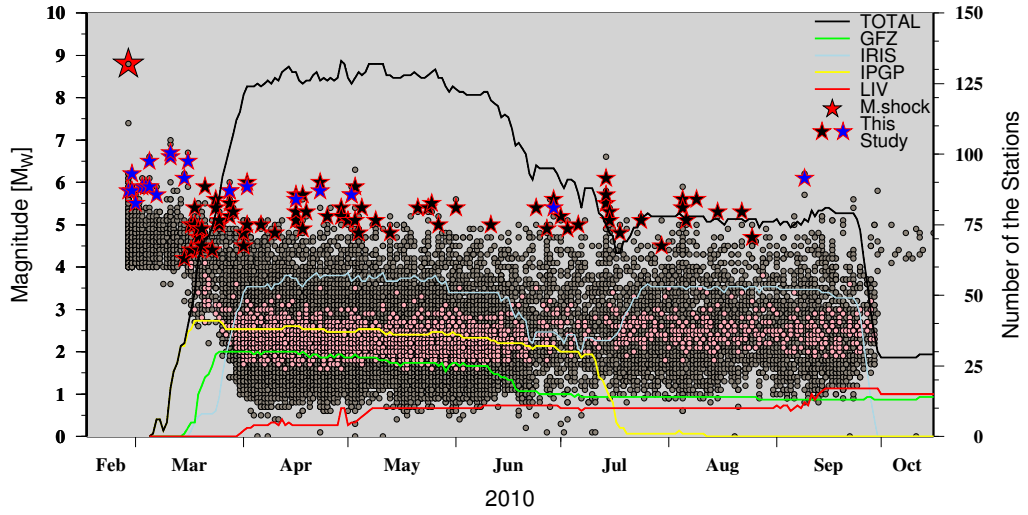

Figure 5.1: Temporal evolution of the aftershock sequence and IMAD regional network. Continuous lines represent the number of available stations installed by different Institutions (see color scale) between March and October 2010. Grey dots represent 13441 detected and located events, using at least 12 P phases from the local aftershock network [Lange et al., 2012]. Pink dots indicate 2494 events, with the highest location quality. The red, blue and black stars denote the mainshock, aftershocks inverted with teleseismic data and aftershocks inverted with local network, respectively.

cation quality subcatalogue includes only 2494 aftershocks [Lange et al., 2012, Figure 5.2]. Agurto et al. [2012] relocated 145 events until March 2012 from the GCMT catalogue and then applied a full waveform regional moment tensor inversion (RMT) using the software package ISOLA [Sokos & Zahradnik, 2008], finally obtaining focal mechanisms for 125 aftershocks taking place between March 18 and December 1, 2010. A similar study was carried out by Hayes et al. [2013], where 2375 events were relocated and moment tensors inversion performed for 465, using regional waveforms and following the approach of Herrmann et al. [2011].

In this study, we first derive moment tensor mechanisms for a set of strong aftershocks of the Maule 2010 earthquake. We selected a subset of 72 events from the local catalogue of Lange et al. [2012] with magnitudes M_W larger than 4, more then 12 P phases per event, RMS smaller than 0.6 s and hypocenter uncertainties smaller then 5 km. Focal mechanisms for the earlier largest aftershocks (limited

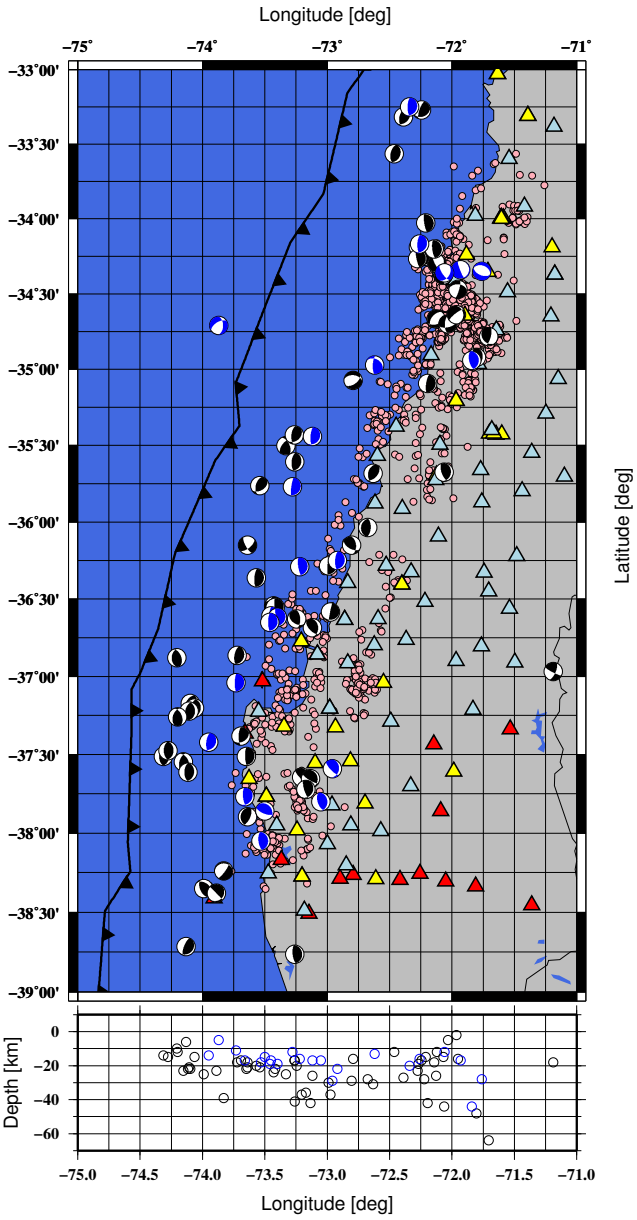

Figure 5.2: Map showing the distribution of events used in this study (black focal mechanisms from regional inversion, blue focal mechanisms from teleseismic inversion). Triangles of different colors denote IMAD broadband stations from different institutions (colors are according to the scale in Figure 5.1). Pink dots indicate 2494 high quality locations from the local aftershock network [Lange et al., 2012].

to the magnitude range M_W 5.4-6.7) are obtained by the inversion of regional and teleseismic data, whereas smaller events in the magnitude range M_W 4.2-5.6 following the deployment of the IMAD have been studied using regional data only. We compare our solutions with available reference focal mechanisms and the slab geometry, and then further extend the inversion approach to obtain stable estimations of the source duration.

Global studies of source durations of larger events from different subduction zones showed a depth dependence of a moment normalized source duration, with anomalous long duration at shallow depths below 15 km [Bilek & Lay, 2002; Bilek et al., 2004]. In this study, we focus on source time durations of moderate to small magnitude aftershocks of the Maule 2010 event, to evaluate down-dip variations of source time durations and their relation to the structure of the Forearc and the plate interface. We extend the approach of Bilek et al. [2004] considering seismicity down to magnitude M_W 4 in a single slab region.

5.3 Methodology

Source inversion are performed using the Kiwi tools software [Cesca et al., 2010; Heimann, 2011]. The Kiwi tools were previously successfully used to investigate a broad range of earthquake sources, including crustal and deep earthquakes, natural and induced seismicity cases, and both at local, regional and teleseismic distances [e.g. Buforn et al., 2011; Cesca et al., 2010; Şen et al., 2013; Zhao et al., 2014]

Two different inversion procedures are adopted here, in consequence of the very different observation conditions throughout the occurrence of the considered aftershock sequence. The local inversion of aftershocks can only be performed for the aftershock sequence after March 17, when the aftershock network is fully operational. (Figure 5.1). Larger events are studied for the whole sequence using teleseismic data and sparse regional data.

For the regional inversion, targeting earthquakes with magnitudes M_W between 4.2 and 5.6 in the period from March 17th, 2010 to August 25th, 2010, we adopt an automated multi-step inversion scheme, which combines both amplitude spectra

and full waveform time domain inversions in different steps. Synthetic seismograms and spectra are built using a layered 1D velocity model, using a reflectivity code [Wang, 1999]. The layered velocity model is an averaged 1D velocity model upon Haberland et al. [2009]. The inversion procedure initially relies on source locations from the local catalogue [Lange et al., 2012]. The first inversion step is performed in the frequency domain, by fitting full waveform amplitude spectra between 0.03 and 0.1 Hz, to derive a pure double couple (DC) point source model, scalar moment and centroid depth. The advantage of the amplitude spectra inversion relies in its stability and lower dependence on a precise trace alignment and phase shifting, which results in a more stable inversion of the double-couple component of the moment tensor on the costs of loosing the phase information. Additionally, a full moment tensor inversion was performed [for details, see Cesca et al., 2013b]. Since the events show in general small non-DC components, we restrict the discussion to DC point source models and do not report the non-DC components.

In the second step, a full waveform time domain inversion is performed to resolve the ambiguity in focal mechanism polarity of amplitude spectra inversions. Finally, we invert the rupture duration, under a spatial point source representation. A set of apparent durations, one for each seismic station, is obtained by fixing the focal mechanism, depth and moment, as retrieved from the previous inversion steps, and by inverting the point source rupture duration. At each station, the high-frequency (up to 1.0 Hz) amplitude spectra are fitted. This approach and its application to estimate directivity effects are described in Cesca et al. [2011]. Here, we retrieve average rupture durations from all the stations which recorded the single events. An example of inversion result, including point source parameters, rupture duration and waveforms and spectra fit is illustrated in Figure 5.3. The performance of the rupture duration inversion result can be discussed with the aid of Figure 5.4, which illustrate both the misfit curves for different single stations as well as for the whole dataset, when varying the rupture duration parameter only. For most stations, the misfit curves show a clear minimum at the corresponding apparent durations. The difference among synthetic spectra and waveforms when varying the rupture duration are illustrated for a given station in Figure 5.4 (right) and highlight the significant improvement in matching the observed waveform and spectra, when an optimal rupture duration is chosen.

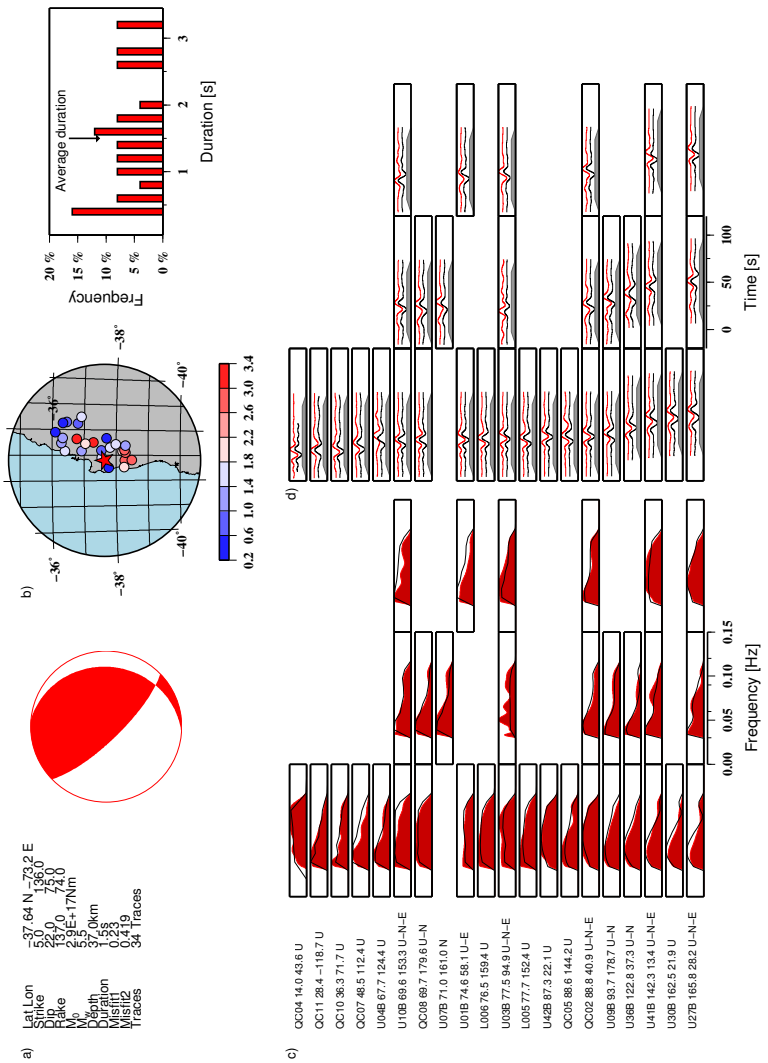

Figure 5.3: Source parameters, spectra and waveform fit after regional moment tensor inversion (for the April 23, 2010, at 10:03, M_W = 5.5 earthquake). a) Summary of DC source parameters derived by the regional inversion. b) Epicentral location (star) and apparent durations at different stations (circles, the color scale denotes apparent durations); the right plot illustrates the distribution (histograms) of the apparent source durations, used to derive the average duration. c) Comparison of normalized amplitude spectra between observed (red) and synthetic (black) data; the station information (distance, azimuth and components) are given on the left side. d) Comparison of full waveforms in the time domain, showing observed (red) and synthetic (black) normalized full waveforms (gray areas denote the applied taper).

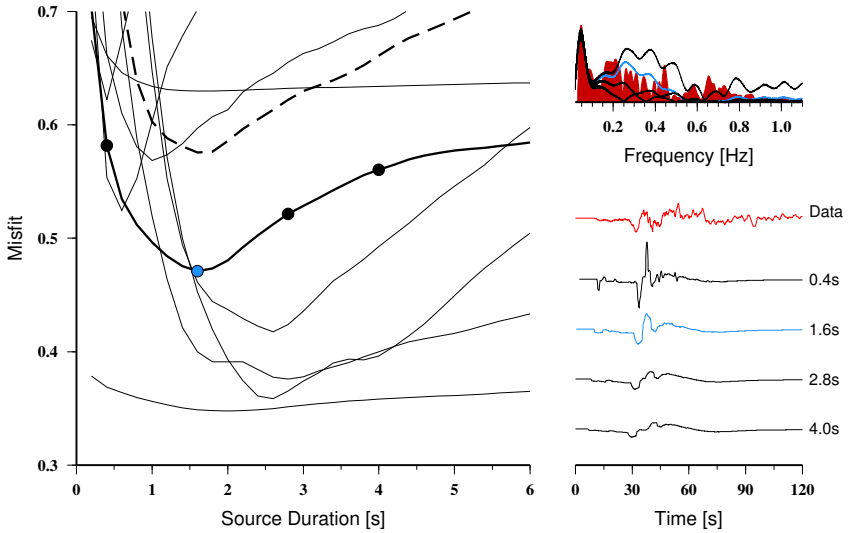

Figure 5.4: Left: misfit curves are shown for different stations, when varying the source duration: a thick black line denote the misfit curve for reference station U04B (IRIS) (for which spectra and waveforms are shown), thin black lines are the misfit curves for all other stations, and a thick dashed line denote the misfit curve when using all data. Circles indicate the misfits for the reference station for durations of 0.4, 1.6, 2.8 and 4.0 s. The best fit for the reference station (blue circle) and for the whole network is found for a rupture duration of 1.6 s.). Right: Comparison of amplitude spectra (top) and waveforms (bottom), showing observed data (red) and synthetics for different rupture duration (black lines for durations of 0.4, 2.8 and 4.0 s, and blue lines for the best rupture duration of 1.6 s).

The inversion for largest aftershocks (magnitudes M_W 5.4-6.8) in the period of February 27th, 2010 to October 23rd, 2010, was performed using regional and teleseismic data from seismic broadband stations of different networks; waveform data and stations metadata were accessed thanks to the IRIS facilities and converted to displacements. A station selection algorithm is used [Heimann, 2011], which selects 60 stations within 100^o maximal epicentral distance. A different inversion scheme is developed here. It is still based on the Kiwi tools and combining frequency and time domain inversion, but is especially tuned for the analysis of larger events and the fit of teleseismic records. The first inversion step is performed in the frequency domain and it is used to define a set of source model configurations, which are then used in the following time domain inversion. The time domain inversion is iteratively solved for each starting configuration by a gradient search. Both inversion steps optimize the fit of vertical P and transversal S phases. Data windows have a length of 60 s, and waveforms are bandpass filtered between

0.01 and 0.05 Hz. The inversion provides the following DC point source model parameters: strike, dip, rake, depth, moment, relative centroid-epicenter location and rise time, which defines the duration of the rupture process for a point source model. For the rise time inversion, a broader frequency range is used, including frequencies up to 0.25 Hz. Uncertainties on all parameters are estimated using a bootstrap approach using random subsets of available stations (see also Heimann, 2011). For example, the uncertainties on duration are the result of the exploration of a 3D solution space, where duration, scalar moment and depth are perturbed, while the remaining source parameters are fixed (Figure 5.5).

5.4 Focal mechanisms and source durations

We obtain 72 focal mechanisms and source durations, for earthquakes with magnitude varying between M_W 4.0 and 6.5. The regional inversions (56 solutions) setup is characterized by an asymmetric station distributions, with stations located on Chilean mainland, and epicenters located both offshore and inland (Figure 5.2). As a consequence, the azimuthal gaps for regional inversion using IMAD data vary between 58° and 302°. Six events could be analysed using both inversion approaches, leading to similar focal mechanisms solutions; since teleseismic inversions (22 solutions) relied on a more distributed network, with lower azimuthal gaps, only these solutions are further considered for six events for which both inversion setups were testd.

The centroids depths for the selected events vary between 5 and 65 km depth, with an average depth of 20 km. Most of the events (78%) have a thrust mechanism, whereas the remaining ones show normal or oblique normal focal mechanisms. Thrust mechanisms are spreaded along the rupture area of the Maule mainshock. Normal fault mechanisms cluster spatially in the continental crust of the overriding plate (source depths of less than 25 km) in the Pichilemu area, at about 34°-35° latitude South. The specific finding of normal fault mechanisms on top of the slab at the Pichilemu area was also described in Farías et al. [2010] and Agurto et al. [2012].

We evaluate the consistency of our focal mechanisms with published DC solu-

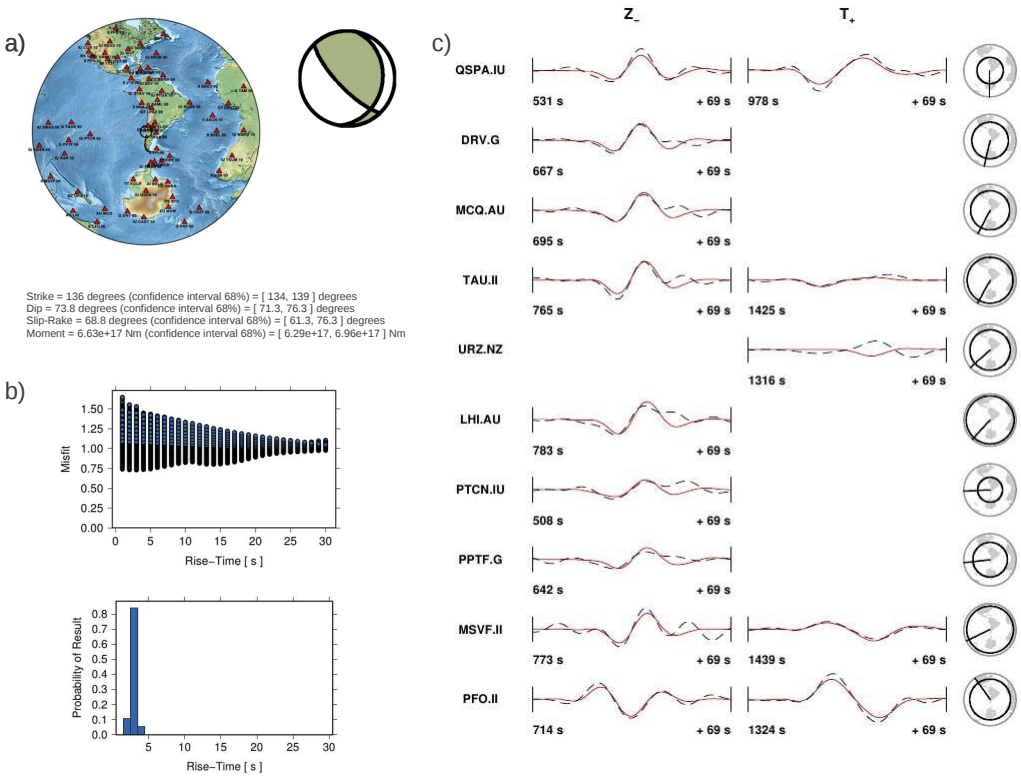

Figure 5.5: Source parameters and waveform fit after teleseismic moment tensor inversion (for the April 23, 2010 at 10:03:06, MW = 5.5 earthquake). (a) Focal mechanism and distribution of used broadband stations (triangles). (b) Comparison of misfits and rise time (top), for all tested point source models (the best fitting solution has a duration of 3 s), and distribution of results based on a bootstrap approach (bottom), used as an uncertainty measure. (c) Comparison of filtered body wave waveforms (dashed black lines are observed data, red lines are synthetics) for vertical P (left column) and transversal S (right column) waves for selected stations. The right panel shows epicentral distances and azimuths of shown stations).

tions in the region of the Maule 2010 earthquake [Agurto et al., 2012; Hayes et al., 2013, and gCMT catalogue]. For our dataset of 72 events, 43, 39 and 36 reference focal mechanism solutions are available in the catalogues by Agurto et al. [2012], Hayes et al. [2013] and gCMT [Ekström et al., 2012], respectively. The comparison between the catalogues is performed using the Kagan angle [Kagan, 1991, 1992] to quantify the similarity among pure DC focal mechanisms (Figure 5.6). Although for most events we find an acceptable agreement with reference solutions, e.g. with average Kagan angles of about 25^o and 20^o when comparing to Agurto et al. [2012]; Hayes et al. [2013] solutions, few focal mechanisms show

larger differences. A more comprehensive agreement is found, when comparing our solutions with the slab geometry (Figure 5.6d). Here the comparison is only performed for the 63 thrust mechanisms, and the Kagan angle is computed among the obtained focal mechanisms and a pure thrust mechanism along planes oriented according to the slab gradient at the epicentral location. The adopted 3D slab geometry is based on the model of Hayes et al. [2012].

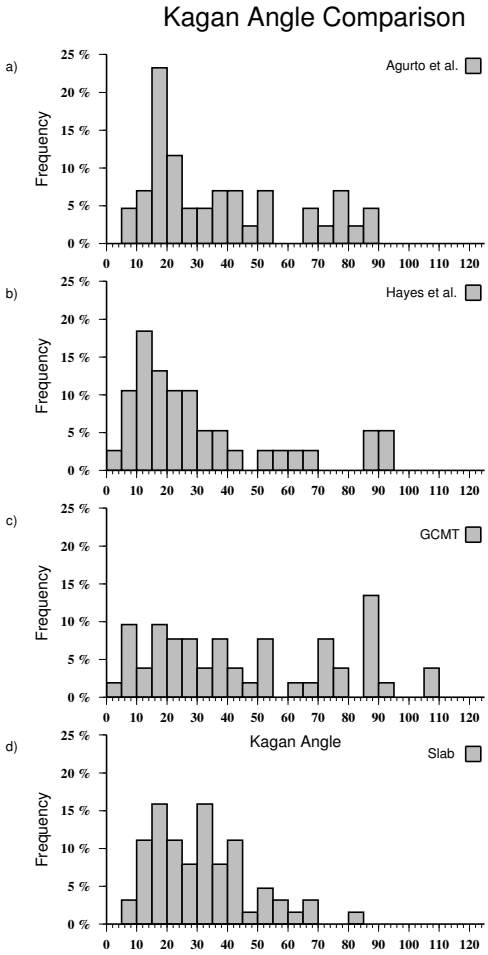

Figure 5.6: Comparison of DC inversion results with reference solutions and the slab geometry, using Kagan angle metrics. The comparison is performed against solutions by Agurto et al. [2012, plot a], Hayes et al. [2012, plot b], GCMT catalogue (plot c) and pure thrust mechanisms oriented according to the 3D slab model by Hayes et al. [2012, plot d].

Tsunamogenic earthquakes are characterized by long rupture duration, low excitation of higher frequencies and the tsunami disproportionally large for the given magnitude [Kanamori, 1972]. Tsunamogenic earthquakes have been documented in Japan (1896), Alaska (1946), Kuril Islands (1963, 1975), Nicaragua (1992), Peru (1960, 1996), Java (1994, 2006), and Indonesia (1907, 2010) [Lay et al., 2010]. Most explanations invoke earthquake rupture along the very shallow part of the subduction interface, conditional frictional regime at the plate interface and slow slip through uncosolidated sediments with unconsidilated deposits from accretionary prisms [e.g. Bilek et al., 2004; Collings et al., 2012; Lay et al., 2012]. If the conditions above are needed for tsunamogenic events, then the smaller magnitude earthquakes within the subduction segment should also have unusual long relative source durations, similar as their stronger neighbors which caused tsunamis. Bilek & Lay [2002] and Bilek et al. [2004] showed a linear relationship for circum-Pacific subduction zone earthquakes between scalar moment and normalized source duration (NSD), with increasing NSD for shallow earthquakes ($\leq$ 15 km depth). Using subsets from different subduction zones, Bilek et al. [2004] showed differences on the depth-dependence durations. Events along the forearcs of Alaska, Mexico and Peru show clear depth-dependence of NSD, while events in Java and Japan show little or none depth-dependence of the NSD. The longer NSD at shallow depths subduction was suggested to be a combination of a variety of features and processes, such as fluid flow, thermal structure, and sediment deformation mechanisms [Bilek et al., 2004] leading to a conditionally stable frictional regime at shallow depths.

However, previous studies mainly focused on large earthquakes (e.g. with scalar moment above 10^{17} Nm). In this study, we enhance the magnitude range for the evaluation of the correlation among source parameters, including weaker events down to M_W 4, focusing to the subduction segment sampled by the aftershock series of the Maule 2010 earthquake. To compare our findings with the larger events (M$\geq$4.0) from regional/global studies, we merged the results from Bilek et al. (2004) for Chile with the estimated parameters of our inversion. Figure 5.7 shows the comparisons between scalar moment, duration, NSD and depth.

In Figure 7a, we plot the comparison between scalar moment and duration and evaluate it in a logarithmic scale plot. These results suggests a linear relationship between these two parameters, in agreement to previous results by Bilek et al. [2004]. From the obtained absolute source duration, normalized source duration

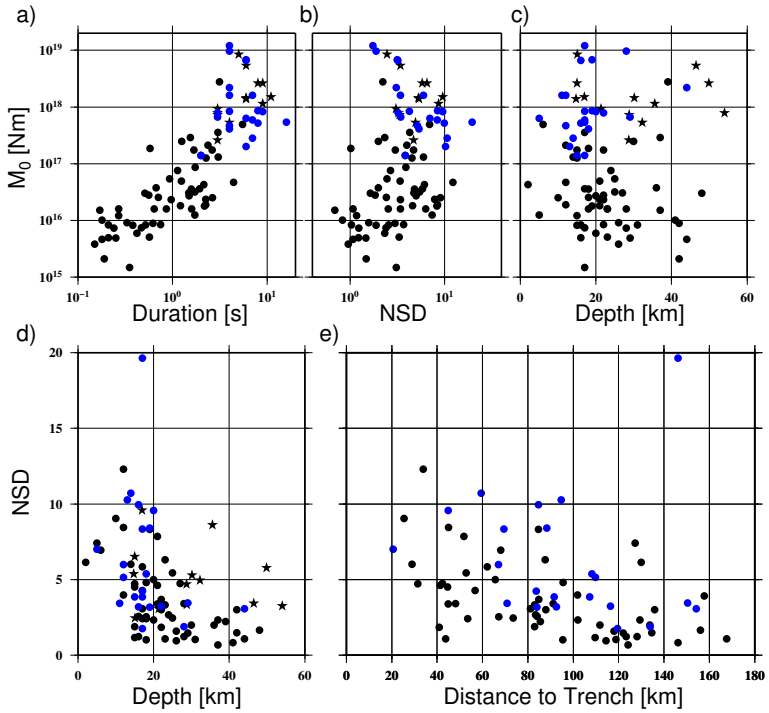

Figure 5.7: Comparison of duration and scalar moment (a), NSD and scalar moment (b), depth and scalar moment (c), depth and NSD (d) and distance to trench and NSD (e). Black and blue circles denote our solutions, using regional and teleseismic data respectively. Black stars are results for earthquakes in Chile by Bilek et al. [2004].

(NSD) for a reference magnitude ($M_W 6$) are obtained according to the equations given in Bilek et al. [2004]. The comparison of scalar moments and NSDs also supports the results of Bilek et al. [2004], showing an increment of the normalized duration with the scalar moment. The expected lack of correlation among scalar moment and depth is confirmed by scattered distribution in Figure 5.7c. The most interesting result is discussed in Figure 5.7d, which illustrates the correlation among NSD and depth. Our results extend previous finding by Bilek et al. [2004] to a much broader magnitude range and including moderate earthquakes of magnitude down to M_W 4. The NSD drops significantly for increasing depth. On the other hand, it is typically assumed that the rupture velocity is slightly slower than the shear wave velocity, which increases with depth. The depth dependence of the rupture size, for a reference magnitude event, will then be affected by the combined and opposite depth dependence of NSD and rupture velocity.

5.5 Conclusion

We analysed 72 aftershocks of the 2010 Maule earthquakes, by means of moment tensor and source duration inversion, combining regional and teleseismic data in order to cover the whole aftershock sequence in the magnitude range between M_W 4.0 and 6.8. Focal mechanism solutions indicate that the majority of this earthquake took place as thrust faulting, with focal mechanisms similar to the main shock; few localized normal faulting solutions are associated to crustal faults. The consistency of our solutions with those published in previous studies has been confirmed upon the analysis of focal mechanism similarities, using a Kagan angle [Kagan, 1991, 1992] metric. Following a similar approach, we could observe a significant consistency among the thrust focal mechanism fault planes and the 3D model of the slab [Hayes et al., 2012]. Our inversion scheme allowed us to estimate the source duration for small magnitude earthquakes. The combined interpretation of focal mechanisms and source durations was used to verify that the correlation between normalized duration, scalar moment and depth, as first proposed by Bilek et al. [2004], remains valid for weaker earthquakes, at least down to Mw 4. Furthermore, we show that even for a narrow region this relation is still observable using the aftershock events of the Maule 2010 event, although the subducted oceanic plate behavior is suggested to be influenced by subducted heterogeneities. Since on a local/regional scale small events have larger relative source times our result suggest that the Central Chilean subduction zone has frictional properties favouring slow slip at shallow depths and therefore tsunamigenic earthquakes in case a (globally rare) large shallow ($\leq$ 15 km) rupture would occur.

5.6 Acknowledgements

We thank Caltech, GFZ, IPGP, IRIS and the University of Liverpool for providing continuous waveform data for IMAD network. We thank the Servicio Sismolgico Nacional de Chile (SSN) and the University of Santiago de Chile for logistical support during the deployment.We are grateful to Susan L. Bilek for providing us

the datasets. This work has been realized within the MARISCOS project funded by German Research Foundation (DFG, grant LA 2970/1-1). S. C. is funded by the MINE project (BMBF, German Ministry of Education and Research, Grant of project BMBF03G0737). We thank to IRIS and GEOFON data pool. Figures were generated using GMT [Wessel & Smith, 1998]

Conclusions

In this study, I proposed and tested specific seismological inversion schemes and automated routines, for the analysis of a broad range of seismic data, including induced seismicity at local distances, and natural seismicity at regional distances. These applications are particularly challenging, because of the weak magnitude of the target seismicity. Moreover, for the case of mining induced seismicity, a broader range of source processes must be accounted. For example, failure processes such as tensile cracks, collapses and rock-burst should be considered, but they are typically not modeled for natural earthquake sources. To this goal, and relying on the flexibility of the Kiwi tools as inversion algorithm, I modified previously existing inversion scheme, adapting them to analyze a broader range of data.

With this work I demonstrated that, if good quality waveform data and information on the velocity model for the study region are available, it is possible to resolve different source parameters for a broad range of magnitudes, including weak events below the standard magnitude target of moment tensor inversion routines. I also showed that these inversion procedures can be highly automatized, making feasible the analysis of large datasets. Following the previous experience of Cesca et al. [2006, 2010]; Dahm & Krüger [1999]; Romanowicz [1982], the inversion scheme highly relies on the fit of amplitude spectra, which reduce the problem related with the simplified velocity models, and the associated waveform alignment.

The performance of the inversion process, in terms of the smallest magnitude events which can be investigated, depends on the waveform quality and signal-to-noise ratio, on the geometry and number of available stations, and on the precise knowledge of the velocity structure of the target site. The source inversion for small events requires the modeling of higher frequency waveforms, which are sensitive to small scale heterogeneities. This implies a major limit for the inversion

approach, whenever the velocity model is poorly known. On the other hand, e.g. in the case of deep mines, where the velocity model is well known, the modeling of wave propagation can only be accounted if 3D velocity models are considered. Both cases show potential limits of the inversion scheme discussed in this thesis. A future extension of the inversion framework should consider 3D geometries, where Greens functions will depend on source and receiver location, and account for a 3D velocity model. Such extension is also required for 3D monitoring networks, in order to merge surface, bore-hole and in-mine sensors within a common inversion framework.

The analysis of mining induced seismicity confirmed the important role of synthetic tests, using a range of different velocity models, when assessing the source parameters uncertainties, or in order to chose the preferred inversion setup. Inversion with synthetic data can be used, for example, to select the preferred frequency range, or to identify possible trade offs in the resolution of different source parameters.

Apart from the methodological development and inversion setup, this work also contributes to the discussion and interpretation of rupture processes in different areas. The inversion scheme was applied to two very different datasets, finally providing more than 1000 focal mechanisms. The first dataset includes weak coal mining induced earthquakes, with magnitude ranging between M_W 0.0 and 2.0, which are analyzed on the base of short-period and broadband stations at very local distances, below 2 km. The second dataset focuses on the Chilean region, and includes a unique dataset from the aftershocks sequence of the 2010 M_W 8.8 Maule earthquake. The results are discussed in terms of focal mechanism solutions, source dimensions, source durations and the relation of these source parameters with respect to mining operations, for the induced seismicity dataset, and the seismotectonic settings and slab geometry, for the natural earthquake dataset.

The first case study targets a weak magnitude mining seismicity dataset following longwall mining in a coal mine in Germany. The application of full waveform MT inversion was successfully applied to more than 1000 mining induced events, despite the challenges of source inversion for so small events. The moment tensor inversion was performed fitting amplitude spectra and displacement traces of seismic data recorded at a local scale ($\leq$ 2 km) by a combination of broadband and short period stations. The quality of the data from this network (HAMMNET, installed by the Ruhr University Bochum) was excellent and determinant for the

inversion success, and allowed to derive source parameters for 1169 earthquakes, including very weak events down to a magnitude M_L=-0.5. The major conclusions from this study are the following. Best results are obtained when fitting amplitude spectra and displacement traces in the range between 0.5 and 4 Hz. The obtained focal mechanisms show similar style of faulting, characterized by a dominance of normal faulting, with one steep fault plane; strike angles are subparallel to the advancing mining stope or to the mining walls. Full MT inversion results shows that most of the events deviate from a pure DC model and include an opening crack component. The determination of finite source parameters remain demanding, because of the difficulty of reproducing the high-frequency observations, with simplified 1D structure model. As a consequence, finite source parameters are poorly resolved. However, the general pattern of kinematic inversion results would suggest that slow ruptures often occur along the steeper fault. Events have been classified in different clusters according to their source parameters: the observed bimodal FMD is better explained by clustering the events according to their fault plane orientations.

The same dataset was also reanalyzed in the light of a novel focal mechanism clustering algorithm, considering both the double couple (DC) and full moment tensor (MT) catalogs. The newly proposed clustering approach was successfully applied to these mining induced moment tensor datasets, revealing five families of DC focal mechanisms, associated with normal faulting of different orientations. This result confirmed that striking correspond to the orientation of the panel sides and stope. The clustering of full moment tensors, identified two main event families, characterized by the presence of positive and negative tensile components, where positive tensile component (65%) dominant in terms of number of events. The analysis of the temporal distribution of clusters indicate that during the first part of the longwall mining, ruptures are dominated by NNWSSE strike faulting, parallel to the mining stope. This pattern changes during the second part of the mining, when fault planes were mostly parallel to the panel sides

The second case study targets moderate magnitude aftershocks of the February 27, 2010, Maule earthquake. The moment tensor inversion and source duration inversion of 72 aftershocks, which have been performed combining regional and teleseismic data in order to cover the whole aftershock sequence, confirmed that the majority of this earthquake took place as thrust faulting, with a focal mechanism similar to the main shock. Additionally, few localized normal faulting solutions are associated to different shallow faults. Derived solutions proofed to

be consistent with available focal mechanisms. The analysis of focal mechanism similarities was performed using a Kagan angle [Kagan, 1991, 1992] metrics, following an approach introduced for the clustering of focal mechanisms. Results indicate a significant consistency among the thrust focal mechanism focal mechanism and the 3D slab model [Hayes et al., 2012]. The aftershock analysis included a discussion on source durations, which is an important new outcome of the proposed inversion scheme. The combined interpretation of focal mechanisms and source durations was used to verify that the correlation between normalized duration, scalar moment and depth, first proposed by Bilek et al. [2004], remains valid for weaker earthquakes, at least down to M_W 4. The source duration and depth relationship shows that mostly long duration events occur in the crust of the upper plate, above the subduction and short duration events mostly occur at larger depths.

Bibliography

Agurto, H., Rietbrock, A., Ryder, I., & Miller, M., 2012. Seismic-afterslip characterization of the 2010 mw 8.8 maule, chile, earthquake based on moment tensor inversion, *Geophysical Research Letters*, **39**(20).

Aki, K. & Richards, P. G., 1980. Quantitative seismology: Theory and methods, 1, *I: WH Freeman and Co*.

Archuleta, R. J. & Hartzell, S. H., 1981. Effects of fault finiteness on near-source ground motion, *Bulletin of the Seismological Society of America*, **71**(4), 939–957.

Becker, D., Cailleau, B., Dahm, T., Shapiro, S., & Kaiser, D., 2010. Stress triggering and stress memory observed from acoustic emission records in a salt mine, *Geophysical Journal International*, **182**(2), 933–948.

Ben-Menahem, A., 1961. Radiation of seismic surface-waves from finite moving sources, *Bulletin of the Seismological Society of America*, **51**(3), 401–435.

Ben-Menahem, A., 1962. Radiation of seismic body waves from a finite moving source in the earth, *Journal of Geophysical Research*, **67**(1), 345–350.

Bernardi, F., Braunmiller, J., Kradolfer, U., & Giardini, D., 2004. Automatic regional moment tensor inversion in the european-mediterranean region, *Geophysical Journal International*, **157**(2), 703–716.

Bilek, S. & Lay, T., 2002. Tsunami earthquakes possibly widespread manifestations of frictional conditional stability, *Geophysical Research Letters*, **29**(14), 18–1.

Bilek, S., Lay, T., & Ruff, L., 2004. Radiated seismic energy and earthquake source duration variations from teleseismic source time functions for shallow

subduction zone thrust earthquakes, *Journal of Geophysical Research: Solid Earth (1978–2012)*, **109**(B9).

Bischoff, M., Fischer, L., Fritschen, R., Meier, T., & Friederich, W., 2010a. Source mechanisms of mining induced seismic events in Hamm , eastern Ruhr area , Germany, vol. 4, p. 5000.

Bischoff, M., Cete, A., Fritschen, R., & Meier, T., 2010b. Coal mining induced seismicity in the ruhr area, germany, *Pure and applied geophysics*, **167**(1-2), 63–75.

Bock, G., 2012. NMSOP-GFZ: IS3.8 Source parameters and moment-tensor solutions.

Boyd, O., Dreger, D., Hellweg, M., Lombard, P., Ford, S., Taira, T., Taggart, J., & Weldon, T., 2011. Full moment tensor analysis using first motion data at the geysers geothermal field, *Am. Geophys. Un.*.

Brune, J. N., 1970. Tectonic stress and the spectra of seismic shear waves from earthquakes, *Journal of Geophysical Research*, **75**(26), 4997–5009.

Buforn, E., Pro, C., Cesca, S., Udias, a., & del Fresno, C., 2011. The 2010 Granada, Spain, Deep Earthquake, *Bulletin of the Seismological Society of America*, **101**(5), 2418–2430.

Bukchin, B., Clévédé, E., & Mostinskiy, A., 2010. Uncertainty of moment tensor determination from surface wave analysis for shallow earthquakes, *Journal of seismology*, **14**(3), 601–614.

Burridge, R. & Knopoff, L., 1964. Body force equivalents for seismic dislocations, *Bulletin of the Seismological Society of America*, **54**(6A), 1875–1888.

Cattaneo, M., Augliera, P., Spallarossa, D., & Lanza, V., 1999. A waveform similarity approach to investigate seismicity patterns, *Natural hazards*, **19**(2-3), 123–138.

Cesca, S. & Dahm, T., 2008. A frequency domain inversion code to retrieve time-dependent parameters of very long period volcanic sources, *Computers & Geosciences*, **34**(3), 235–246.

Cesca, S., Buforn, E., & Dahm, T., 2006. Amplitude spectra moment tensor inversion of shallow earthquakes in Spain, *Geophysical Journal International*, **166**(2), 839–854.

Cesca, S., Braun, T., Tessmer, E., & Dahm, T., 2007. Modelling of the April 5, 2003, Stromboli (Italy) paroxysmal eruption from the inversion of broadband seismic data, *Earth and Planetary Science Letters*, **261**(1-2), 164–178.

Cesca, S., Battaglia, J., Dahm, T., Tessmer, E., Heimann, S., & Okubo, P., 2008. Effects of topography and crustal heterogeneities on the source estimation of LP event at Kilauea volcano, *Geophysical Journal International*, **172**(3), 1219–1236.

Cesca, S., Heimann, S., Stammler, K., & Dahm, T., 2010. Automated procedure for point and kinematic source inversion at regional distances, *Journal of Geophysical Research: Solid Earth (1978–2012)*, **115**(B6).

Cesca, S., Heimann, S., & Dahm, T., 2011. Rapid directivity detection by azimuthal amplitude spectra inversion, *Journal of Seismology*, **15**(1), 147–164.

Cesca, S., Dost, B., & Oth, A., 2013a. Preface to the special issue triggered and induced seismicity: probabilities and discrimination, *Journal of Seismology*, pp. 1–4.

Cesca, S., Rohr, A., & Dahm, T., 2013b. Discrimination of induced seismicity by full moment tensor inversion and decomposition, *Journal of Seismology*, **17**(1), 147–163.

Chouet, B., Dawson, P., Ohminato, T., Martini, M., Saccorotti, G., Giudicepietro, F., De Luca, G., Milana, G., & Scarpa, R., 2003. Source mechanisms of explosions at stromboli volcano, italy, determined from moment-tensor inversions of very-long-period data, *Journal of Geophysical Research: Solid Earth (1978–2012)*, **108**(B1), ESE–7.

Chung, W.-Y. & Kanamori, H., 1976. Source process and tectonic implications of the spanish deep-focus earthquake of march 29, 1954, *Physics of the Earth and Planetary Interiors*, **13**(2), 85–96.

Coldewey, W. & Semrau, L., 1994. Mine water in the ruhr area (federal republic of germany), in *Proceedings of 5th International Mine Water Congress*, pp. 613–629.

Collings, R., Lange, D., Rietbrock, A., Tilmann, F., Natawidjaja, D., Suwargadi, B., Miller, M., & Saul, J., 2012. Structure and seismogenic properties of the mentawai segment of the sumatra subduction zone revealed by local earthquake traveltime tomography, *Journal of Geophysical Research: Solid Earth (1978–2012)*, **117**(B1).

Cotton, F. & Campillo, M., 1995. Frequency domain inversion of strong motions: Application to the 1992 landers earthquake, *Journal of Geophysical Research: Solid Earth (1978–2012)*, **100**(B3), 3961–3975.

Custodio, S., Cesca, S., & Heimann, S., 2012. Fast Kinematic Waveform Inversion and Robustness Analysis: Application to the 2007 Mw 5.9 Horseshoe Abyssal Plain Earthquake Offshore Southwest Iberia, *Bulletin of the Seismological Society of America*, **102**(1), 361–376.

Dahm, T., 2001. Rupture dimensions and rupture processes of fluid-induced microcracks in salt rock, *Journal of volcanology and geothermal research*, **109**(1), 149–162.

Dahm, T. & Krueger, F., 2014. NMSOP-GFZ: IS3.9 Moment Tensor Inversion and Moment Tensor Interpretation, pp. 1–259.

Dahm, T. & Krüger, F., 1999. Higher-degree moment tensor inversion using far-field broad-band recordings: theory and evaluation of the method with application to the 1994 bolivia deep earthquake, *Geophysical Journal International*, **137**(1), 35–50.

Dahm, T., Manthei, G., & Eisenblätter, J., 1999. Automated moment tensor inversion to estimate source mechanisms of hydraulically induced micro-seismicity in salt rock, *Tectonophysics*, **306**(1), 1–17.

Dahm, T., Horálek, J., & Šílenỳ, J., 2000. Comparison of absolute and relative moment tensor solutions for the january 1997 west bohemia earthquake swarm, *Studia Geophysica et Geodaetica*, **44**(2), 233–250.

Dahm, T., Becker, D., Bischoff, M., Cesca, S., Dost, B., Fritschen, R., Hainzl, S., Klose, C. D., Kühn, D., Lasocki, S., Meier, T., Ohrnberger, M., Rivalta, E., Wegler, U., & Husen, S., 2013. Recommendation for the discrimination of human-related and natural seismicity, *Journal of Seismology*, **17**(1), 197–202.

Davi, R., O'Brien, G., Lokmer, I., Bean, C., Lesage, P., & Mora, M., 2010. Moment tensor inversion of explosive long period events recorded on arenal volcano, costa rica, constrained by synthetic tests, *Journal of volcanology and geothermal research*, **194**(4), 189–200.

Domingues, A., Custódio, S., & Cesca, S., 2013. Waveform inversion of small-to-moderate earthquakes located offshore southwest iberia, *Geophysical Journal International*, **192**(1), 248–259.

Dreger, D. S., 2003. TDMT_INV: Time domain seismic moment tensor inversion, *International Geophysics*, **81**, 1627.

Dreger, D. S. & Helmberger, D. V., 1993. Determination of source parameters at regional distances with three-component sparse network data, *Journal of Geophysical Research*, **98**(B5), 8107.

Drozdzewski, G., 1993. The ruhr coal basin (germany): structural evolution of an autochthonous foreland basin, *International journal of coal geology*, **23**(1), 231–250.

Du, J. & Warpinski, N. R., 2011. Uncertainty in FPSs from moment-tensor inversion, *Geophysics*, **76**(6), WC65–WC75.

Dziewonski, A. M., Chou, T.-A., & Woodhouse, J. H., 1981. Determination of earthquake source parameters from waveform data for studies of global and regional seismicity, *Journal of Geophysical Research*, **86**(B4), 2825.

Ekström, G., Nettles, M., & Dziewoński, A., 2012. The global cmt project 2004–2010: centroid-moment tensors for 13,017 earthquakes, *Physics of the Earth and Planetary Interiors*, **200**, 1–9.

Ester, M., Kriegel, H.-P., Sander, J., & Xu, X., 1996. A density-based algorithm for discovering clusters in large spatial databases with noise., in *KDD*, vol. 96, pp. 226–231.

Farías, M., Vargas, G., Tassara, A., Carretier, S., Baize, S., Melnick, D., & Bataille, K., 2010. Land-level changes produced by the mw 8.8 2010 chilean earthquake, *Science*, **329**(5994), 916–916.

Feignier, B. & Young, R. P., 1992. Moment tensor inversion of induced microseisnmic events: Evidence of non-shear failures in the -4<m<-2 moment magnitude range, *Geophysical Research Letters*, **19**(14), 1503–1506.

Fletcher, J. & McGarr, A., 2005. Moment tensor inversion of ground motion from mining-induced earthquakes, trail mountain, utah, *Bulletin of the Seismological Society of America*, **95**(1), 48–57.

Foulger, G. R. & Julian, B. R., 1993. Non-double-couple earthquakes at the hengill-grensdalur volcanic complex, iceland: Are they artifacts of crustal heterogeneity?, *Bulletin of the Seismological Society of America*, **83**(1), 38–52.

Frohlich, C., 1995. Characteristics of well-determined non-double-couple earthquakes in the Harvard CMT catalog, *Physics of the Earth and Planetary Interiors*, **91**(4), 213–228.

Geersen, J., Behrmann, J. H., Völker, D., Krastel, S., Ranero, C. R., Diaz-Naveas, J., & Weinrebe, W., 2011. Active tectonics of the south chilean marine fore arc (35 s–40 s), *Tectonics*, **30**(3).

Giardini, D., Boschi, E., & Palombo, B., 1993. Moment tensor inversion from mednet data (2) regional earthquakes of the mediterranean, *Geophysical research letters*, **20**(4), 273–276.

Gibowicz, S. J., Kijko, A., Gibowicz, S., Kijko, A., & Gibowicz, S. J., 1994. *An introduction to mining seismology*, vol. 399, Academic Press San Diego.

Gilbert, F., 1971. Excitation of the normal modes of the earth by earthquake sources, *Geophysical Journal International*, **22**(2), 223–226.

Gilbert, G. K., 1884. A theory of the earthquakes of the great basin, with a practical application, *American Journal of Science*, (157), 49–53.

Glodny, J., Echtler, H., Collao, S., Ardiles, M., Burón, P., & Figueroa, O., 2008. Differential late paleozoic active margin evolution in south-central chile (37 s–40 s)–the lanalhue fault zone, *Journal of South American Earth Sciences*, **26**(4), 397–411.

Grigoli, F., Cesca, S., Vassallo, M., & Dahm, T., 2013. Automated Seismic Event Location by Travel-Time Stacking: An Application to Mining Induced Seismicity, *Seismological Research Letters*, **84**(4), 666–677.

Haberland, C., Rietbrock, A., Lange, D., Bataille, K., & Dahm, T., 2009. Structure of the seismogenic zone of the southcentral chilean margin revealed by local earthquake traveltime tomography, *Journal of Geophysical Research: Solid Earth (1978–2012)*, **114**(B1).

Hainzl, S., Zöller, G., Kurths, J., & Zschau, J., 2000. Seismic quiescence as an indicator for large earthquakes in a system of self-organized criticality, *Geophysical research letters*, **27**(5), 597–600.

Hardebeck, J. L. & Shearer, P. M., 2003. Using s/p amplitude ratios to constrain the focal mechanisms of small earthquakes, *Bulletin of the Seismological Society of America*, **93**(6), 2434–2444.

Hartzell, S. & Helmberger, D. V., 1982. Strong-motion modeling of the imperial valley earthquake of 1979, *Bulletin of the Seismological Society of America*, **72**(2), 571–596.

Hartzell, S. H. & Heaton, T. H., 1983. Inversion of strong ground motion and teleseismic waveform data for the fault rupture history of the 1979 imperial valley, california, earthquake, *Bulletin of the Seismological Society of America*, **73**(6A), 1553–1583.

Hasegawa, H. & Kanamori, H., 1987. Source mechanism of the magnitude 7.2 grand banks earthquake of november 1929: Double couple or submarine landslide?, *Bulletin of the seismological Society of America*, **77**(6), 1984–2004.

Hasegawa, H. S., Wetmiller, R. J., & Gendzwill, D. J., 1989. Induced seismicity in mines in canadaan overview, *pure and applied geophysics*, **129**(3-4), 423–453.

Haskell, N., 1964. Total energy and energy spectral density of elastic wave radiation from propagating faults, *Bulletin of the Seismological Society of America*, **54**(6A), 1811–1841.

Hayes, G. P., Wald, D. J., & Johnson, R. L., 2012. Slab1. 0: A three-dimensional model of global subduction zone geometries, *Journal of Geophysical Research: Solid Earth (1978–2012)*, **117**(B1).

Hayes, G. P., Bergman, E., Johnson, K. L., Benz, H. M., Brown, L., & Meltzer, A. S., 2013. Seismotectonic framework of the 2010 february 27 mw 8.8 maule, chile earthquake sequence, *Geophysical Journal International*, **195**(2), 1034–1051.

Hedley, D. & Wetmiller, R., 1985. Rockburst in ontario mines during 1984, canmet, energy, mines and recources canada report no.

Heimann, S., 2011. A robust method to estimate kinematic earthquake source parameters.

Henry, C., Woodhouse, J., & Das, S., 2002. Stability of earthquake moment tensor inversions: effect of the double-couple constraint, *Tectonophysics*, **356**(1-3), 115–124.

Herrmann, R., Benz, H., & Ammon, C., 2011. Monitoring the earthquake source process in north america, *Bulletin of the Seismological Society of America*, **101**(6), 2609–2625.

Hicks, S. P., Rietbrock, A., Haberland, C. A., Ryder, I., Simons, M., & Tassara, A., 2012. The 2010 mw 8.8 maule, chile earthquake: Nucleation and rupture propagation controlled by a subducted topographic high, *Geophysical Research Letters*, **39**(19).

Holub, K., 1999. Changes in the frequency-energy distribution of seismic events during mining in the ostrava-karvina coal field, *Studia geophysica et geodaetica*, **43**(2), 147–162.

Honda, H., 1962. Earthquake mechanism and seismic waves, *Journal of Physics of the Earth*, **10**(2), 1–97.

Hudson, J., Pearce, R., & Rogers, R., 1989. Source type plot for inversion of the moment tensor, *Journal of Geophysical Research: Solid Earth (1978–2012)*, **94**(B1), 765–774.

Jones, L. M., 1988. Focal mechanisms and the state of stress on the san andreas fault in southern california, *Journal of Geophysical Research: Solid Earth (1978–2012)*, **93**(B8), 8869–8891.

Jost, M. u. & Herrmann, R., 1989. A students guide to and review of moment tensors, *Seismological Research Letters*, **60**(2), 37–57.

Julià, J., Nyblade, A. A., Durrheim, R., Linzer, L., Gök, R., Dirks, P., & Walter, W., 2009. Source mechanisms of mine-related seismicity, savuka mine, south africa, *Bulletin of the Seismological Society of America*, **99**(5), 2801–2814.

Julian, B. R. & Foulger, G., 1996. Earthquake mechanisms from linear-programming inversion of seismic-wave amplitude ratios, *Bulletin of the Seismological Society of America*, **86**(4), 972–980.

Julian, B. R., Miller, A. D., & Foulger, G., 1998. Non-double-couple earthquakes 1. theory, *Reviews of Geophysics*, **36**(4), 525–549.

Kagan, Y. & Knopoff, L., 1976. Statistical search for non-random features of the seismicity of strong earthquakes, *Physics of the earth and planetary interiors*, **12**(4), 291–318.

Kagan, Y. Y., 1991. 3-D rotation of double-couple earthquake sources, *Geophysical Journal International*, **106**(3), 709–716.

Kagan, Y. Y., 1992. Correlations of earthquake focal mechanisms, *Geophysical Journal International*, **110**(2), 305–320.

Kagan, Y. Y. & Jackson, D. D., 1991. Long-term earthquake clustering, *Geophysical Journal International*, **104**(1), 117–133.

Kanamori, H., 1972. Tectonic implications of the 1944 tonankai and the 1946 nankaido earthquakes, *Physics of the earth and planetary interiors*, **5**, 129–139.

Kanamori, H., Ekström, G., Dziewonski, A., Barker, J. S., & Sipkin, S. A., 1993. Seismic radiation by magma injection: An anomalous seismic event near tori shima, japan, *Journal of Geophysical Research: Solid Earth (1978–2012)*, **98**(B4), 6511–6522.

Kaneshima, S., Kawakatsu, H., Matsubayashi, H., Sudo, Y., Tsutsui, T., Ohminato, T., Ito, H., Uhira, K., Yamasato, H., Oikawa, J., et al., 1996. Mechanism of phreatic eruptions at aso volcano inferred from near-field broadband seismic observations, *Science*, **273**(5275), 643–645.

Kijko, A., Drzezla, B., & Stankiewicz, T., 1988. Bimodal character of the distribution of extreme seismic events in polish mines, *Acta Geophysica Polonica*, **35**(2), 157–166.

Kikuchi, M. & Kanamori, H., 1982. Inversion of complex body waves, *Bulletin of the Seismological Society of America*, **72**(2), 491–506.

Kisslinger, C., 1980. Evaluation of s to p amplitude rations for determining focal mechanisms from regional network observations, *Bulletin of the Seismological Society of America*, **70**(4), 999–1014.

Knopoff, L. & Randall, M. J., 1970. The compensated linear-vector dipole: A possible mechanism for deep earthquakes, *Journal of Geophysical Research*, **75**(26), 4957–4963.

Konstantaras, A., Katsifarakis, E., Maravelakis, E., Skounakis, E., Kokkinos, E., & Karapidakis, E., 2012. Intelligent spatial-clustering of seismicity in the vicinity of the hellenic seismic arc., *Earth Science Research*, **1**(2).

Kravanja, S., Batini, F., Fiordelisi, A., & Panza, G., 2000. Full moment tensor retrieval from waveform inversion in the larderello geothermal area, *pure and applied geophysics*, **157**(9), 1379–1392.

Krieger, L. & Heimann, S., 2012. Mopadmoment tensor plotting and decomposition: a tool for graphical and numerical analysis of seismic moment tensors, *Seismological Research Letters*, **83**(3), 589–595.

Kuge, K. & Kawakatsu, H., 1990. Analysis of a deep non double couple earthquake using very broadband data, *Geophysical Research Letters*, **17**(3), 227–230.

Kuge, K. & Kawakatsu, H., 1992. Deep and intermediate-depth non-double couple earthquakes: interpretation of moment tensor inversions using various passbands of very broadband seismic data, *Geophysical Journal International*, **111**(3), 589–606.

Kuge, K. & Kawakatsu, H., 1993. Significance of non-double couple components of deep and intermediate-depth earthquakes: implications from moment tensor inversions of long-period seismic waves, *Physics of the earth and planetary interiors*, **75**(4), 243–266.

Kühn, D. & Vavryčuk, V., 2013. Determination of full moment tensors of microseismic events in a very heterogeneous mining environment, *Tectonophysics*, **589**, 33–43.

Kwiatek, G., Plenkers, K., & Dresen, G., 2011. Source Parameters of Picoseismicity Recorded at Mponeng Deep Gold Mine, South Africa: Implications for Scaling Relations, *Bulletin of the Seismological Society of America*, **101**(6), 2592–2608.

Lange, D., Tilmann, F., Barrientos, S. E., Contreras-Reyes, E., Methe, P., Moreno, M., Heit, B., Agurto, H., Bernard, P., Vilotte, J.-P., et al., 2012. Aftershock

seismicity of the 27 february 2010¡ i¿ mw¡/i¿ 8.8 maule earthquake rupture zone, *Earth and Planetary Science Letters*, **317**, 413–425.

Langston, C. A., 1976. A body wave inversion of the koyna, india, earthquake of december 10, 1967, and some implications for body wave focal mechanisms, *Journal of Geophysical Research*, **81**(14), 2517–2529.

Lawson, A. C. & Reid, H. F., 1908. *The California Earthquake of April 18, 1906: Report of the State Earthquake Investigation Commission...*, no. 87, Carnegie institution of Washington.

Lay, T., Ammon, C., Kanamori, H., Koper, K., Sufri, O., & Hutko, A., 2010. Teleseismic inversion for rupture process of the 27 february 2010 chile (mw 8.8) earthquake, *Geophysical Research Letters*, **37**(13).

Lay, T., Kanamori, H., Ammon, C. J., Koper, K. D., Hutko, A. R., Ye, L., Yue, H., & Rushing, T. M., 2012. Depth-varying rupture properties of subduction zone megathrust faults, *Journal of Geophysical Research: Solid Earth (1978–2012)*, **117**(B4).

Legrand, D., Kaneshima, S., & Kawakatsu, H., 2000. Moment tensor analysis of near-field broadband waveforms observed at Aso Volcano, Japan, *Journal of Volcanology and Geothermal Research*, **101**(1-2), 155–169.

Lippiello, E., Marzocchi, W., de Arcangelis, L., & Godano, C., 2012. Spatial organization of foreshocks as a tool to forecast large earthquakes, *Scientific reports*, **2**.

Lizurek, G. & Wiejacz, P., 2011. Moment tensor solution and physical parameters of selected recent seismic events at rudna copper mine, in *Geophysics in Mining and Environmental Protection*, pp. 11–19, Springer.

Lokmer, I., Bean, C. J., Saccorotti, G., & Patanè, D., 2007. Moment-tensor inversion of lp events recorded on etna in 2004 using constraints obtained from wave simulation tests, *Geophysical Research Letters*, **34**(22).

Love, A. E. H., 1927. *A treatise on the mathematical theory of elasticity*, Cambridge University Press.

Lund, B. & Bodjvarsson, R., 2002. Correlation of microearthquake body-wave spectral amplitudes, *Bulletin of the Seismological Society of America*, **92**(6), 2419–2433.

Madariaga, R. & Papadimitriou, P., 1985. Gaussian beam modelling of upper mantle phases, in *Annales geophysicae*, vol. 3, pp. 799–812, Gauthier-Villars.

Manthei, G., Eisenblätter, J., & Dahm, T., 2001. Moment tensor evaluation of acoustic emission sources in salt rock, *Construction and Building Materials*, **15**(5), 297–309.

Maruyama, T., 1963. On the force equivalents of dynamical elastic dislocations with reference to the earthquake mechanism.

Maurer, H. & Deichmann, N., 1995. Microearthquake cluster detection based on waveform similarities, with an application to the western swiss alps, *Geophysical Journal International*, **123**(2), 588–600.

McGarr, A., 1992a. An implosive component in the seismic moment tensor of a mining-induced tremor, *Geophysical research letters*, **19**(15), 1579–1582.

McGarr, A., 1992b. Moment tensors of ten witwatersrand mine tremors, *pure and applied geophysics*, **139**(3-4), 781–800.

Melis, N. S. & Konstantinou, K. I., 2006. Real-time seismic monitoring in the greek region: an example from the 17 october 2005 east aegean sea earthquake sequence, *Seismological Research Letters*, **77**(3), 364–370.

Melnick, D., Moreno, M., Motagh, M., Cisternas, M., & Wesson, R. L., 2012. Splay fault slip during the mw 8.8 2010 maule chile earthquake, *Geology*, **40**(3), 251–254.

Mendecki, A. J., 2012. Size distribution of seismic events in mines, in *Australian Earthquake Engineering Society 2012 Conference*.

Mendecki, A. J. & Lötter, E., 2011. Modelling seismic hazard for mines, in *Australian Earthquake Engineering Society 2011 Conference*.

Moreno, M., Melnick, D., Rosenau, M., Baez, J., Klotz, J., Oncken, O., Tassara, A., Chen, J., Bataille, K., Bevis, M., et al., 2012. Toward understanding tectonic control on the¡ i¿ m¡/i¿¡ sub¿ w¡/sub¿ 8.8 2010 maule chile earthquake, *Earth and Planetary Science Letters*, **321**, 152–165.

Mori, J. & Hartzell, S., 1990. Source inversion of the 1988 upland, california, earthquake: Determination of a fault plane for a small event, *Bulletin of the Seismological Society of America*, **80**(3), 507–518.

Nakamura, M., 2002. Determination of focal mechanism solution using initial motion polarity of P and S waves, *Physics of the Earth and Planetary Interiors*, **130**(1-2), 17–29.

Olson, A. H. & Apsel, R. J., 1982. Finite faults and inverse theory with applications to the 1979 imperial valley earthquake, *Bulletin of the Seismological Society of America*, **72**(6A), 1969–2001.

Ouillon, G. & Sornette, D., 2011. Segmentation of fault networks determined from spatial clustering of earthquakes, *Journal of Geophysical Research: Solid Earth (1978–2012)*, **116**(B2).

Panza, G., Šílený, J., Campus, P., Nicolich, R., & Ranieri, G., 1993. Point source moment tensor retrieval in volcanic, geothermal and orogenic areas by complete waveform inversion, *Journal of Applied Geophysics*, **30**(1-2), 89–118.

Panza, G. F. & Sarao, A., 2000. Monitoring volcanic and geothermal areas by full seismic moment tensor inversion: are non-double-couple components always artefacts of modelling?, *Geophysical Journal International*, **143**(2), 353–364.

Pedregosa, F., Varoquaux, G., Gramfort, A., Michel, V., Thirion, B., Grisel, O., Blondel, M., Prettenhofer, P., Weiss, R., Dubourg, V., et al., 2011. Scikit-learn: Machine learning in python, *The Journal of Machine Learning Research*, **12**, 2825–2830.

Pelzing, R., 1978. *Untersuchungen zur Ortung von Herden seismischer Ereignisse, dargestellt an Beispielen aus einem Stationsnetz in Ruhrbergbaugebiet*, Ph.D. thesis, Institut für Geophysik der Ruhr-Universität Bochum.

Pondrelli, S., Morelli, A., Ekström, G., Mazza, S., Boschi, E., & Dziewonski, A., 2002. European–mediterranean regional centroid-moment tensors: 1997–2000, *Physics of the Earth and Planetary Interiors*, **130**(1), 71–101.

Reasenberg, P. A. & Oppenheimer, D., 1985. *FPFIT, FPPLOT and FPPAGE: Fortran computer programs for calculating and displaying earthquake fault-plane solutions*.

Reid, H. F., 1910. *The mechanics of the earthquake*, vol. 2, Carnegie institution of Washington.

Rietbrock, A., Ryder, I., Hayes, G., Haberland, C., Comte, D., Roecker, S., & Lyon-Caen, H., 2012. Aftershock seismicity of the 2010 maule mw= 8.8, chile, earthquake: Correlation between co-seismic slip models and aftershock distribution?, *Geophysical Research Letters*, **39**(8).

Ritsema, J. & Lay, T., 1993. Rapid source mechanism determination of large (mw 5) earthquakes in the western united states, *Geophysical research letters*, **20**(15), 1611–1614.

Romanowicz, B. A., 1982. Moment tensor inversion of long period rayleigh waves: a new approach, *Journal of Geophysical Research: Solid Earth (1978–2012)*, **87**(B7), 5395–5407.

Ross, A., Foulger, G. R., & Julian, B. R., 1999. Source processes of industriallyinduced earthquakes at The Geysers geothermal area, California, *Geophysics*, **64**(6), 1877–1889.

Rueda, J. & Mezcua, J., 2005. Near-real-time seismic moment-tensor determination in spain, *Seismological research letters*, **76**(4), 455–465.

Rydelek, P. A. & Sacks, I. S., 1989. Testing the completeness of earthquake catalogues and the hypothesis of self-similarity, *Nature*, **337**(6204), 251–253.

Sarao, A., Panza, G., Privitera, E., & Cocina, O., 2001. Non-double-couple mechanisms in the seismicity preceding the 1991–1993 etna volcano eruption, *Geophysical Journal International*, **145**(2), 319–335.

Savage, J., 1966. Radiation from a realistic model of faulting, *Bulletin of the Seismological Society of America*, **56**(2), 577–592.

Şen, A., Cesca, S., Bischoff, M., Meier, T., & Dahm, T., 2013. Automated full moment tensor inversion of coal mining-induced seismicity, *Geophysical Journal International*, **195**(2), 1267–1281.

Şen, A., Heimann, S., Cesca, S., Lange, D., & Dahm, T., 2014. Systematic Changes Of Earthquake Rupture With Depth: A Case Study From The 2010 Mw 8.8 Maule, Chile, Earthquake Aftershocks sequence, *Submitted*.

Šílenỳ, J. & Milev, A., 2006. Seismic moment tensor resolution on a local scale: Simulated rockburst and mine-induced seismic events in the kopanang gold mine, south africa, *pure and applied geophysics*, **163**(8), 1495–1513.

Šílenỳ, J. & Milev, A., 2008. Source mechanism of mining induced seismic eventsresolution of double couple and non double couple models, *Tectonophysics*, **456**(1), 3–15.

Sokos, E. N. & Zahradnik, J., 2008. Isola a fortran code and a matlab gui to perform multiple-point source inversion of seismic data, *Computers & Geosciences*, **34**(8), 967–977.

Somerville, P. G., Smith, N. F., Graves, R. W., & Abrahamson, N. A., 1997. Modification of empirical strong ground motion attenuation relations to include the amplitude and duration effects of rupture directivity, *Seismological Research Letters*, **68**(1), 199–222.

Sornette, D. & Werner, M. J., 2005. Apparent clustering and apparent background earthquakes biased by undetected seismicity, *Journal of Geophysical Research: Solid Earth (1978–2012)*, **110**(B9).

Stein, S. & Wysession, M., 2009. *An introduction to seismology, earthquakes, and earth structure*, John Wiley and Sons.

Stich, D., Ammon, C. J., & Morales, J., 2003. Moment tensor solutions for small and moderate earthquakes in the ibero-maghreb region, *Journal of Geophysical Research: Solid Earth (1978–2012)*, **108**(B3).

Tanioka, Y. & Ruff, L. J., 1997. Source time functions, *Seismological Research Letters*, **68**(3), 386–400.

Tape, W. & Tape, C., 2012. A geometric comparison of source-type plots for moment tensors, *Geophysical Journal International*, **190**(1), 499–510.

Trifu, C., Angus, D., & Shumila, V., 2000. A fast evaluation of the seismic moment tensor for induced seismicity, *Bulletin of the Seismological Society of America*, **90**(6), 1521–1527.

Trifu, C.-I., Shumila, V., et al., 2010. Geometrical and inhomogeneous raypath effects on the characterization of open-pit seismicity, in *44th US Rock Mechanics Symposium and 5th US-Canada Rock Mechanics Symposium*, American Rock Mechanics Association.

Udias, A. U., 1999. *Principles of seismology*, Cambridge University Press.

Vallée, M. & Bouchon, M., 2004. Imaging coseismic rupture in far field by slip patches, *Geophysical Journal International*, **156**(3), 615–630.

Vavryčuk, V., 2001. Inversion for parameters of tensile earthquakes, *Journal of Geophysical Research: Solid Earth (1978–2012)*, **106**(B8), 16339–16355.

Vavryčuk, V. & Kühn, D., 2012. Moment tensor inversion of waveforms: A two-step time-frequency approach, *Geophysical Journal International*, **190**(3), 1761–1776.

Wang, R., 1999. A simple orthonormalization method for stable and efficient computation of green's functions, *Bulletin of the Seismological Society of America*, **89**(3), 733–741.

Warren, L. M. & Shearer, P. M., 2006. Systematic determination of earthquake rupture directivity and fault planes from analysis of long-period p-wave spectra, *Geophysical Journal International*, **164**(1), 46–62.

Wehling-Benatelli, S., Becker, D., Bischoff, M., Friederich, W., & Meier, T., 2013. Indications for different types of brittle failure due to active coal mining using waveform similarities of induced seismic events., *Solid Earth*, **4**(2).

Wessel, P. & Smith, W. H., 1998. New, improved version of generic mapping tools released, *Eos, Transactions American Geophysical Union*, **79**(47), 579–579.

Willemann, R. J., 1993. Cluster analysis of seismic moment tensor orientations, *Geophysical Journal International*, **115**(3), 617–634.

Zahradnik, J., Gallovic, F., Sokos, E., Serpetsidaki, A., & Tselentis, A., 2008. Quick fault-plane identification by a geometrical method: Application to the mw 6.2 leonidio earthquake, 6 january 2008, greece, *Seismological Research Letters*, **79**(5), 653–662.

Zhao, P., Kühn, D., Oye, V., & Cesca, S., 2014. Evidence for tensile faulting deduced from full waveform moment tensor inversion during the stimulation of the basel enhanced geothermal system, *Geothermics*.